

Development and test
of a controlled source MT method
in the frequency range
1 to 50 kHz

Andreas Pfaffhuber

Diploma Thesis
January 2001

Technical University Berlin
Institute for Applied Geoscience II
Department of Applied Geophysics

Ackerstraße 71-76
13355 Berlin

Content

Preface	6
Introduction	7
1 Theory	
<hr/> <hr/>	
1.1 Radiomagnetotelluric (RMT)	10
1.1.1 Basic principles-----	10
1.1.2 The impedance tensor in controlled source RMT (CSRMT)-----	12
1.1.3 The magnetotelluric formulation of a 1D earth-----	13
1.2 Finite sources over a layered halfspace	14
1.2.1 Reflection coefficients-----	14
1.2.2 Horizontal magnetic dipole-----	15
General solution	16
Far field approximation	17
Near field approximation	18
2 Modeling	
<hr/> <hr/>	
2.1 Numerical realization	20
2.1.1 Digital filtering-----	20
2.1.2 Computing the CSRMT Impedance tensor-----	21
2.1.3 Far field estimation-----	23
2.2 Homogeneous halfspace	24
2.2.1 Comparison of the far field approximation and the general solution-----	24
2.2.2 Fields over a homogeneous halfspace-----	26
Amplitudes	27
Phases	30
2.2.3 Scalar resistivities-----	31
2.2.4 RMT tensor resistivities-----	32
Dependency on position	32
Dependency on frequency and resistivity	35
2.3 Two layer case	36
2.3.1 Conductive overburden-----	36
2.3.2 Resistive overburden-----	37

2.3.3 Dependency on resistivity contrast-----	38
2.4 Far field distance estimation	40
2.5 Summary of the modeling results	43
3 Instrument	
<hr/> <hr/>	
3.1 Receiver	45
3.1.1 Technical specification-----	45
3.1.2 The control panel-----	47
3.2 Transmitter	51
3.2.1 Technical description-----	51
3.2.2 Improvements-----	52
Power supply	53
Heat production	53
4 Measurements	
<hr/> <hr/>	
4.1 Laboratory	56
4.1.1 Transmitter output-----	56
4.1.2 Calibration-----	57
4.1.3 Control program verification-----	58
4.2 Field	59
4.2.1 Resonance curves-----	59
4.2.2 Transmitter currents-----	60
4.2.3 Received signals-----	60
5 Interpretation concepts	
<hr/> <hr/>	
5.1 Inversion of near field data	63
5.2 Joint CSRMT and VLF profiling	65
6 Conclusion and Outlook	
<hr/> <hr/>	
Acknowledgments	69
List of figures	70
Appendix	73

Symbols

The most important symbols are listed and explained below. Generally bold letters mark vectors, underlined bold letters stand for tensors. Capital letters mark the frequency space whereas the lower case indicates the time space.

Coordinate system:

x, y, z	cartesian coordinates	m, m, m
r, ϕ, z	cylindrical coordinates	m, rad, m
$\lambda = \sqrt{k_x^2 + k_y^2}$	wavenumber	1/m
t	time	s
ω	angular frequency	rad/s

Fields and related quantities:

$\mathbf{E}, \mathbf{e} \dots$	electric field intensity	V/m
$\mathbf{J} = \sigma \mathbf{E} \dots$	electric current density	A/m ²
$\mathbf{D} = \epsilon \mathbf{E} \dots$	dielectric displacement	C/m ²
$\mathbf{H}, \mathbf{h} \dots$	magnetic field intensity	A/m
$\mathbf{B} = \mu \mathbf{H} \dots$	magnetic induction	Tesla
$Z = \frac{E_x}{H_y} = -\frac{E_y}{H_x} \dots$	scalar impedance	m/s
$\underline{\mathbf{Z}} \ (\mathbf{E} = \underline{\mathbf{Z}} \cdot \mathbf{H}) \dots$	impedance tensor	m/s
$\mathbf{T} \dots$	tipper vector	
$p = \sqrt{\frac{2}{\omega \mu \sigma}} \dots$	skin depth	m

Material properties and their derivatives:

$\rho = \sigma^{-1} \dots$	electric resistivity	Ωm
$\epsilon \dots$	dielectric permittivity	C/Vm
$\mu \dots$	magnetic permeability	Vs/Am
$\hat{z} = j \mu \omega \dots$	impedivity	
$\hat{y} = \sigma + j \epsilon \omega \dots$	admittivity	
$k = \sqrt{-\hat{z} \hat{y}} \dots$	complex wavenumber	
$k_\sigma = j \omega \mu \sigma \dots$	k for the quasi static approximation	

Parameters of the layered halfspace

$Z_i = \frac{\hat{z}}{k_i} \dots$	impedance of the i^{th} layer	m/s
$\hat{Z}_i \dots$	impedance at the top of the i^{th} layer	m/s
$Y_i = \frac{1}{Z_i}$	admittance of the i^{th} layer	s/m
$\hat{Y}_i \dots$	admittance at the top of the i^{th} layer	s/m
$r_{TE} \dots$	reflection coefficient for TE mode	
$r_{TM} \dots$	reflection coefficient for TM mode	

Source related quantities

$A_z \dots$	scalar TM potential of the HMD	
$F_z \dots$	scalar TE potential of the HMD	
$J_{0,1} \dots$	Bessel function of order 0,1 of the first kind	
$m \dots$	magnetic moment of the loop	Am ²
$h \dots$	height of the source dipole axis	m
$x_{5^\circ} \dots$	FFD in x- direction at 5° phase deviation	m
$y_{10} \dots$	FFD in y- direction at 10 % ampl. deviation	m

Preface

This thesis represents the final work of my studies at the Department of Applied Geophysics at the Technical University Berlin. With this, I am finishing my course of studies titled "Applied Geoscience" majoring Applied Geophysics.

The relatively new course of studies, "Applied Geoscience" combines a broad geoscientific background (which I gathered at the Mining University Leoben, Austria) with a profound knowledge of the specific main subject. Especially for geophysicists it is important to understand and question the geological plausibility of the various processing results of acquired field data.

During my studies in Berlin I was involved in a scientific project work of Tino Radic and Prof. Hans Burkhardt. The aim of this project was to evaluate the applicability of high temperature SQUID magnetometers for geophysical applications. In the scope of this project a new radio-frequency magnetotelluric (RMT) instrument was designed. As the Metronix company was a partner of the project, a transmitter with a frequency range from 1 kHz and upwards was contributed by them. As a result of the limited length of time, this transmitter prototype was never used during the project. Due to the lower applicable frequencies, the transmitter enables deeper soundings as the depth of investigation is inversely proportional to the square root of the frequency. Hence, this would increase the field of possible applications reaching deeper structures. However, before starting any field measurements, it has to be investigated if approximations, used in similar methods can be applied. For example if or under which restrictions assumptions can be adapted, that are used for conventional magnetotelluric processing. Induced by all these facts, step by step the main topic for my diploma thesis arose.

After the project was finished, I started to rework the transmitter to a field suitable condition. The control program of the RMT receiver also had to be adapted to meet the new requirements. At the same time I developed a forward modeling program for the fields of the used horizontal magnetic dipole (HMD) source.

Introduction

The radio-frequency magnetotelluric or radiomagnetotelluric (RMT) method, introduced by Turberg et. al. (1994), uses the electric and magnetic fields of artificial transmitters far off the measuring site in the frequency range from about 16 kHz up to 240 kHz. These sources are powerful communication transmitters for submarines in the very low frequency range (VLF) from 10 to 30 kHz and radio transmitters at higher frequencies. Hence, RMT is an extension to higher frequencies of the VLF-R technique described by McNeill and Labson (1988). Using standard MT algorithms, it is possible to estimate the apparent resistivity of the subsurface from orthogonal horizontal electric and magnetic fields on the earth's surface (Ward and Hohmann, 1988).

The typical fields of application are environmental problems such as the mapping of lateral and vertical boundaries of waste disposal sites (Tezkan et. al., 1995) and hydrogeophysical topics (Turberg et. al., 1994). With the five channel RMT instrument, developed at the department of Applied Geophysics (Radic and Burkhardt, 2000), it is possible to acquire resistivity data in a fast manner, which makes the system attractive for all types of resistivity profiling and sounding. With the introduced instrument it is possible to work with frequencies up to 1 MHz.

A limitation of the method is the frequency range and therefore the depth of investigation, as the lowest frequency and the resistivity of the subsurface determines the penetration depth of the electromagnetic waves. Regarding this problem, Tezkan et. al. (1995) combined transient electromagnetic measurements with RMT soundings to increase the depth of exploration. Another approach to overcome this limitation is the introduction of a transmitter to the system, extending the frequency range to lower limits. Furthermore in rural areas, where no radio transmitters are close, a controlled source contributes the needed signal strength. In contrast to RMT, for the audio frequency range the application of a horizontal electric dipole as source is a conventional method these days, called controlled source audiomagnetotelluric (CSAMT, Zonge and Hughes, 1988). Regarding AMT, the introduction of a transmitter was mainly due to the instable and often weak natural signals in this frequency range. As source for RMT the concept of a horizontal magnetic dipole (HMD) is preferred. This dipole type is realized by vertical standing loops in the field. The Metronix company contributed a RMT transmitter to the department of Applied Geophysics during a joint project. This source is a prototype of a later developed transmitter for the EnviroMT system, designed by the University of Uppsala (Sweden) and Metronix (Pedersen et. al., 1999).

This thesis illustrates the development of a CSRMT system from the five channel RMT receiver and the transmitter prototype. Besides the reworking of the instrument and its controlling software, synthetic data were calculated to evaluate the applicability of the plane wave solution (or to say MT interpretation) on the CSRMT measurements.

In the first chapter of this work the theoretical background for electromagnetic fields interacting with conductive matter is given. The description of the source fields, both with a general formula and approximations for the near and far field is of special interest.

The results of the modeling are illustrated in the second chapter. Amplitude and phase of the electric and magnetic fields of the HMD as well as the regarding magnetotelluric (scalar and tensor resistivities) and magnetic (tipper vector) transfer functions are presented. They are calculated considering the frequency, position of the receiver and subsurface resistivity. To evaluate the satisfaction of the far field condition, the synthetic data are compared to the MT apparent resistivities of the model. Resting upon the deviation of the HMD- and MT apparent resistivities, the far field distance (FFD) is introduced. It marks the range between transmitter and receiver where the deviation drops below a certain value. Besides a homogeneous halfspace, several two layer cases with different resistivity contrasts are taken into account to study the dependency of the FFD on the contrast. Finally a field formula to estimate the FFD is developed, which relates the far field distance to the skin depth.

In chapter three the changes that were adapted to the transmitter prototype and the RMT receiver control program are listed and described.

Chapter four illustrates the measurements performed both in the field and laboratory. Before any field measurements were started, the power of the transmitter amplifier was checked in the office. To verify all realized changes on the receiver system, it was calibrated and a simulation of a field measurement was conducted in the laboratory. Most of the field days were invested in tests related to the reworking of the transmitter. Hence, some acquired resonance curves are shown. To evaluate the actual transmitter moments for the specific frequencies, the maximum achievable currents in the transmitter loop were acquired under field conditions as well. Amplitudes of acquired fields are compared with synthetic data to end the measurements chapter.

Just previous to the conclusion, in chapter five two interpretation concepts, considering the results of the modelings and measurements, are introduced.

1 Theory

1.1 Radiomagnetotelluric (RMT)

Magnetotelluric (MT) deals with magnetic and electric fields on the earth's surface to investigate the conductivity structure of the subsurface.

The origins of these electromagnetic (EM) fields are sources on or above the earth's surface on one, and induced (secondary, internal) fields on the other side. Primary source fields are also called fields of external origin. These natural or artificial fields appear as homogeneous (plane waves) or inhomogeneous, spatially deformed fields around a finite source. In the so called far field inhomogeneous source fields can be treated as plane waves.

The electrical resistivity of the earth determines the secondary field strength and polarization which makes it possible to extract the subsurface resistivity information from the measured field data.

The following chapters will show the physical background for the oncoming topics. In the first subchapter some general descriptions of plane wave fields are given. The second subchapter gives the theoretical background for spatial deformed source fields of finite source.

Radiomagnetotelluric systems work on the MT-principle in the frequency range from 1 kHz up to 1 MHz. Sources of the electromagnetic fields are powerful communication transmitters for submarines in the VLF-frequency range (10-30 kHz) and radio transmitters at higher frequencies. Hence the basic relations for MT are given.

1.1.1 Basic principles

The following derivations are taken from Ward and Hohmann (1988) when no other source is given.

Working with time-varying fields $e, h = e_0, h_0 e^{j\omega t}$ in homogeneous regions and taking the constitutive relations $B = \mu H$, $J = \sigma E$, $D = \epsilon E$ (with electrical properties which are independent of time, temperature and pressure and μ assumed to be that of free space) into account, the Maxwell equations in the frequency domain are

$$\begin{aligned}\nabla \times E + \hat{z} H &= 0 \\ \nabla \times H - \hat{y} E &= 0\end{aligned}\tag{1-1}$$

with the impedivity $\hat{z} = j\mu\omega$ and the admittivity $\hat{y} = \sigma + j\epsilon\omega$. Considering plane waves traveling in z- direction the Maxwell equations can be converted into wave equations respectively Helmholtz equations in E and H

$$\begin{aligned}\nabla^2 E + k^2 E &= 0 \\ \nabla^2 H + k^2 H &= 0\end{aligned}\tag{1-2}$$

where k is the complex wave number $k^2 = -\hat{z}\hat{y} = \mu\epsilon\omega^2 - j\mu\sigma\omega$.

The solutions of the wave equation for a sinusoidal time dependence are

$$\begin{aligned} \mathbf{e} &= \mathbf{e}_0 e^{-j(kz - \omega t)} \\ \mathbf{h} &= \mathbf{h}_0 e^{-j(kz - \omega t)} \end{aligned} \quad (1-3)$$

Equations (1-3) describe a wave varying sinusoidally with z and t . As one can see the imaginary part of k attenuates the wave in z - direction. The distance at which the amplitude is reduced by a factor of $1/e$ is called the skin depth p , where

$$p = \sqrt{\frac{2}{\omega \mu \sigma}} \quad (1-4)$$

Employing the solutions (1-3) into the first Maxwell equation (1-1a) and considering waves polarized in the xy - plane, one will get the following relationship:

$$\frac{E_x}{H_y} = -\frac{E_y}{H_x} = \frac{\omega \mu}{k} = Z \quad (1-5)$$

In this equation Z stands for the plane wave impedance which is the magnetotelluric transfer function, defined as the ratio of orthogonal horizontal electric and magnetic field pairs. As $\mu \epsilon \omega^2 \ll j \mu \sigma \omega \rightarrow k^2 \approx j \mu \sigma \omega = k_\sigma^2$ for earth materials at frequencies less than 100 kHz equation (1-5) can be rewritten as

$$Z = \frac{\omega \mu}{k_\sigma} \rightarrow |\rho| = \frac{1}{\omega \mu} |Z|^2 \quad (1-6)$$

Equation (1-6) is valid over a 1D earth which is never the case in practice. Reflection and refraction of plane EM waves on two- or three-dimensional bodies result in a tensor definition of the impedance.

$$\underline{\mathbf{Z}} = \begin{bmatrix} Z_{xx} & Z_{xy} \\ Z_{yx} & Z_{yy} \end{bmatrix} \rightarrow \mathbf{E} = \underline{\mathbf{Z}} \cdot \mathbf{H} \quad (1-7)$$

Over a 1D earth $Z_{xy} = -Z_{yx}$ and $Z_{xx}, Z_{yy} = 0$.

In 2- and 3D environments an additional parameter besides the impedance tensor is used. The so called tipper vector \mathbf{T} , which is the vertical magnetic transfer function, describing the relationship between the horizontal and the vertical magnetic fields. It is defined as

$$H_z = T_x H_x + T_y H_y, \quad \mathbf{T} = (T_x \ T_y)^T. \quad (1-8)$$

For a horizontally layered halfspace $\mathbf{T} = \mathbf{0}$ due to $H_z = 0$. In the 2D case $\mathbf{T} \neq \mathbf{0}$ in the TE mode which means that the polarization of the electric field is parallel to the geological strike. If the E fields are normal to it and the magnetic field components are parallel to the strike the fields are of TM mode. TE and TM mode are notations which are used in MT literature. However, the given description for the two modes exactly meets the definition of the E- respectively B-polarization. To be strictly correct, TE mode means that the electric field is tangential to the surface and therefore has no vertical component. The correct definition of the TM mode follows analogically.

1.1.2 The impedance tensor in controlled source RMT (CSRMT)

See Zonge and Hughes (1988) for more details on this topic

The natural signal sources in MT have an infinite number of polarizations. Hence all elements of the impedance tensor and tipper vector can be estimated from one measurement of E_x, E_y, H_x, H_y and H_z . Artificial signals have one finite location and polarization which makes it impossible to determine the tensor elements from one measurement. Two independent, preferably perpendicular source polarizations must be used to calculate all of them. Since $\underline{\mathbf{Z}}$ has to meet $\mathbf{E}_1 = \underline{\mathbf{Z}} \mathbf{H}_1$ as well as $\mathbf{E}_2 = \underline{\mathbf{Z}} \mathbf{H}_2$ where the subscripts 1 and 2 indicate the two different source polarizations, $\underline{\mathbf{Z}}$ can be calculated by

$$Z_{xx} = \frac{E_{x1} H_{y2} - E_{x2} H_{y1}}{H_{x1} H_{y2} - H_{x2} H_{y1}}, \quad (1-9)$$

$$Z_{xy} = \frac{E_{x2} H_{x1} - E_{x1} H_{x2}}{H_{x1} H_{y2} - H_{x2} H_{y1}}, \quad (1-10)$$

$$Z_{yx} = \frac{E_{y2} H_{y1} - E_{y1} H_{y2}}{H_{x2} H_{y1} - H_{x1} H_{y2}}, \quad (1-11)$$

$$Z_{yy} = \frac{E_{y1} H_{x2} - E_{y2} H_{x1}}{H_{x2} H_{y1} - H_{x1} H_{y2}}. \quad (1-12)$$

In a similar way one can determine the tipper elements:

$$T_x = \frac{H_{z1} H_{x2} - H_{z2} H_{x1}}{H_{y1} H_{x2} - H_{x1} H_{y2}} \quad (1-13)$$

$$T_y = \frac{H_{z2} H_{y1} - H_{z1} H_{y2}}{H_{y1} H_{x2} - H_{x1} H_{y2}} \quad (1-14)$$

1.1.3 The magnetotelluric formulation of a 1D earth

The following considerations are taken from Ward and Hohmann (1988)

Performing MT measurements over a homogeneous halfspace yields directly the true electric conductivity of the subsurface using equation (1-6).

Considering a horizontally layered halfspace changes this relation. Layered means that the electrical parameters of the material change only along the z axis. Properties change at boundaries and are homogeneous within each layer. Measurements over such a 1D earth yield an apparent resistivity, named MT apparent resistivity in the following, which is affected by all layers.

To determine the impedance of this layered earth, in each layer up- and down-traveling waves are considered. Implying the continuity of tangential fields across interfaces leads to a recursive formulation of the plane wave impedance of a n-layered isotropic earth:

$$\hat{Z}_n = Z_n \frac{\hat{Z}_{n+1} + Z_n \tanh(jk_n h_n)}{Z_n + \hat{Z}_{n+1} \tanh(jk_n h_n)} \quad n=1,2,\dots,N-1 \quad (1-15)$$

The corresponding earth model consists of $N-1$ layers of thickness h_n , lying over an uniform halfspace. Z_n is the intrinsic impedance of every strata after equation (1-5), whereas \hat{Z}_n denotes the impedance at the top of the n^{th} layer derived by equation (1-15), except for the underlying halfspace where $\hat{Z}_N = Z_N$. Using equation (1-15) it is easy to compute \hat{Z}_1 and the MT apparent resistivity respectively. The surface admittance \hat{Y}_1 can be calculated analogically whereby the intrinsic admittance is given as $Y_n = k/\hat{Z}_n$.

1.2 Finite sources over a layered halfspace

Fields of an finite electromagnetic source on or over a conducting halfspace can be expressed as a superposition of numerous reflected plane waves at different angles of incidence.

As expected these fields don't satisfy the plane wave approximations of equation (1-2) within a certain distance from the source. This region is called "near field". Further away, in the "far field" the fields comply with the properties of normal incident plane waves.

1.2.1 Reflection coefficients

To determine the fields of the source over a layered halfspace, reflection and refraction of the EM wave on the numerous boundaries must be considered. Developing Snell's laws and the Fresnel equations yields the reflection coefficients for E perpendicular to (TE) and in (TM) the plane of incidence (Ward and Hohmann, 1988, pp. 183-202).

The reflection coefficients for the surface of the layered halfspace for TE and TM mode are given by

$$r_{TE} = \frac{Y_0 - \hat{Y}_1}{Y_0 + \hat{Y}_1} \quad \text{and} \quad r_{TM} = \frac{Z_0 - \hat{Z}_1}{Z_0 + \hat{Z}_1}. \quad (1-16 \text{ a,b})$$

As r_{TM} won't be used explicitly in the following, no simplifications are done on (1-16 b). In equation (1-16 a) Y_0 stands for the free space admittance and \hat{Y}_1 has to be determined by

$$\hat{Y}_n = Y_n \frac{\hat{Y}_{n+1} + Y_n \tanh(u_n h_n)}{Y_n + \hat{Y}_{n+1} \tanh(u_n h_n)} \quad (1-17)$$

as \hat{Z}_n in equation (1-15). Instead of the complex wavenumber for normal incidence (k), oblique incidence is considered now with

$$u_n^2 = k_x^2 + k_y^2 - k_n^2 = \lambda^2 - k_n^2. \quad (1-18)$$

Note that also for $Y_n = u_n / \hat{z}_n$ not k but u has to be taken into account. Setting $\hat{z}_n = \hat{z}_0$ for a nonmagnetic structure Y_n and \hat{Y}_n can be replaced by u_n and \hat{u}_n in equations (1-16) and (1-17).

Regarding the source field in free space the quasi static approximation is applied. Therefore the free space wavenumber $k_0 \ll \lambda$ for low frequencies and equation (1-16) turns into

$$r_{TE} = \frac{\lambda - \hat{u}_1}{\lambda + \hat{u}_1}. \quad (1-19)$$

The complex wavenumber on the surface of a layered earth is given recursively as

$$\hat{u}_n = u_n \frac{\hat{u}_{n+1} + u_n \tanh(u_n h_n)}{u_n + \hat{u}_{n+1} \tanh(u_n h_n)}. \quad (1-20)$$

Note that the complex wavenumber k_n in equation (1-18) contains ω , μ , σ and ε as well though displacement currents derived by ε_0 are neglected in (1-19) for the free space. Thus for the subsurface no low frequency approximation as in equation (1-6) was employed.

1.2.2 Horizontal magnetic dipole

At a distance of at least 5 (Ward and Hohmann, 1988), better 10 (Dey and Ward, 1970) loop radii a vertical loop can be treated as a horizontal dipole (HMD). In the following considerations the dipole axis is aligned in x direction in a height of h meters.

The field of a horizontal magnetic dipole consists of TE and TM modes as there is both an electric and a magnetic vertical field component. The TM and TE potentials are given as (Ward and Hohmann, 1988)

$$\begin{aligned} A_z(r, z) &= -\frac{k_0^2 m}{4\pi} \frac{\delta}{\delta y} \int_0^\infty [1 + r_{TM}] e^{-u_0 h} \frac{1}{\lambda u_0} J_0(\lambda r) d\lambda, \\ F_z(r, z) &= -\frac{\hat{z}_0 m}{4\pi} \frac{\delta}{\delta x} \int_0^\infty [1 + r_{TE}] e^{-u_0 h} \frac{1}{\lambda} J_0(\lambda r) d\lambda \end{aligned} \quad (1-21)$$

where A_z stands for the TM and F_z the TE potential. m represents the magnetic moment of the source in Am^2 and J_0 stands for the Bessel function of order 0 of the first kind. A cylindrical coordinate system is used with $r = \sqrt{x^2 + y^2}$ and z pointing downwards. The fields can be derived from the potentials using

$$\begin{aligned} \mathbf{E} &= -\hat{z} \mathbf{A} + \frac{1}{\hat{y}} \nabla (\nabla \cdot \mathbf{A}) - \nabla \times \mathbf{F} \text{ and} \\ \mathbf{H} &= -\hat{y} \mathbf{F} + \frac{1}{\hat{z}} \nabla (\nabla \cdot \mathbf{F}) + \nabla \times \mathbf{A}. \end{aligned} \quad (1-22)$$

General solution

Due to the infinite impedance contrast at the earth's surface and the inductively coupled source field, no TM mode fields are excited inside the conductive earth in the scope of the quasi static approximation. This can be seen from equation (1-21), since for $k_0 \approx 0$ the TM mode potential for a 1D earth A_z vanishes. Using equations (1-22) on F_z yields after differentiation

$$H_x = \frac{m}{4\pi} \left[\left(\frac{2x^2}{r^3} - \frac{1}{r} \right) I_1 - \frac{x^2}{r^2} I_2 \right] \quad (1-23)$$

$$H_y = \frac{m}{4\pi} \left[\frac{2xy}{r^3} I_1 - \frac{xy}{r^2} I_2 \right] \quad (1-24)$$

$$H_z = -\frac{m}{4\pi} \frac{x}{r} I_3 \quad (1-25)$$

$$E_x = \frac{m}{4\pi} i\mu\omega \left[-\frac{2xy}{r^3} I_4 + \frac{xy}{r^2} I_5 \right] \quad (1-26)$$

$$E_y = \frac{m}{4\pi} i\mu\omega \left[\left(\frac{2x^2}{r^3} - \frac{1}{r} \right) I_4 + \frac{x^2}{r^2} I_5 \right] \quad (1-27)$$

$$\begin{aligned} \text{where } I_1 &= \int_0^{\infty} [1 - r_{TE}(\lambda)] e^{-\lambda h} \lambda J_1(\lambda r) d\lambda, \\ I_2 &= \int_0^{\infty} [1 - r_{TE}(\lambda)] e^{-\lambda h} \lambda^2 J_0(\lambda r) d\lambda, \\ I_3 &= \int_0^{\infty} [1 + r_{TE}(\lambda)] e^{-\lambda h} \lambda^2 J_1(\lambda r) d\lambda, \\ I_4 &= \int_0^{\infty} [1 + r_{TE}(\lambda)] e^{-\lambda h} J_1(\lambda r) d\lambda \text{ and} \\ I_5 &= \int_0^{\infty} [1 + r_{TE}(\lambda)] e^{-\lambda h} \lambda J_0(\lambda r) d\lambda. \end{aligned} \quad (1-28)$$

The vector components of the fields \mathbf{E} and \mathbf{H} are given in cartesian coordinates. In equations (1-23) to (1-24) $r = \sqrt{x^2 + y^2}$ describes the distance between transmitter and receiver on the xy plane.

Far field approximation

At a transmitter – receiver separation of several skin depths ($kr \gg 1$), the far field approximation can be used to compute the fields of the source without solving any Integrals resp. Hankel transforms. Since the Integrals in equation (1-28) show an asymptotical behavior for $r \rightarrow \infty$ the fields over a homogeneous halfspace with both transmitter and receiver on the surface can be expressed as

$$H_r = \frac{m}{\pi r^3} \left(1 - \frac{6}{k_\sigma^2 r^2} \right) \cos \varphi , \quad (1-29)$$

$$H_\varphi = \frac{m}{2\pi r^3} \left(1 - \frac{3}{k_\sigma^2 r^2} \right) \sin \varphi , \quad (1-30)$$

$$H_z = -\frac{3m}{2\pi k_\sigma r^4} \cos \varphi , \quad (1-31)$$

$$E_r = \frac{k_\sigma m}{2\pi \sigma r^3} \sin \varphi , \quad (1-32)$$

$$E_\varphi = -\frac{k_\sigma m}{\pi \sigma r^3} \cos \varphi , \quad (1-33)$$

where k_σ stands for the complex wavenumber for the low frequency approximation as in equation (1-6). Different from the general solution now the fields are given in cylindrical components. H_r and E_r stand for the radial components respectively H_φ and E_φ for the tangential components (Weidelt, lecture script, unpublished). Calculating the apparent resistivity from orthogonal electric and magnetic field pairs as in equation (1-6) yields the MT apparent resistivity of the halfspace as the terms in brackets in equations (1-29) and (1-30) tend to unity for $kr \gg 1$.

Near field approximation

For comparison also the solutions for the near field valid if $kr \ll 1$ are given.

$$H_r = \frac{m}{2\pi r^3} \cos \varphi, \quad (1-34)$$

$$H_\varphi = \frac{m}{4\pi r^3} \sin \varphi, \quad (1-35)$$

$$H_z = -\frac{k_\sigma^2 m}{16\pi r} \cos \varphi, \quad (1-36)$$

$$E_r = \frac{k_\sigma^2 m}{4\pi \sigma r^2} \sin \varphi, \quad (1-37)$$

$$E_\sigma = -\frac{k_\sigma^2 m}{4\pi \sigma r^2} \cos \varphi. \quad (1-38)$$

2 Modeling

2.1 Numerical realization

The forward modeling program CSRMT_1Dmod.IIb was developed with LabVIEW™ 5.1, a graphical programming platform used in the completed project in which the receiver and its controlling software was designed.

Using the program it is possible to calculate the amplitudes and phases of $E_{x,y}$, $H_{x,y,z}$, Z , Z and T for a layered halfspace with intrinsic resistivity, thickness, and dielectric permittivity for each layer. Calculations can be done with respect to position, frequency and transmitter height & moment. In addition there is the possibility to determine a so called far field distance (FFD). At the FFD between receiver and transmitter the deviation of the HMD apparent resistivity to the MT apparent resistivity of the model drops below a certain value. The HMD apparent resistivity is derived from the orthogonal horizontal electric and magnetic fields of a HMD over a layered halfspace, calculated from equations (1-23) to (1-27). For example, the maximum deviation equals 10 % of the amplitude or 1° of the phase. In this work this is called far field estimation.

2.1.1 Digital filtering

To compute the numerous Hankel transforms in equations (1-28) a digital filter developed by Guptasarma and Singh (1997) was used. They presented two filters both for the Hankel transforms of order 0 and 1 of first kind. In this work the shorter filters with 61 points for J_0 resp. 47 points for J_1 have been used.

The Integrals of the Hankel transforms are of the form

$$f(r) = \int_0^{\infty} F(\lambda) J_{0,1}(\lambda r) d\lambda \quad (2-1)$$

Substituting $r = e^a$ and $\lambda = e^{-b}$ in equation (2-1) leads to a convolution integral

$$r \cdot f(r) = \int_{-\infty}^{\infty} k(b) h(a-b) db, \quad (2-2)$$

with $k(b) = F(\lambda)$ as the input and $h(a-b) = \lambda r J_{0,1}(\lambda r)$ as the filter function of the system. This integral can be approximated by the discrete convolution

$$r \cdot f(r) = \sum_{i=1}^l k(r-i) h(i) \quad (2-3)$$

This numerical approach on analytically known Hankel transforms yields the filter function $h(i)$ and the values for shift sh and spacing sp .

To perform the convolution, the kernel function $F(\lambda)$ must be computed on specific abscissa values λ_i which are calculated with the help of sh and sp :

$$\lambda_i = \frac{1}{r} 10^{sh + (i-1)sp}, \quad i=1,2,\dots,l. \quad (2-4)$$

The integral can then be computed with

$$f(r) = \frac{\sum_{i=1}^l F(\lambda_i) h(i)}{r}. \quad (2-5)$$

The curves for h_i and values for sh and sp are given in Appendix II÷1. Values for h_i are listed in Guptsarma and Singh (1997).

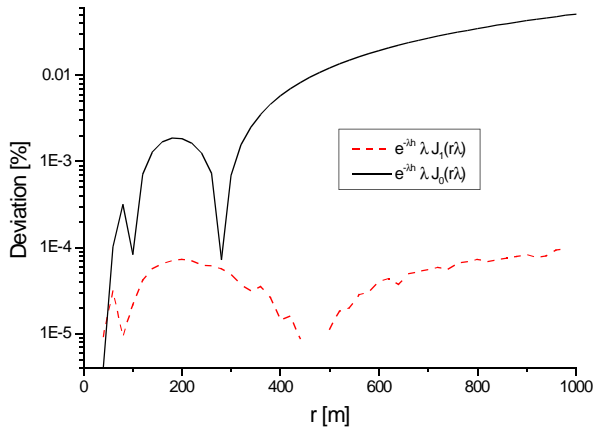


Figure 2-1 Deviation of the Hankel transforms computed analytical and with a digital filter.

To investigate the accuracy of the digital filter routine, two known Hankel transforms were computed analytically and with the filter algorithm. One example for the order 0 is

$$\int_0^{\infty} e^{-\lambda h} \lambda J_0(\lambda r) d\lambda = \frac{h}{\sqrt{(h^2 + r^2)^3}}$$

and for the order 1

$$\int_0^{\infty} e^{-\lambda h} \lambda J_1(\lambda r) d\lambda = \frac{r}{\sqrt{(h^2 + r^2)^3}}.$$

Calculations were done for r from 0 to 1.000 m at a height h of 1.25 m. The deviation of the two single results is shown in figure 2-1 for both of the transforms. In the range of r , which is of interest, the deviation remains below 0.1%. This accuracy meets the requirements for the forward modeling routine. Therefore the numerical approach is the basis of the further work.

2.1.2 Computing the CSRMT Impedance tensor

The fields E , H and Z are calculated directly from equations (1-23) to (1-27) and (1-5). To compute the elements of the impedance tensor, measurements with two transmitter polarizations have to be considered. In order to keep the time for calculation low, only one polarization is computed and afterwards rotated to a second. This can be done, as long as a layered earth is concerned. For both

polarizations the transmitter is located at $(x=0, y=0)$ with dipole axis x resp. y for polarization 1 resp. 2. Relating the new coordinates (x_2, y_2) to the original values (x_1, y_1) is the first step to rotate the data matrix. In this case

$$x_2 = -y_1, \quad y_2 = x_1 \quad (2-6)$$

and consequently the function values f for the 2nd polarization are

$$f_2(x_2, y_2) = f_1(-y_1, x_1). \quad (2-7)$$

Next the changed directions of the calculated fields have to be considered after equation (2-6). To give an example $H_{x2}(x_2, y_2) = -H_{y1}(-y_1, x_1)$. After equation (1-24) a changed sign of y also changes the sign of H_y . With $f(y_1, x_1) = f^T(x_1, y_1)$ the fields of the second polarization are

$$\begin{aligned} H_{x2} &= H_{y1}^T, & E_{x2} &= -E_{y1}^T, \\ H_{y2} &= H_{x1}^T, & E_{y2} &= -E_{x1}^T \text{ and} \\ H_{z2} &= H_{z1}^T. \end{aligned} \quad (2-8)$$

Applying equations (2-8) on equations (1-9) to (1-14) yields

$$\begin{aligned} Z_{xx} &= \frac{E_{x1} H_{x1}^T + E_{y1} H_{y1}^T}{H_{x1} H_{x1}^T - H_{y1} H_{y1}^T}, & Z_{xy} &= \frac{-E_{y1} H_{x1} - E_{x1} H_{y1}^T}{H_{x1} H_{x1}^T - H_{y1} H_{y1}^T}, \\ Z_{yx} &= \frac{-E_{x1} H_{y1} - E_{y1} H_{x1}^T}{H_{y1} H_{y1}^T - H_{x1} H_{x1}^T}, & Z_{yy} &= \frac{E_{y1} H_{y1}^T + E_{x1} H_{x1}^T}{H_{y1} H_{y1}^T - H_{x1} H_{x1}^T}, \\ T_x &= \frac{H_{z1} H_{y1}^T - H_{z1}^T H_{x1}}{H_{y1} H_{y1}^T - H_{x1} H_{x1}^T}, & T_y &= \frac{H_{z1}^T H_{y1} - H_{z1} H_{x1}^T}{H_{y1} H_{y1}^T - H_{x1} H_{x1}^T}. \end{aligned} \quad (2-9)$$

In this way the impedance- and tipper elements are determined from one forward modeling.

2.1.3 Far field estimation

As mentioned before, the program is able to find the distance to the transmitter where the deviation of the HMD- to the MT apparent resistivities of the model drops below a certain value. Compared to the analytical far field condition $|kr| \gg 1$ this way represents a more handsome definition of the far field which can be used in the field as well. It can be calculated for certain frequencies and resistivities. The decisive condition for the far- / near- field determination is the deviation of the HMD- and MT apparent resistivity of the model.

The distance is found easily: For a certain frequency and resistivity the search routine starts in the far field at a distance of 1.000 m which is decreased by a step length of 50 m every iteration. As soon as the near field is reached, the step length is reduced to 5 m and the current distance increased by 50 m to get into the far field again. This procedure continues down to a step length of 0.1 m. Hence the far field estimation is computed with an accuracy of 0.1 m. The calculated FFDs are termed x_{1° or y_5 which stands for a deviation of 1° phase or 5 % amplitude respectively distances in x- or y- direction for example.

However the far field distances in the Chapters 2.2 to are not calculated in the introduced way, but picked manually out of the HMD resistivity amplitude and phase data. All FFDs in the chapters 2.3.3 and 2.4 have to be precise and are therefore determined with the described accuracy of 0.1 m.

2.2 Homogeneous halfspace

The spatial propagation of the field of horizontal electric dipoles (HED) is well known. For example Zonge and Hughes (1988) calculated the fields over a homogeneous halfspace. The spatial fields of a horizontal magnetic dipole (HMD) are presented in the following chapter as results from several calculations. The fields are computed in dependency of the position, frequency and resistivity. The relative dielectric permittivity is set to 10 for all executed simulations. The dependency on ϵ was controlled by some calculations with different values, but the effect on the data was neglectable.

2.2.1 Comparison of the far field approximation and the general solution

First the fields are computed for one frequency and resistivity along a certain profile to compare the calculations with the results of the far field approximation. This can also be seen as a test of the forward modeling routine. In the following not the magnetic field \mathbf{H} but the magnetic induction \mathbf{B} will be considered as it also is measured with a wire loop magnetometer.

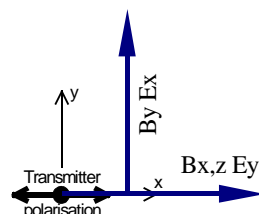


Figure 2-2 Position of the two simulated profiles.

Two profiles were computed: The first starts at $(x = 0, y = 0)$ and runs along the x axis to a distance of 1000 m (see figure 2-2). On this profile B_x , E_y and B_z are calculated. The second line starts at $(x = 5 \text{ m}, y = 0)$ and runs parallel to the y axis. Here E_x and B_y are determined. The reason for this layout is that E_x and B_y are both zero on the x and y axis.

In figure 2-3 the curves of the fields can be seen. Dashed lines mark the far field approximation of the respective fields calculated from equations (1-29) to (1-30). Note that B_x - E_y and B_z are on a different profile than E_x - B_y . One can see that at a distance of roughly 3 skin depths (p), the general solution meets the far field approximation. It can also clearly be seen, that both fields decay with the same slope. Hence the impedance remains at a constant value. Mathematically the far field approximation is defined to be valid at a distance where $kr \gg 1$. Here 10 seems to be a value $\gg 1$.

The E fields decrease slower in the near than in the far field. There is a strong change in the slope of the E field when far field conditions are met and the distance - dependency changes from $1/r^3$ to $1/r^2$. In the near field the amplitudes are controlled just by the distance. As the magnetic fields in the near field are also not controlled by the resistivity or frequency, this dependence allows no resistivity soundings in the near field with the HMD. Note that this restriction is valid only for "traditional" soundings involving orthogonal pairs of E and B.

The horizontal magnetic fields are primary fields which are influenced by the conductivity of the halfspace with increasing distance to the source. Because of this, they have a smoother curvature than the electric fields which are entirely secondary fields. The slope of the magnetic fields doesn't change but they are shifted to greater amplitudes in the far field.

Considering tipper measurements, mind the curve of B_z which doesn't meet plane wave conditions inside the observed range. B_z keeps decreasing faster than B_x but doesn't vanish! The source induced scalar tipper element T_x^S reaches values up to 41 % just before passing a distance of 3 skin depths and decreases to roughly 5 % in the far field (appendix II÷2). This has to be taken into account when CS-tipper measurements are used. The advantage of this effect is the possibility to conduct

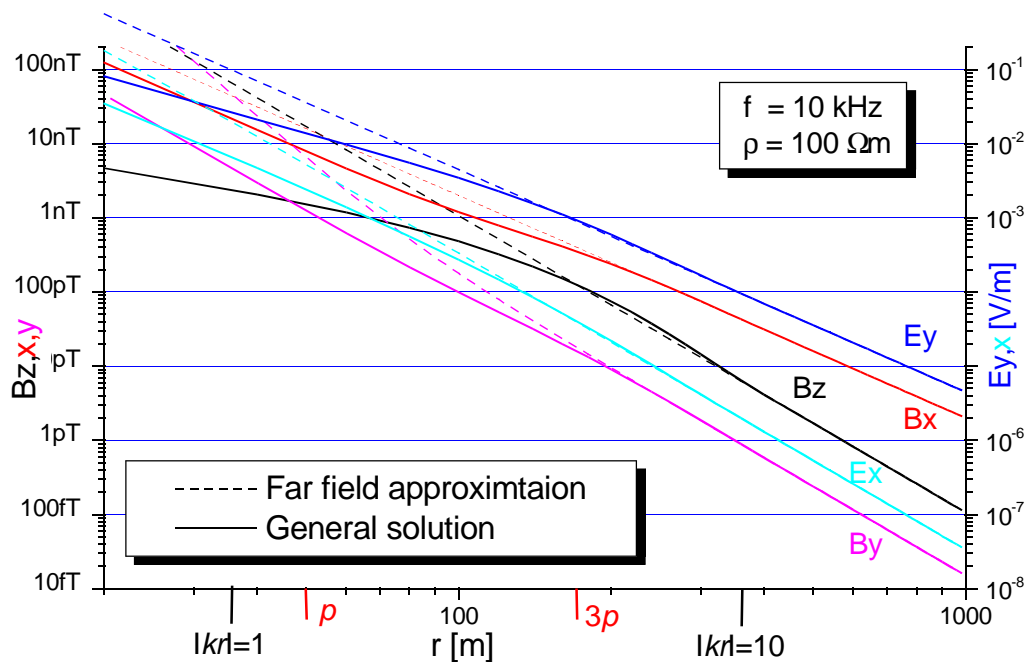


Figure 2-3 Calculated amplitudes of the electric and magnetic fields caused by a HMD over a homogeneous halfspace. On the abscissa the skin depth ρ and the induction parameter $|krl|$ are provided.

resistivity measurements in the near field using the vertical magnetic field. It is depending on distance, frequency and resistivity in the near and the far field. It might be a practical problem that the distance contributes to T_x^S with the power of two and thus it would have to be measured accurately. Using B_z itself for the sounding would prevent this problem ($B_z \sim r$).

The phases show similar effects. Secondary fields start with 90° for $E_{x,y}$ resp. 180° for B_z and meet a phase of $\pm 45^\circ$ in the far field at about 4 skin depths in this example. The curves can be seen in appendix II÷5.

2.2.2 Fields over a homogeneous halfspace

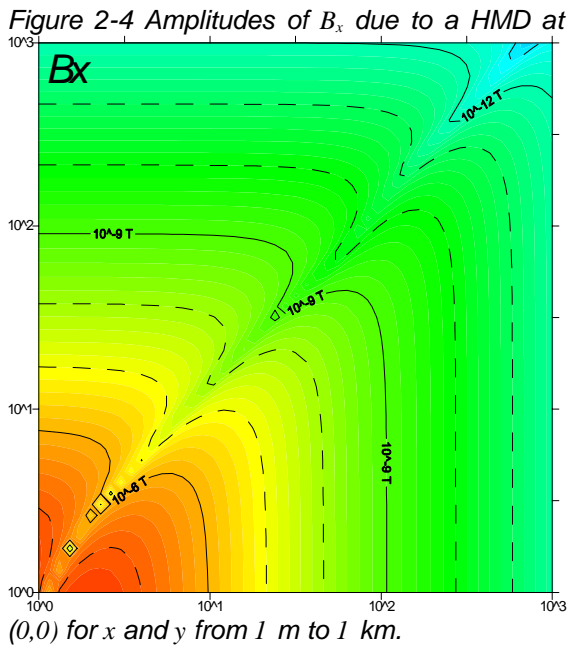
After analyzing the fields on certain profiles the spatial distribution is now examined.

The simulations in the next chapters where done with the following parameters:

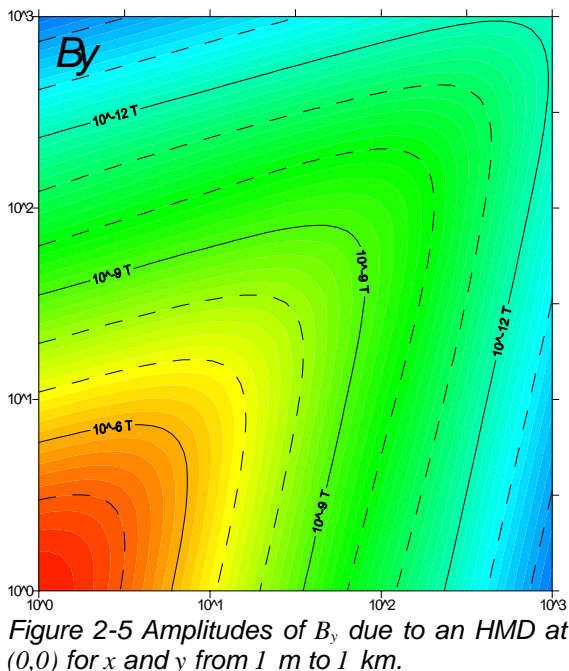
Frequency f	10 kHz
Halfspace resistivity ρ	100 Ωm
Height of dipole h	1.25 m
Transmitter moment m	5.000 Am^2

It will be noted when different values are used. All the following contour plots extend from 1 m to 1 km on the logarithmically scaled x- and y axis. The transmitter is located at the origin of the coordinate system with a polarization in x direction.

Amplitudes



To understand the properties of the calculated HMD apparent resistivities, it is helpful to have a look at the fields themselves. Note that B_x and E_y as well as B_y and E_x show corresponding spatial characteristics (Appendix II-3). Therefore only B_x and B_y are shown in the following figures. The given explanations mostly refer to B_x, E_y or B_y, E_x jointly. B_x and E_y show a zero crossing when they change their orientation to get from the “north-” to the “south-pole” of the transmitter again (figure 2-4). B_y and E_x don't show this changing of the sign but reach their maximum in the same region and tend to zero on the x- and y axis (figure 2-5). Note that the minimum values for x or y in the regarding figure are 1 m and thus the fields don't reach a zero level on the lower and left margin. The values of B_x or E_y depend on the azimuth from the source. The fields on the polarization axis of the transmitter are twice as high as normal to it. Measurements in this region close to the x axis are called collinear whereas the area around the y axis is defined as broadside. These definitions are used to compare the results with the characterization of the HED fields in Zonge and Hughes (1988). As one can see in this article the fields of the HED are vice versa.



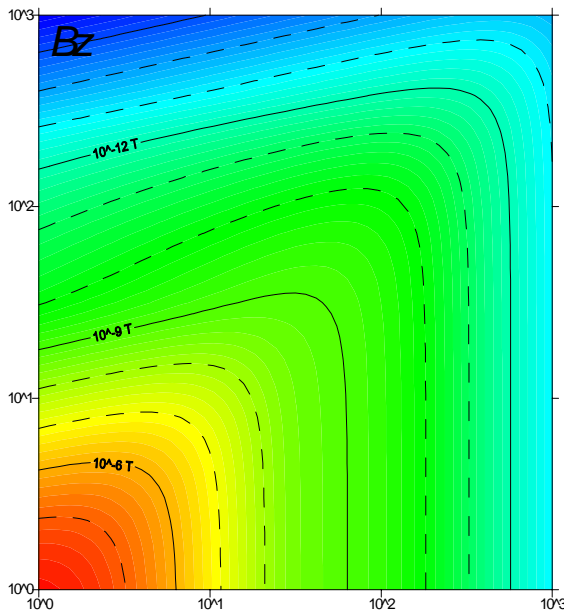
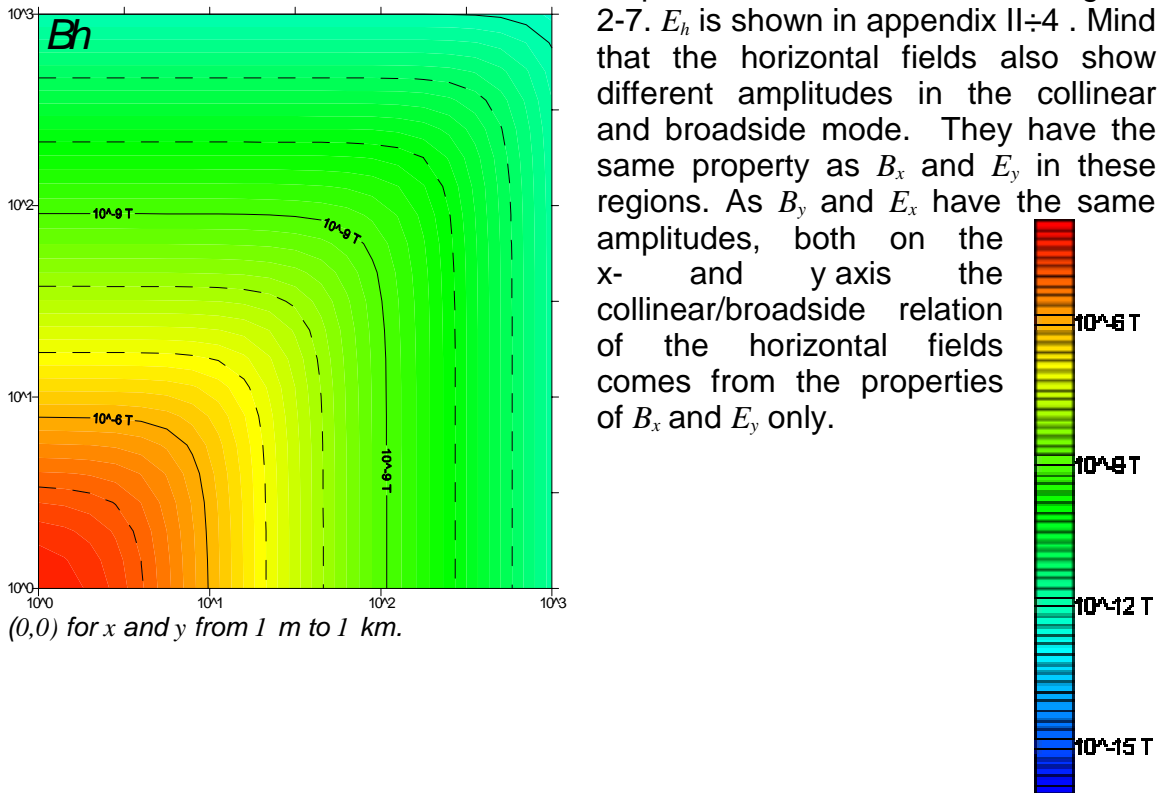


Figure 2-6 Amplitudes of B_z due to a HMD at $(0,0)$ for x and y from 1 m to 1 km.

In figure 2-6 the vertical component of the magnetic field is plotted. It shows a quite asymmetrical behavior, reaching a maximum in the line of the dipole axis and passing a zero crossing in the broadside mode (on the y axis). This behavior is in good accordance to Maxwell's equations where $j\omega B_z = \partial E_x / \partial y - \partial E_y / \partial x$. E_x equals zero on the y axis and hence $\partial E_x / \partial y = 0$. In the far field E_y is independent on x because it passes the y axis with a constant amplitude. Hence $\partial E_y / \partial x \approx const$ on the y axis. It is an important information that tipper measurements should be conducted in the broadside layout though the other fields have the weakest amplitudes here.

As one can expect the horizontal fields B_h and E_h don't show such a behavior. They are defined as $B_h = \sqrt{B_x^2 + B_y^2}$ respectively $E_h = \sqrt{E_x^2 + E_y^2}$ and show a roughly rectangular pattern. The amplitudes of B_h can be seen in figure 2-7. E_h is shown in appendix II-4. Mind that the horizontal fields also show different amplitudes in the collinear and broadside mode. They have the same property as B_x and E_y in these regions. As B_y and E_x have the same amplitudes, both on the x - and y axis the collinear/broadside relation of the horizontal fields comes from the properties of B_x and E_y only.

Figure 2-7 Amplitudes of B_h due to a HMD at $(0,0)$ for x and y from 1 m to 1 km.



$(0,0)$ for x and y from 1 m to 1 km.

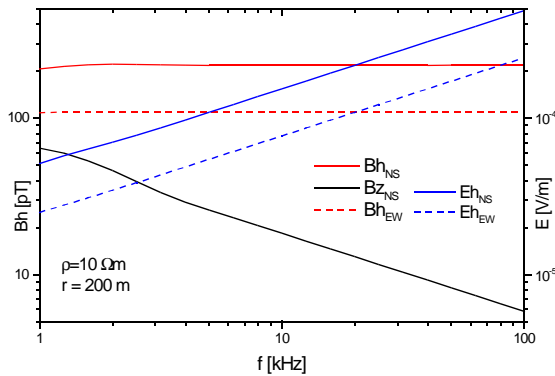


Figure 2-8 Dependency of the electric and magnetic fields on the frequency for different transmitter polarizations.

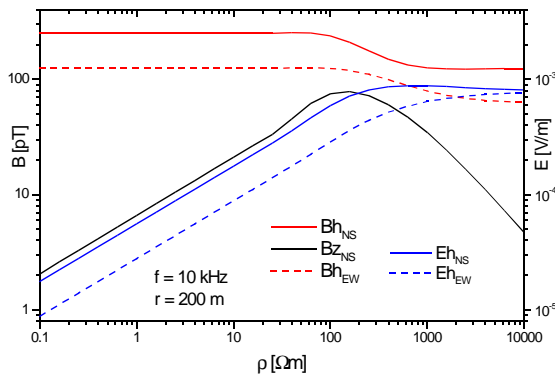


Figure 2-9 Dependency of the electric and magnetic fields on the halfspace resistivity for different transmitter polarizations

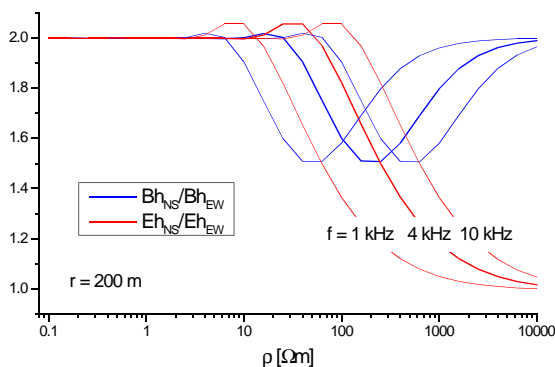


Figure 2-10 Ratio of the horizontal fields in collinear and broadside measurements

Consider a profile strike of 0° (N-S) and two transmitter polarizations. The first polarization heading to the north (NS polarization) and the second to the east (EW polarization). The measured horizontal fields in NS polarization (collinear) will be roughly 2 times as strong as the fields in EW polarization (broadside). This ratio seems to be independent of the frequencies but related to the resistivity. In figure 2-8 one can see that the amplitude of the E field changes with the frequency but the ratio of the values at the different polarizations doesn't change. The increase of E_h with frequency can be explained by equation 1-5 where the relation of the E and B field to the frequency and resistivity is clear. Based on constant values of B the electric field is coupled directly proportional to the frequency. Around 1 kHz a little bend introduces the near field. The vertical magnetic field decreases with increasing frequency. The higher the frequency, the better is the far field condition fulfilled and B_z decreases. Note that the amplitude is quite high anyhow. There is no broadside B_z plotted because the field passes a zero crossing on the y axis. More descriptive near field conditions can be observed in figure 2-9. Here the fields are calculated as a function of the halfspace resistivity. In the far field E_h and B_z increase with frequency by a factor of $\sqrt{\rho}$. Equations 1-31 to 1-33 predict this relationship. At a halfspace resistivity of roughly $100 \Omega\text{m}$ near field effects start to exert influence. The electric fields tend to a constant value which is the same for both transmitter

polarizations. Note that the ratio of the fields at different transmitter azimuths changes in figure 2-10. A ratio of 1 means that $E_x = E_y$, which implies an existence of Z_{xx} and/or Z_{yy} over the simulated 1D earth. This is the only possibility for $E_x = E_y$ while $B_x \neq B_y$. If $Z_{xx}=0 \Rightarrow Z_{yy}=Z_{xy}-2Z_{yx}$ while $Z_{xx}=Z_{yx}-Z_{xy}/2$ if $Z_{yy}=0$. This effect can be understood when the three dimensional structure of the source is considered. Such as a 3D subsurface delivers values unequal zero for Z_{xx} and Z_{yy} for the plane wave solution, a primary field with a finite source over a homogeneous halfspace fills the impedance tensor with four nonzero elements. The shift of the magnetic fields when passing the far/near field border (which was already introduced in Chapter 2.2.2) can also be seen in figure 2-9. Note in figure 2-10 that the ratio of collinear to broadside field returns to the value of 2 again in the near field.

Mind that all these considerations were done using the quasi static approximation. In the near field regions of figure 2-9 and 2-10 at resistivities of 10 kΩm also displacement currents would have to be taken into account. Then the amplitudes of the horizontal fields would not be constant.

Phases

The phases of the fields over a homogeneous halfspace show similar effects as the amplitudes. Appendix II-6 shows the plots for all five phases. As an example the phases of E_y are shown in figure 2-11. As a matter of principle two different effects can be observed:

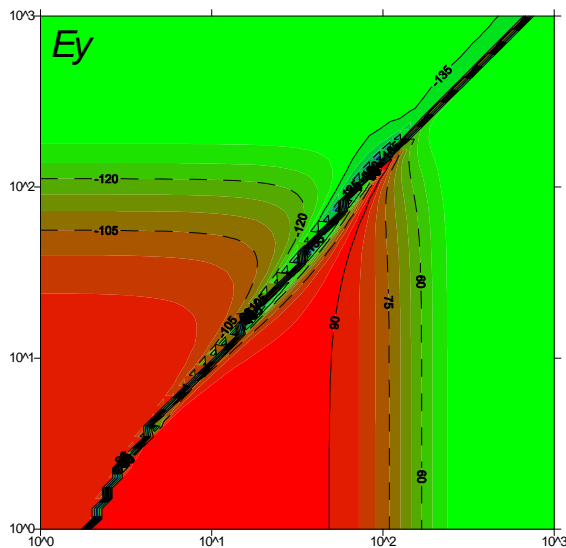
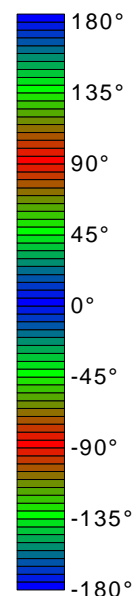


Figure 2-11 Phases of E_y due to a HMD at (0,0) for x and y from 1 m to 1 km.

First the change of the phase depending on the distance from the source marks the change from the near into the far field. The primary horizontal B field phases show a trend to a level of approximately 20° over their normal value of 0° respectively 180° in the transition zone (see appendix II-6). Note that this zone is passed at about 11 skin depths (575m) on the x and y axis concerning B_y . At this distance the phase deviation goes below 1° again. The corresponding ranges for B_x are $8p$ for broadside and $13p$ for collinear measurements.

The secondary horizontal electric fields start with $\pm 90^\circ$ phase and meet 45° respectively -135° in the far field. The distances from the source where these values are reached within a deviation of 1° are $8p$ for E_x and collinear E_y respectively $6p$ for broadside E_y . B_z starts with 180° phase angle and reaches $-45^\circ \pm 1^\circ$ at $14p$.

The second effect is the 180° phase drop in the amplitude zero crossing region of B_x and E_y .



2.2.3 Scalar resistivities

The spatial distribution of the scalar resistivities, calculated from orthogonal pairs of E and B field amplitudes (equation 1-5) are more or less self explaining. This, in Anglo - American literature called Cagniard resistivity, reproduces the features of the horizontal field components B_x-E_y and B_y-E_x in Chapter 2.2.2.

The zero crossing of B_x and E_y is reflected in figure 2-12 where the resistivities are calculated from these two modeled fields. Green colored regions in the color table mark areas where the synthetic HMD resistivities are within a range of 10 % deviation of the model resistivity.

Again an asymmetrical behavior is observed. In broadside mode the synthetic scalar HMD resistivity meets the halfspace resistivity of the model earlier than in the collinear fashion. To give some quantitative facts, the distances where the error drops below 10 % is 4 skin depths in broadside and 5 in collinear mode.

In contrast figure 2-13 shows a quite symmetrical behavior. The minimum distance from the source to get a 10 % accurate reading is 4.5 p in both azimuths regarding the source polarization. The according ranges for the phases of the scalar HMD resistivities plotted in appendix II÷7 are 10 p respectively 6.6 p for broadside resp. collinear B_x-E_y and 8.7 p when using B_y-E_x . The relevant deviation is 1° as in Chapter . By comparison the ranges for an error of 2° are 7 p resp. 5 p and 6.6 p .

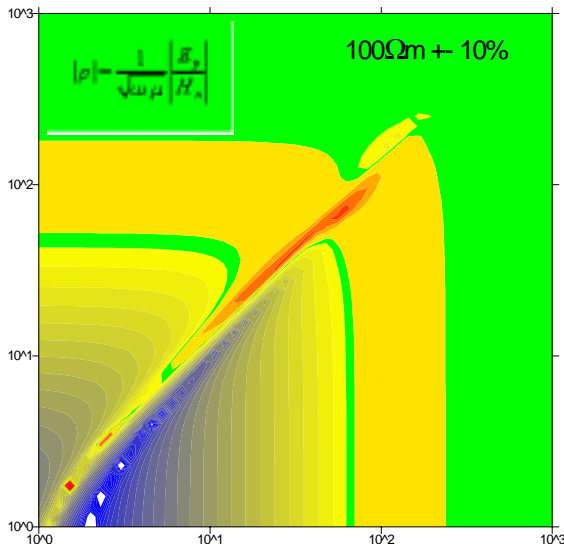


Figure 2-12 Scalar resistivity calculated from B_x and E_y due to the HMD at (0,0) as in chapter 2.2.2.

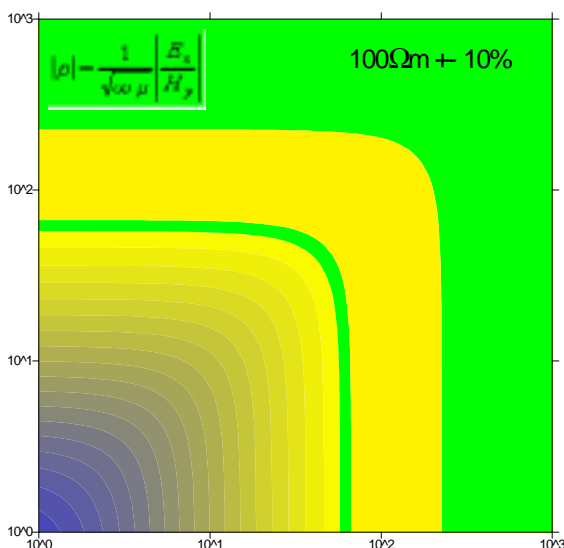


Figure 2-13 Scalar resistivity calculated from B_y and E_x due to the HMD at (0,0) as in chapter 2.2.2.

2.2.4 RMT tensor resistivities

As discussed in Chapter 1.1.2 (Page 12) two transmitter polarizations are needed to determine the impedance tensor and therefore the resistivity tensor. Computing these tensor values should eliminate parts of the observed source effects in chapter 2.2.3.

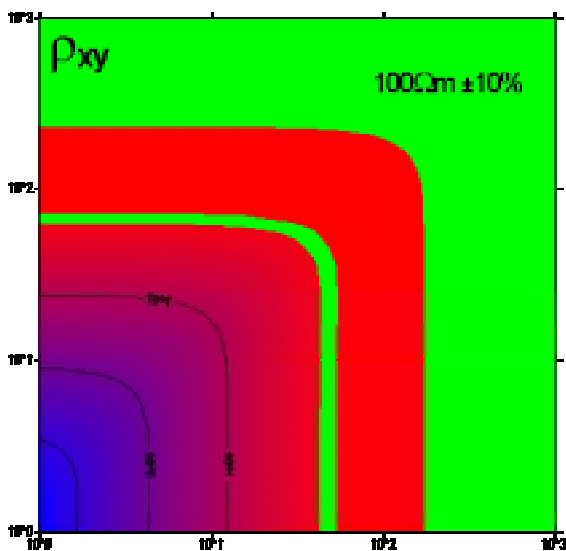


Figure 2-14 Amplitude of the resistivity tensor element ρ_{xy} over a $100 \Omega m$ halfspace. Derived from the electromagnetic field of a HMD at $(0,0)$ with two dipole polarizations.

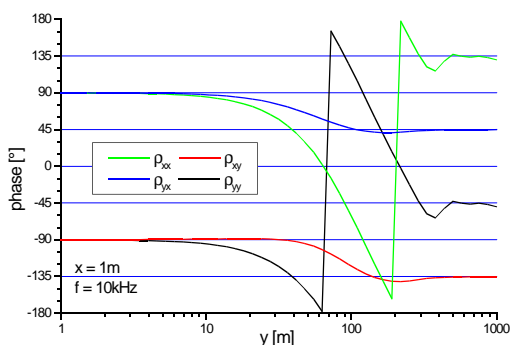
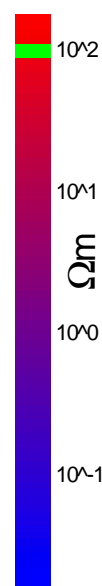


Figure 2-15 Phases of the resistivity tensor elements calculated according to fig. 2-14.

Dependency on position

Figure 2-14 shows the effect of the tensor treatment on the synthetic fields after equations 2-9 and 1-6. The calculated HMD resistivity ρ_{xy} meets the value of the model earlier or at a smaller distance from the source as the scalar determined HMD resistivities in the last chapter. In this example the ranges are $x_{10} = 3.4 p$ and $y_{10} = 4.6 p$ in x- and y- direction. x_{10} or y_{10} stand for the range between transmitter and receiver where the deviation of the calculated to the model resistivity drops below 10%. Note that the definition of the collinear and broadside mode is no longer valid as two transmitter polarizations contribute to the determination of the tensor values. In appendix II-8 the remaining elements of the resistivity tensor are plotted. The primary diagonal elements ρ_{xx} and ρ_{yy} are close to zero as they are supposed to. An interesting effect can be observed comparing ρ_{xy} and ρ_{yx} . They seem to be mirrored on the 45° axis. Even the far field distance (FFD) corresponds. Hence for ρ_{yx} the ranges are $x_{10} = 4.6 p$ and $y_{10} = 3.4 p$. This behavior can be understood when the two single transmitter polarizations are observed.



For the determination of ρ_{yx} E_y has to be taken into account. For the first transmitter polarization (on the x axis) E_y shows the asymmetrical behavior plotted in appendix II-3. In the first place the amplitude in collinear mode is stronger as in the broadside and second the distance where the phase of E_y reaches 45° shows a higher value in the collinear mode. For the second transmitter polarization E_x in appendix II-3 stands for the actual E_y in this case. Due to its symmetrical distribution it does

not influence the behavior of ρ_{yx} . Thus the asymmetrical arrangement of E_y for the first transmitter polarization is reflected in the two different far field distances $x_{10} > y_{10}$.

Consider that for one specific sounding point the whole impedance tensor has to be determined. Hence it is impossible to define a preferable measuring position as always one of the two secondary diagonal elements of the resistivity tensor is in the “bad” mode. These modes don't differ much but with a factor of roughly 1.3 which means that $y_{10}/x_{10} = 1.3$ for ρ_{xy} or $x_{10}/y_{10} = 1.3$ for ρ_{yx} .

Note that all four tensor elements reach a similar magnitude in the near field. This coincides with the estimation of a “full” impedance tensor for the existence of $E_x=E_y$ when $B_x \neq B_y$ in chapter on page . The phases of the single resistivity tensor and tipper elements are plotted in appendix II÷9. Exemplarily the phases of all elements on a certain profile heading west (parallel to the y axis) running one meter north of the source ($x=1m$) are shown in figure 2-15. All resistivities start with a phase difference of $\pm 90^\circ$ in the near field. The secondary diagonal elements meet a phase of 45° or -135° in the far field as expected for a homogeneous underground. The respective far field distances y_{10} are $8.8p$ for ρ_{xy} and $6.7p$ for ρ_{yx} . Note the same ratio of 1.3 like just before ($x_{10}/y_{10}=1.3$). Again the phase derived FFD y_{10} is greater than the one which is determined from the amplitudes (y_{10}). Mind that 1° phase deviation is much more accurate than 10% amplitude error. Comparing the two distances quantitatively yields a factor of quite accurate 2 for y_{10} / y_{10} resp. x_{10} / x_{10} . Also the primary diagonal elements tend to phases of -45° or 135° respective 90° shifted from their corresponding primary diagonal element regarding the magnetic component (for example ρ_{xx} and ρ_{yx} which both are related to B_x).

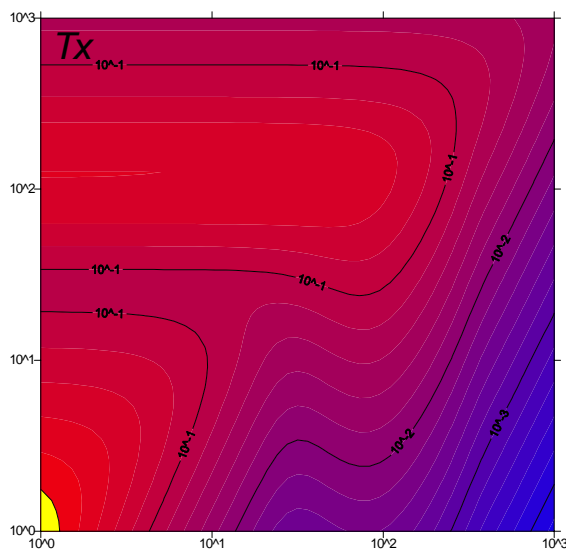


Figure 2-16 Amplitude of the tipper element T_x over a homogeneous halfspace. Derived from the electromagnetic field of a HMD at (0,0) with two dipole polarizations. The yellow area marks values above 1 %.

The amplitudes of the tipper elements remain below 1 % as they suppose to be over a 1D ground (see appendix II÷8 and figure 2-16). When studying the tipper amplitudes no near / far field discrimination is possible but the phases of the tipper elements show a similar trend as the tensor resistivities. Tipper phases start with 180° and meet -45° in the far field. In contrast to the behavior of the far field distances of the single resistivity tensor elements the spatial tipper phase distribution is exactly symmetrical and equal for T_x and T_y . The x_{10} resp. y_{10} distance equals 5.7 skin depths. In this case x, y_{10} is

more a mathematical value than an usable field factor. As the tipper

phase is not descriptive it won't be discussed in the following. The certain plots will be provided in the respective appendix pages. Not the phase, but the amplitude plays the important role for CS tipper measurements. Over a layered halfspace the source induced tipper must tend to zero to permit any measurements. As one can see in figure 2-16 this criteria is fulfilled in almost the hole area. The tipper amplitude stays below 1% outside of a 2 m distance (yellow) which is much too narrow anyhow.

Remember that in the scalar mode tipper measurements are not possible as the vertical magnetic field doesn't die off fast enough with distance. Measuring with two transmitter polarizations allows to conduct tipper measurements also under near field conditions for impedance measurements.

Dependency on frequency and resistivity

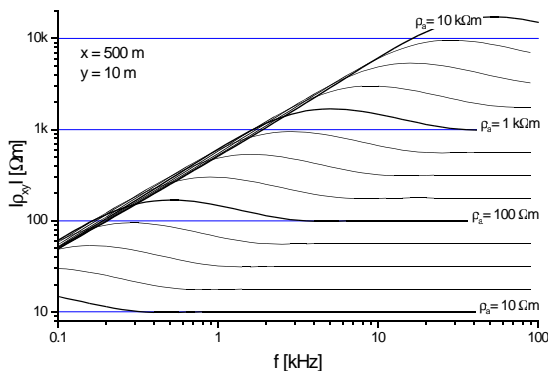


Figure 2-17 Calculated resistivity tensor element ρ_{xy} at (500,10) for different halfspace resistivities as a function of frequency. Derived from the electromagnetic field of a HMD at (0,0) with two dipole polarizations.

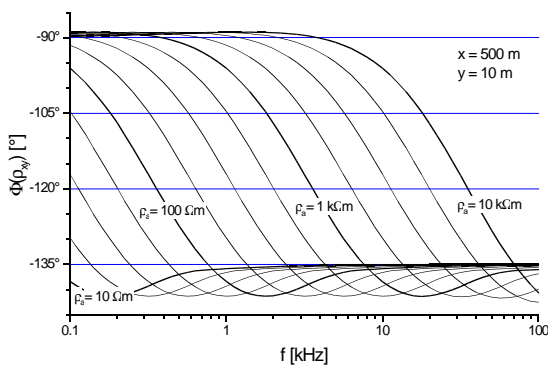


Figure 2-18 Phases of ρ_{xy} in figure 2-17.

near field asymptote where the calculated HMD resistivities decrease linear with the frequency. If the curves of several resistivities are now compared under this point of view, one can see that the far field / transition zone border is shifted to higher frequencies when the halfspace resistivity increases. As we are still regarding a homogeneous halfspace, the phases start at -90° and meet -135° in the far field independent on frequency or resistivity (figure 2-18). In contrast, the distance where it reaches this value depends nevertheless on the resistivity. The effects are comparable to the amplitude behavior. For example the frequency in which the $100 \Omega\text{m}$ phase meets 135° is 8 kHz.

As the spatial description of the modeled HMD resistivities is just a snapshot for one single frequency and halfspace resistivity, the dependency on these variables is now discussed. For better transparency one element of the resistivity tensor ρ_{xy} is picked for all oncoming investigations. It is of special interest if and how the near / far field border changes with frequency and resistivity. Figure 2-17 delivers both answers. All the curves represent simulations on one certain sounding point with the coordinates ($x = 500$, $y = 10$ m). Simulations were done for 12 resistivities from $10 \Omega\text{m}$ to $1 \text{k}\Omega\text{m}$ logarithmically spaced in a frequency range from 100 Hz to 100 kHz. The dependency on the frequency can be observed best with the curve for one halfspace resistivity, for example $100 \Omega\text{m}$. At frequencies above 3 kHz the calculated resistivity meets the model value properly thus the sounding point is in the far field. Below this frequency the transition zone to the near field starts. At roughly 200 Hz the curve meets the

2.3 Two layer case

After studying the features of calculated CSRMT measurements over a homogeneous halfspace a few examples for resistivity changes with depth are discussed in the following subchapters. As it is impossible to compute every geologically possible structure, only basic effects are considered.

In order to compare the results of the next simulations with the homogeneous halfspace responses, the MT apparent resistivity of all models is $100 \Omega\text{m}$ for 10 kHz.

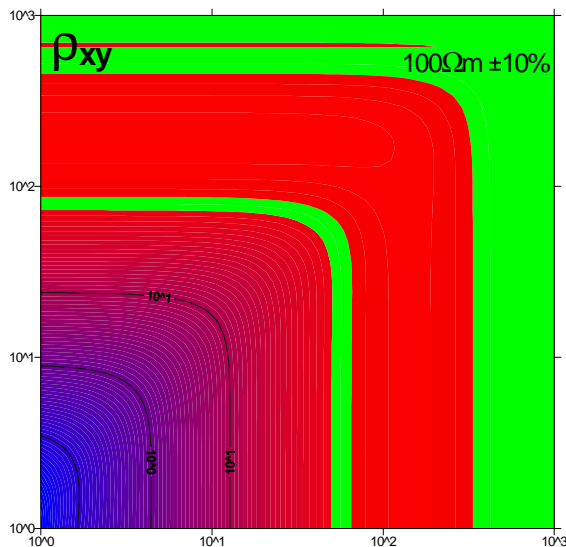


Figure 2-19 Amplitude of the resistivity tensor element ρ_{xy} over a 2 layer halfspace with conductive overburden and MT apparent resistivity of $100 \Omega\text{m}$ for 10 kHz. Derived from the electromagnetic field of a HMD at $(0,0)$ with two dipole polarizations.

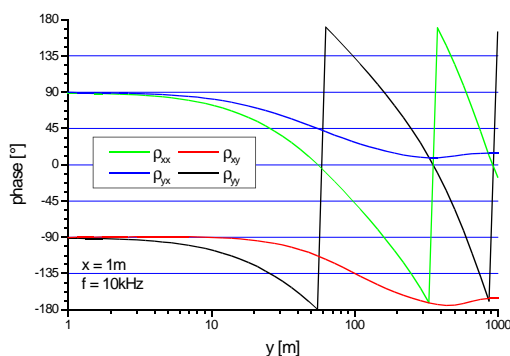
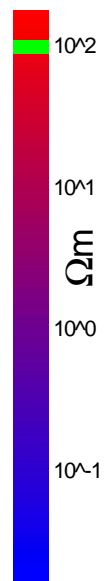


Figure 2-20 Phases of the resistivity tensor elements over a 2 layer structure with increasing resistivity. Derived according to fig. 2-19.

2.3.1 Conductive overburden

To study the spatial distribution of the calculated HMD apparent resistivities, the resistivity tensor was computed as in Chapter 2.2.4 with the following model: Over a $\rho_1 = 1 \text{ k}\Omega\text{m}$ halfspace lies a conductive layer with $\rho_2 = 10 \Omega\text{m}$ resistivity and a thickness of $t = 2.73 \text{ m}$. The phase of the MT apparent resistivity of this model is 14° . The results are plotted in appendix II÷10 and II÷11 respectively figure 2-19 and 2-20. In figure 2-19 an increase of the far field distance can be seen. The updated ranges are $x_{10} = 6.6 \text{ p}$ and $y_{10} = 9 \text{ p}$ if the little stripe where the HMD apparent resistivity reaches $89 \Omega\text{m}$ on just one sounding point in y-direction is neglected. The ratio $y_{10} / x_{10} = 1.36$ in this example. The explanation for these increased far field distances must be found in a current channeling effect of the conductive layer. Also the phases meet their far field value of 14° or -166° at greater distances. The characteristic values are $x_{I^\circ} = 12 \text{ p}$ and $y_{I^\circ} = 14 \text{ p}$. In figure 2-20 exemplary phase curves are plotted where a drastic slope of the primary diagonal elements phase can be seen.



2.3.2 Resistive overburden

To give an example for a model in which the resistivity decreases with depth, an overburden with 1 k Ω m and a thickness of 33.3 m over a 1 Ω m halfspace is introduced. Again the cumulative MT apparent resistivity for 10 kHz is 100 Ω m and the phase 84 $^\circ$ or -96 $^\circ$. The results of the simulations are shown in appendix II÷12 and II÷13 as well as in figure 2-21 and 2-22. In contrast to the conductive overburden here the far field distance decreases explicitly. $x_{10} = p$ if the single value of 112 Ω m at $x = 95$ m is neglected. Note that this range of 50 m makes no sense for the field as the geometry of the transmitter coil limits the minimum separation of transmitter and receiver. The respective relationships are given in chapter 1.2.2 on page 15. Outside of the deviation band between $y = 100$ and 180 m which reaches an error of 16 %, y_{10} equals 3.6 p . If this zone is also neglected, y_{10} would be 1.3 p . With this value y_{10} / x_{10} would be 1.3 again. Regarding the phases, it is worth mentioning that the drop of the curves is not as rapid for the primary diagonal elements as over the conductive overburden or even over the halfspace. This leads to the conclusion that the more positive the resistivity contrast is, the sharper and deeper the decline of the ρ_{xx} and ρ_{yy} phases has to be. The respective FFDs are $x_{10} = 1.3 p$ and $y_{10} = 1.9 p$ which yields a ratio y_{10} / x_{10} of 1.46.

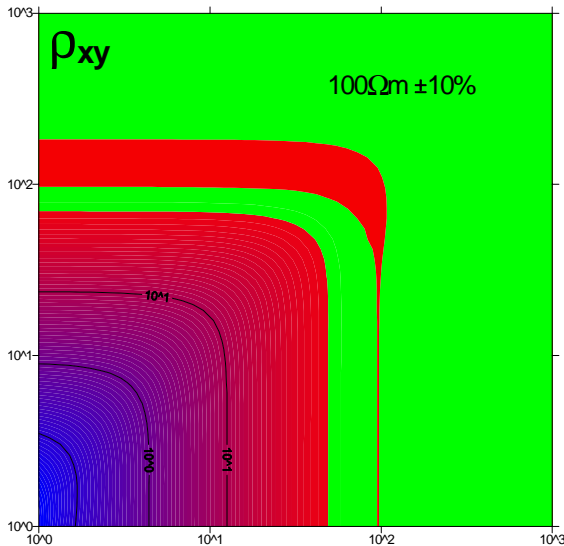


Figure 2-21 Amplitude of the resistivity tensor element ρ_{xy} over a 2 layer halfspace with resistive overburden and MT apparent resistivity of 100 Ω m for 10 kHz. Derived from the electromagnetic field of a HMD at (0,0) with two dipole polarizations.

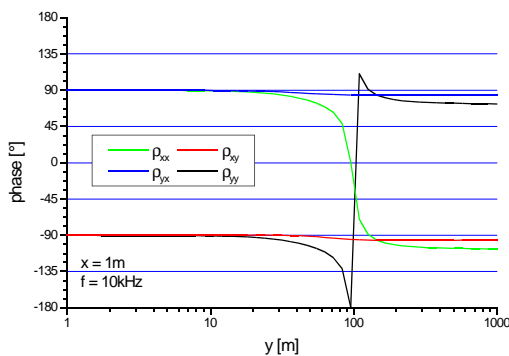
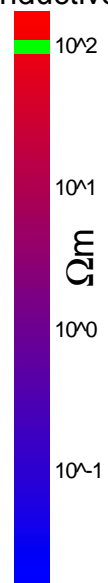


Figure 2-22 Phases of the resistivity tensor elements over a 2 layer structure with decreasing resistivity. Calculated as in fig. 2-21.



2.3.3 Dependency on resistivity contrast

After discussing two single cases of a 2 layered structure now the changes of the calculated HMD apparent resistivity tensor regarding the resistivity contrast K of the several layers is being studied.

Simulations were done with 13 different values for $K = \log(\rho_1/\rho_2)$ from -5 to 5. The particular thickness t of the layer with ρ_1 which overlays a halfspace with ρ_2 is chosen to meet an apparent MT apparent resistivity of 100 Ωm for 10 kHz. A table with the used resistivities and thicknesses is given in appendix II÷14.

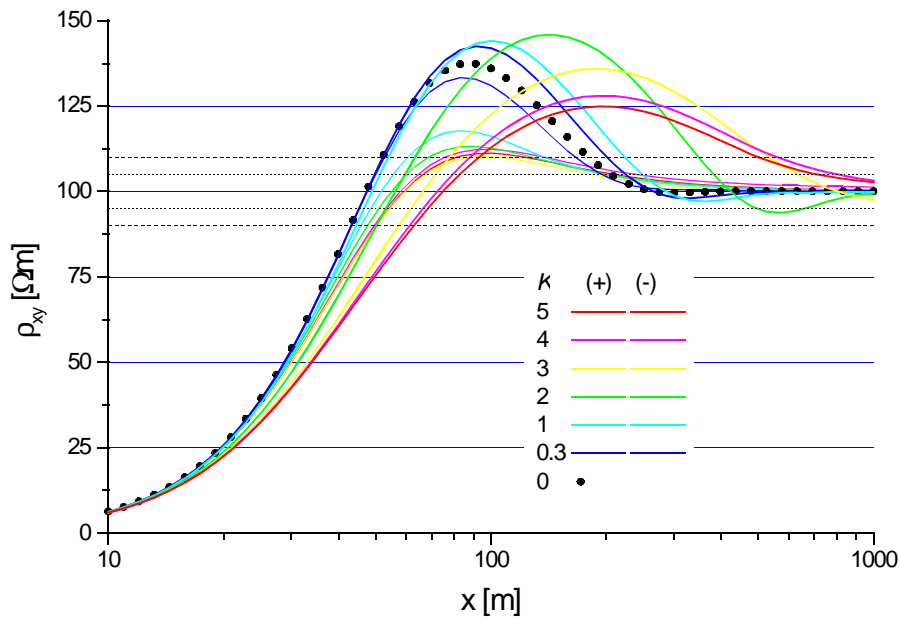


Figure 2-23 Amplitudes of ρ_{xy} along a profile in x -direction at $y = 5$ m for different $K = \log(\rho_1/\rho_2)$ with $f = 10$ kHz. Derived from the electromagnetic field of a HMD at $(0,0)$ with two dipole polarizations.

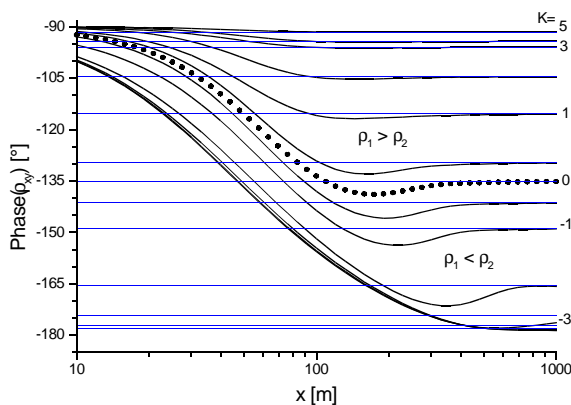


Figure 2-24 Phases of ρ_{xy} in figure 2-23.

In order to achieve transparency only the tensor element ρ_{xy} is being studied along one profile in x -direction. As it is shown in the last chapters, this configuration yields a far field distance which is less than concerning ρ_{yx} on the x axis or ρ_{xy} on the y axis. But also the ratio of these two certain distances is quite stable around 1.3. This makes it possible to transfer the one value into the other. The range x_{10} in the ρ_{xy} configuration can be understood as the minimum separation where one of the HMD apparent resistivity tensor elements meets its far field value.

Increasing the distance of 30 % sets the sounding point into the “real” far field. The way the FFD changes with K can be seen in figure 2-23. The results of the last chapters imply an increase of x_{10} with K which is illustrated now. A conductive overburden ($K < 0$) results in a more intensive change of ρ_{xy} in comparison to models with $K > 0$. Note that for $-4 < K < -0.3$ the single curves of the resistivity change much more than for $K = -5$ and -4 . This seems to be some kind of saturation effect. A resistive overburden doesn't change the calculated HMD apparent resistivity values in such a way. There are significant differences between the curves for $K = 0, 0.3$ and 1 , but for $K = 2$ to 5 the changes are quite small. As in other electromagnetic methods, good conductors influence the system more than poor conductors. In figure 2-24 (where the respective phases are plotted) one can see that there are some changes in the phase for $K > 2$.

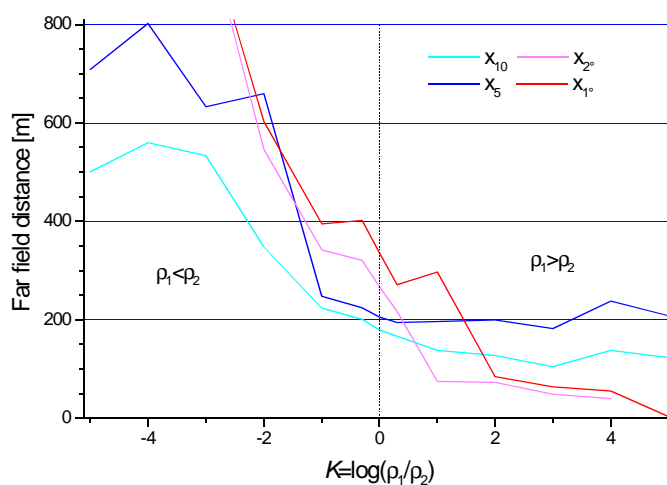


Figure 2-25 Far field distances for 5 %, 10 %, 1° and 2° deviation depending on $K = \log(\rho_1 / \rho_2)$.

Note that the FFD decreases continuously with increasing K . To evaluate the connection of x_{10} and K , different resistivity contrasts were tested with the FFD estimation program introduced in chapter 2.1.3 on page 23. Up to this point values for x_{10} , y_{10} , or x_{1° , y_{1° were picked manually. Figure 2-25 shows the results of the calculations. Mind the offset of the curves for x_5 and x_{10} respectively x_{1° and x_{2° to each other as the FFD decreases with increased allowable deviation. On the right hand side of the plot resistive overburdens are represented. The FFD stays at or just below the homogeneous halfspace value. Only when the phase criteria is taken into account, the FFD drops continuously with increasing K . On the left hand side, in which conductive overburdens appear, the FFD increases rapidly with an increasing value of negative K . Regarding the phase, the minimum far field range reaches values above 1 km early. Even when an amplitude error of 10° is accurate enough, the FFD gets almost 3 times as high as over the homogeneous halfspace. In appendix II÷15 and II÷16 some more curves for other allowable deviations are given.

The trend that the FFD increases drastically when simulations with a conductive overburden are done, generally points out a sort of current channeling in the low resistivity layer. This effect may cause serious problems for CSRMT field work.

2.4 Far field distance estimation

After studying the effects of the certain resistivity contrasts on the FFD, a field formula to estimate the minimum range between transmitter and receiver is developed now.

Therefore several calculations of the FFD x_l concerning ρ_{xy} for different frequencies from 10 Hz to 1 MHz dependent on the subsurface resistivity were done. For the frequencies 1 to 100 kHz also the 10 % deviation FFD x_{10} was computed. Appendix II-17 shows the certain curves. Note that for high frequencies and resistivities the slope changes as the quasi static approximation is no longer fulfilled. This plot can be used like similar figures for the skin depth to find out the actual far field distance in the field when the resistivity of the subsurface is roughly known which is the case in most geophysical surveys. Knowing the frequencies of the used system one can easily determine the minimum range between transmitter and receiver.

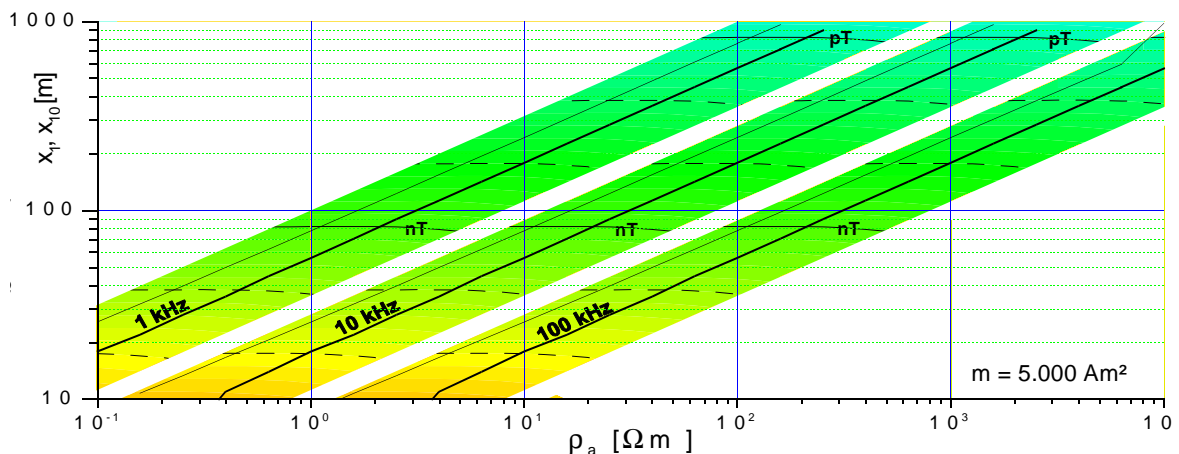
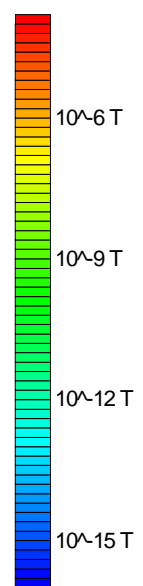


Figure 2-26 FFD and B_h for 1, 10 and 100 kHz depending on the halfspace resistivity (x_{10} as the thick; x_l as the thin line).

The second interesting magnitude for field work is the amplitude of the fields which have to be measured at the sounding point. It is clear that the maximum distance is limited by this field strength and the resolvability of the receiver. To crosscheck these two values the horizontal magnetic field was also computed for certain resistivities and distances. The magnetic field was chosen as a limiting factor as the measured electric field is increasable by a larger electrode spacing if the signal gets to low. Calculations for 1, 10 and 100 kHz are plotted in appendix II-18. Figure 2-26 shows a combined plot of the two interesting magnitudes. Exemplary x_{10} and x_l for the three frequencies are shown (x_{10} as the thicker line) with their relating B_h values in the background. This plot makes it easy to have a quick look on the estimated minimum transmitter receiver separation and to see if the used instrument is able to measure the field strength at this distance. The magnetic field in figure 2-26 is calculated with a fixed transmitter moment of 5000 Am². Working with the transmitter used for this thesis the current in the transmitter coil decreases with increasing



frequencies and thus the transmitter moment goes down. In appendix II-19 a plot like figure 2-26 is provided in which different moments for the single frequencies are taken into account. Except at 100 kHz no significant change is observed.

The curves for x_{10} respectively x_1 show a linear behavior in the double logarithmic scale. Hence a linear regression with these data was done. For the regression following relationship was assumed:

$$\log(x_1) = A(f) + B(f) * \log(\rho_a) \Rightarrow x_1 = 10^{A(f)} * \rho_a^{B(f)} \quad (2-10)$$

The results with x_1 in meter and ρ_a in Ωm are:

f [kHz]	$A(f)$	$B(f)$	SD
1	1.896	0.493	0.003
3	1.652	0.491	0.005
10	1.412	0.489	0.007
32	1.167	0.488	0.006
100	0.922	0.487	0.008

SD stands for the standard deviation of the values from the regression result. Plotting the factor A and B over the logarithm of the frequency also yields a linear dependence of the form

$$A(f) = 1.896 - 0.4867 \log(f) \approx 1.9 - 0.5 \log(f)$$

$$B(f) = 0.4924 - 0.003 \log(f) \approx 0.5 \quad (2-11)$$

$$x_1 = 10^{1.9 - 0.5 \log(f)} * \sqrt{\rho_a} = 10^{1.9} \sqrt{\frac{\rho_a}{f}}$$

which results in a field formula for the 1 % FFD of

$$x_1 \approx 79 \sqrt{\frac{\rho_a}{f}} \quad \text{with } x[m], \rho[\Omega m], f[kHz] \quad (2-12)$$

The same proceeding on x_{10} yields

f [kHz]	$A(f)$	$B(f)$	SD
1	1.75	0.502	0.003
3	1.499	0.503	0.005
10	1.237	0.507	0.014
32	0.97	0.513	0.021
100	0.744	0.503	0.003

as well as

$$\begin{aligned}
 A(f) &= 1.748 - 0.5082 \log(f) \approx 1.75 - 0.5 \log(f) \\
 B(f) &= 0.503 - 0.003 \log(f) \approx 0.5 \\
 x_{10} &= 10^{1.75 - 0.5 \log(f)} * \sqrt{\rho_a} = 10^{1.75} \sqrt{\frac{\rho_a}{f}}
 \end{aligned} \tag{2-13}$$

which delivers a 10 % FFD of

$$x_{10} \approx 56 \sqrt{\frac{\rho_a}{f}} \text{ with } x[m], \rho[\Omega m], f[kHz]. \tag{2-14}$$

Note that these two field formulas (2-12) and (2-14) have a similar form as the skin depth formula

$$p = \sqrt{\frac{2}{\omega \mu_0 \sigma}}. \tag{2-15}$$

Taking into account that $\omega = 2000\pi f[kHz]$, $\mu_0 = 4\pi 10^{-7}$ and $\sigma = 1/\rho_a[\Omega m]$ yields

$$p \approx 16 \sqrt{\frac{\rho_a}{f}}. \tag{2-16}$$

Both p and x_1 or x_{10} depend on $\sqrt{\rho_a/f}$ just with different scaling factors. Building the ratios of these parameters delivers the following dependencies:

$$\begin{aligned}
 x_{10} &\approx 3.5p & (x_{10} = 3.520p) \\
 x_1 &\approx 5p & (x_1 = 4.949p)
 \end{aligned} \tag{2-17}$$

Remember these are the minimum ranges which have to be increased by 30 % to get into the definitive far field.

2.5 Summary of the modeling results

For the sake of clarity the most important properties of the electromagnetic field of a horizontal magnetic dipole as well as the resulting calculated HMD apparent resistivities are given in the following list.

- The amplitudes of the fields and HMD apparent resistivities meet the far field condition at smaller distances from the source than the respective phases.
- In the collinear mode the magnetic field contains a vertical component with a significant magnitude which has to be taken into account if scalar tipper measurements are conducted. As the vertical field tends to zero in the broadside mode, the determination of the tipper vector eliminates this effect due to the incorporation of two transmitter polarizations.
- The spatial distribution of the horizontal electric and magnetic field shows a difference of the specific amplitudes in collinear and broadside mode. The amplitude in the line of the transmitter polarization is twice as high as in the broadside mode.
- The far field distances of tensor resistivity values are smaller than the FFDs of scalar derived resistivities. Regarding the resistivity tensor element ρ_{xy} the FFD in y- direction is thirty percent greater than in x- direction. This effect is vice versa for ρ_{yx} .
- The presence of a conductive overburden affects the far field distance strongly. A resistivity contrast of just two magnitudes at least doubles the FFD. Minimum ranges between transmitter and receiver beyond one kilometer are reached quickly.
- A linear dependency between far field distance and skin depth was found. The deviation between the amplitudes of the HMD- and the MT apparent resistivity reaches one percent at five skin depths respectively ten percent at 3.5 skin depths.

3 Instrument

3.1 Receiver

The RMT receiver used in this work was developed in the finished research project with the title “Klärung des methodischen Potentials einer vielkanaligen geophysikalischen RMS-Apparatur mit HTSL-SQUID”. The aim of this project was to evaluate the potentials of SQUID magnetometers for geophysical EM methods. A detailed presentation of the system can be found in Radic and Burkhardt (2000).

3.1.1 Technical specification

A brief description of the main parameters of the receiver is given in the following table:

Channels	5
Sampling frequency	2.5 Mhz
A/D resolution	16 bit
Bandwidth	400 Hz – 1.25 Mhz

Further highlights are 8 digital down converters (DDCs) which extract single frequencies from the time series and a digital signal generator which provides a sine voltage for calibration purposes.



Figure 3-1 Picture of the RMT receiver with connected control laptop.

The system is powered by internal chargeable batteries which last for approximate one field day.

The five channels are used to measure 3 magnetic and 2 electric fields simultaneously. Magnetic signals are picked up with a triple of orthogonal



Figure 3-2 Picture of the magnetic sensors.

shielded coils. Figure 3-2 shows the three copper pipe loops which cover the coil windings from electric fields. The specifications of the B sensors are given in the next table:

Channels	3
Area	0.5 x 0.5 m ²
Windings	5
Bandwidth	1 kHz – 1.25 Mhz
System noise	1 fT/√Hz

Both magnetic and electric sensors are connected to the receiver by a 10 m BNC cable. The preamplifier for the electric fields converts four poles and one common ground. Hence it is possible to work in X- and L- layout. Both electric and magnetic preamplifiers have an individual power supply which has to be charged after the field day. The technical data is given in the following table:



Figure 3-3 Picture of electric preamplifier.

Channels	2
Dipole	1 – 16 m
Bandwidth	DC – 1.25 Mhz
System noise	<10 nV/√Hz

3.1.2 The control panel

After the preprocessing in the receiver the measured data are transferred to the control laptop where the saving and final field processing is done. The control of the measurement and calibration is also conducted by this computer. For this purpose a LabVIEW™ program had been developed during the mentioned

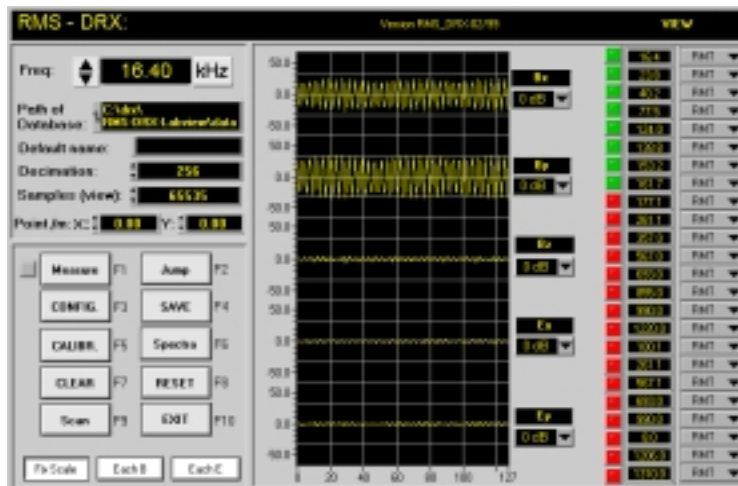


Figure 3-4 Screenshot of the front panel of the RMT control program.

finished SQUID project. In figure 3-4 a typical screen during a measurement is shown. In the central part the time series of the specific channels can be observed to check data quality and saturation of the A/D converters. The displayed time series are already downconverted which means that they contain just a narrow frequency bandwidth. On the upper left side the actual measuring frequency can be chosen and some configurations can be made. The lower left side contains buttons for certain subroutines like calibration, configuration or scanning for transmitter frequencies. On the right hand side it is possible to set the frequencies for the measurement.

This was the status of the controlling software which had to be adapted for CSRMT requirements. The following main changes were necessary:

- Adapting an existing transmitter control program to find the resonance frequencies of the system
- Introducing the communication with the transmitter via serial bus or radio modem into the measuring program
- Adding a CSRMT mode to the front panel of the measuring program
- Reworking the sounding and processing routine for the altered requirements due to the source mode

A few comments on the single tasks are given in the following.

Adapting the source control routine

As it will be shown in chapter 3.2.1, the transmitter contains a serial resonance circuit. To find the resonance frequencies for the given capacitor combinations, the stimulation frequency has to be varied in small steps.

First the program calculates the necessary capacity for a chosen frequency using an estimated value for the inductivity of the transmitter coil. A combination of the built in capacitors, which meets the desired capacity best, is activated. The system is stimulated with the chosen frequency which is changed to higher or lower values depending on the observed current in the coil. When this current reaches a maximum the resonance frequency is found. Measurements of this kind can be found in chapter 4.2.1.

Communication

The transmitter is connected to the field computer via the serial port. For communication a DOS program was provided.

As the Metronix company kindly provided a radio modem, it was possible to control both receiver and transmitter with just one field laptop. Therefore the communication between laptop and transmitter respectively laptop and receiver had to be separated. This caused no technical problem as the receiver uses the parallel port of the notebook. For the software it was necessary to avoid a simultaneous use of both ports.

The DOS source control executable asks for a hexadecimal code containing the information which relays in the transmitter have to be switched. The DOS program converts this code into certain signals on the serial port. Due to this fact, the CSRMT control program doesn't run under Windows NT. Depending on the given tasks, the LabVIEW™ control panel creates a batch file containing all needed callings of the DOS executable file.

The new front panel

The so called front panel of the CSRMT control program is the main level from where all functions are started or configured. Here it is possible to check the signals at the used frequencies as time series or spectra before starting a sounding. In this View-mode the system is acquiring and plotting data continuously. If the frequency is changed, the digital downconverters of the receiver provide the laptop with data containing this frequency information. When using the active mode not only the receiver but also the transmitter changes the active frequency. A frequency change of the transmitter contains the following steps:

- ✓ Turning the stimulation amplitude down to zero
- ✓ Switching off the amplifier
- ✓ Setting the relays for the capacitors
- ✓ Setting the relay for the transmitter polarization
- ✓ Switching on the amplifier
- ✓ Setting the stimulating amplitude and frequency to the adjusted value

Once tuned in to one frequency it is possible to change the amplitude of the stimulating signal in the transmitter to find the best compromise between proper received signal and low amplitude in the transmitter to save battery power and prevent the amplifier of getting too hot. When the optimum configuration is found, the amplitude can be taken into account for the following sounding. It is possible to work with different stimulation amplitudes for each individual frequency.

Note that when the single channels are checked for maximum saturation at the selected frequencies, the displayed time series or spectra contain only a narrow frequency bandwidth. To see the data without any preprocessing, one must check the saturation with the scan routine where unprocessed time series are transferred to the laptop and are displayed without any manipulation. This is a way to see the raw field data which is also used for some measurements in

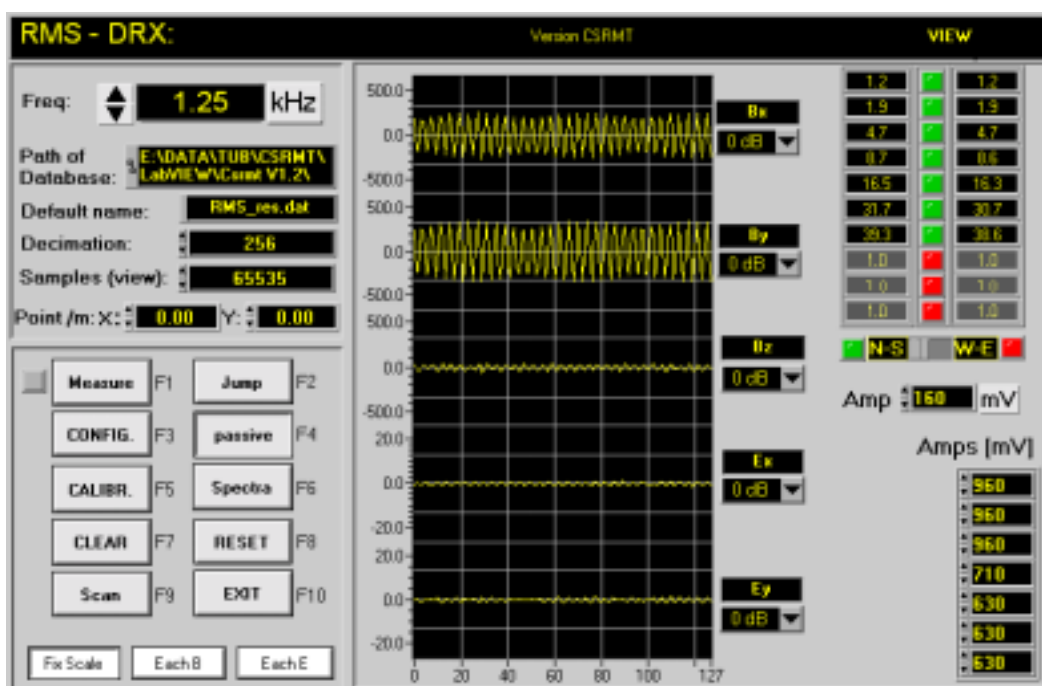


Figure 3-5 Screenshot of the CSRMT control program.

chapter 4.2.3.

The finally designed CSRMT control panel shown in figure 3-5 contains the tools to work with the transmitter from the laptop which is connected to the receiver as well. On the upper right corner the various selectable frequencies for both transmitter polarizations are displayed. They were determined as described before. The LED like looking buttons between the specific almost equal frequencies for the different polarizations allow to choose if they should be used for the sounding or not. Below this frequency block a switch to set the currently used transmitter polarization is provided. The next control with the title “Amp” allows to set the actual stimulating amplitude in the transmitter in mV. The list in the lower right corner contains the amplitudes “Amps [mV]” which will be used for the single frequencies in the sounding. The button next to the letters “F4” on the

left side of the screen switches from the active to the passive measuring mode. After clicking the button or pressing the F4 key the screen will look like figure 3-4 again.

The new sounding routine

The use of digital down converters (DDCs) enhances the speed of passive RMT measurements. The basic principle is measuring one time series, preprocessing the data with 8 DDCs simultaneously and transferring 8 decimated binary data sets to the laptop. As explained before, a DDC extracts a narrow band around a given frequency from the raw data. The result is again a time series with less data points than before. As measuring time decreases as the amount of data which has to be transferred decreases with the decimation.

As one active measurement contains just one frequency, this procedure had to be changed. Conducting CSRMT measurements, the polarization of the transmitter or the frequency of the DDC and the transmitter are alternately changed. Measuring time increases as several registrations and decimations have to be done. As the switching of the transmitter takes a certain time the measuring routine must wait for the transmitter before the next registration is started.

When all the data is collected the processing is also different from the passive type. As one single measurement contains all frequencies and polarizations in the passive mode, the impedance tensor can be calculated directly from this information. Dealing with the controlled source yields a number of data sets which have to be combined to determine the tensor information. Therefore the data has to be sorted and joined in a way that it fits for the passive tensor calculation routine.

Optionally the results of the CSRMT measurement can be combined with the passive data to one continuous sounding.

3.2 Transmitter

Figure 3-6 shows a principal sketch of the transmitter. The basic features are:

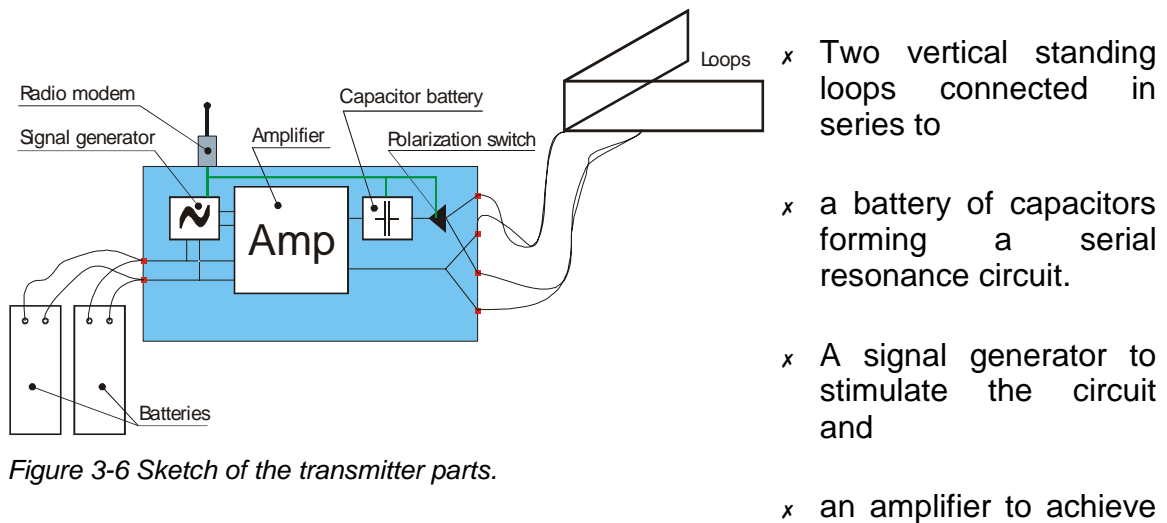


Figure 3-6 Sketch of the transmitter parts.

high currents.

The provided system (except the signal generator) was a prototype contributed to the SQUID project by the Metronix company, but was never used in this project.

3.2.1 Technical description

Before describing the alterations to the system the single components are briefly introduced in the following.

The signal generator

was built by “Linau industry electronics” and works in a frequency range from 0 to 250 kHz. Its output voltage reaches up to 960 mV in 13 linear spaced steps. As it just acts as stimulating input for the amplifier, the maximum current is irrelevant. The generator is controlled by the serial port of the notebook directly. The generator is connected to the relays of the capacitors via a zero modem cable.

The amplifier

is a 250 watt (at 4 Ω) mono car audio amplifier. It is a Rockford Fosgate® “Punch 250.1 power” with a specified bandwidth of 10 Hz to 200 kHz. The power rating of the manufacturer yields a frequency range from 20 Hz to just 20 kHz with less than 0.1 % total harmonic distortion. The casing consists of an aluminum cast heatsink.

The capacitors battery

consists of fourteen capacitors from 10 μF down to 470 pF. They are spaced 10, 4.7, 2.2, 1, 0.47, ... to reach specific values most accurately. Relays allow to connect them in parallel. The maximum capacity is therefore $\approx 18.78 \mu\text{F}$.

The loops

are made of high voltage cables with 5 wires which are connected in a way that they represent loops of 5 turns. The cables have a length of 25 m to form a 10 x 2.5 m² rectangle in the field. The loops are mounted on overall 5 rods which



Figure 3-7 Built up transmitter loops in the field. The loop cables are highlighted by orange lines.

are tightened to the ground with straps to keep them in a vertical position. The layout of the coils is equivalent to an L, where one is oriented to the west and the other orthogonal to it. A typical field layout can be seen in figure 3-7.

Due to the different resonance frequencies it is important that for each polarization the same loop cable is being used for every field day.

3.2.2 Improvements

At the beginning of this work the transmitter was supplied with an external signal generator. The control laptop was connected to the signal generator and from there to the relays for the amplifier and capacitors. Because of intense heating the case had to be opened most of the time to cool the amplifier. Figure 3-8 gives an impression of how this looked like in the field. To

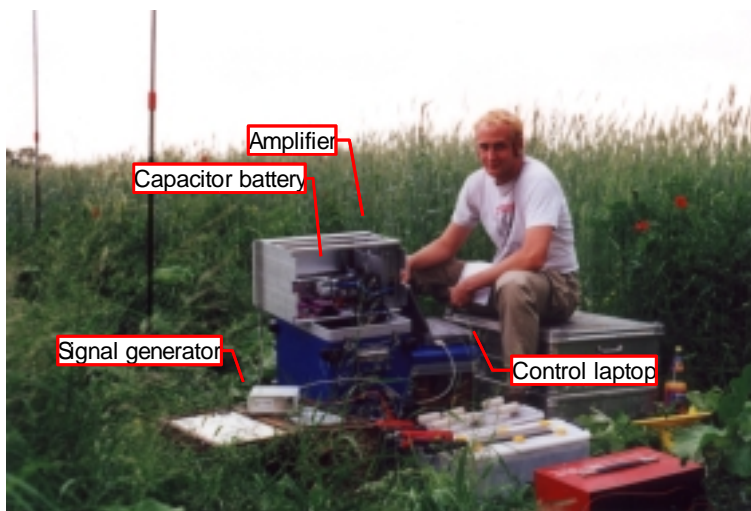


Figure 3-8 The start up configuration of the RMT source.

the left of the blue transmitter casing two of the rods to mount the loops can be seen. Next to the two batteries stands the 30 A battery charger connected to a power generator approximately 50 m away.

Regarding the transmitter two main problems had to be solved:

- Excessive power consumption and
- “system melting” heat production.

Power supply

The problem with the immense power consumption of roughly 55 A DC while transmitting was solved with the help of a 2 kW power generator in the field. During the measurements the two 143 Ah batteries for the transmitter were charged continuously by a 30 A 12 V battery charger. This prevented the transmitter from going down just after approximately 5 hours. With the permanent charging it was also possible to measure on several days, as it would have been impossible to charge two 143 Ah batteries over night.

After this change a new problem arose. The signal generator stopped to react to program calls when the power generator was running. It turned out that the signal generator was sensitive to supply voltages beyond specifications. To prevent this problem a voltage regulator was installed.

Heat production

Besides the power supply the more serious problem seemed to be the overheating of the amplifier and the capacitors at high currents.

It happened quite soon that one of the capacitors melted under field conditions. The problem of the system layout is, that at certain desired capacities just a few or even only one or two capacitors are switched on. Then the whole current of the system (up to 50 A) runs through these two or three capacitors and heats them up. Even when more capacitors are being used, more than half of the current flows through one capacitor. In figure 3-9 the distribution of the current through the single capacitors is shown. Capacitor #1 stands for the one with 10 μF . The capacity decreases with increasing number (for example cap. 10 \cong 10 nF). A listing of all the capacitors and percentile currents is given in appendix III÷1. Note that the 0.22 μF capacitor (cap. #6 in figure 3-9) melted when working with 8 kHz. This melted capacitor was replaced by a stronger type of the same capacity. For

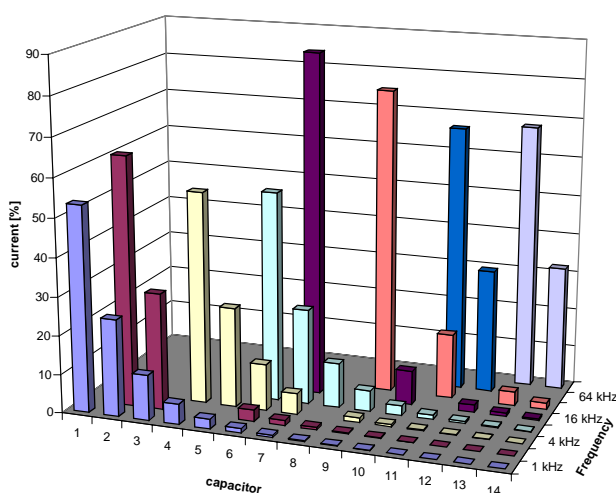


Figure 3-9 Distribution of the system current among the single capacitors of the transmitter for different frequencies.

the used frequencies of 1, 2, 4, 8, 16, 32 and 40 kHz the rest of the capacitors were quite stable. Tests with frequencies between 40 and 200 kHz showed rapid temperature increases at the used capacitors and besides that a breakdown of the amplifier which will be discussed later.

Generally the performance of the system is limited by the amplifier. Although it ought to be able to handle frequencies up to 200 kHz it fails already around 30 kHz. The amplifier seems to be not fast enough to provide the output with a high frequency sine current. This can be seen using an oscilloscope.

Especially at these high frequencies the casing of the amplifier gets extremely hot. To transport the heat from the amplifier out of the transmitter housing a ventilation system with a powerful 12 V fan was installed. To avoid overheating damages of the amplifier a temperature controlled security switch off had been integrated. Nevertheless the amp broke down two times. The first time it was repaired by the manufacturer without charge who gave the information that



Figure 3-10 The reworked transmitter system with radio modem.

exactly this security switch broke and didn't switch on again. The second time the heat load had been more damaging and the power transistors were broken and black from smoke or flames. This was the moment when we stopped investing any more time and energy in this system as it didn't meet the requirements. Figure 3-10 shows the transmitter after all alterations were finished. The signal generator is mounted internally and a radio modem is connected instead of the laptop. The two circular grids on the left side of the top of the casing are the air in- and outlet for the cooling fan. The batteries are connected to a charger when profiling work is done.

4 Measurements

4.1 Laboratory

4.1.1 Transmitter output

Before the transmitter was taken out to the field, its characteristics were evaluated during measurements in the laboratory.

The amplifier was stimulated with a manually adjustable signal generator. One of the loops was laid out on the floor to simulate the interplay of capacity and inductor. Varying the stimulation frequency of the signal generator the resonance frequencies for the specific capacities were found rapidly. The lowest achieved frequency was 1.33 kHz when all capacitors were switched on ($\cong 18.8 \mu\text{F}$) and the maximum was reached at 165 kHz with no activated capacity. For this frequency range two different investigations were carried out.

First the stimulating voltage was increased until the amplifier reached its maximum deliverable current at the certain frequency or the temperature of any active capacitor reached a dangerous level. At frequencies above 30 kHz the heat production of the capacitors limited the performance of the system. The rapid temperature increase allowed maximum transmitting durations of only one minute. Besides the capacitor temperature the harmonic distortion of the amplifier restricted the performance. In detail at 35 and 66 kHz the heat production respectively at 142 and 165 kHz the harmonic distortion limited the maximum

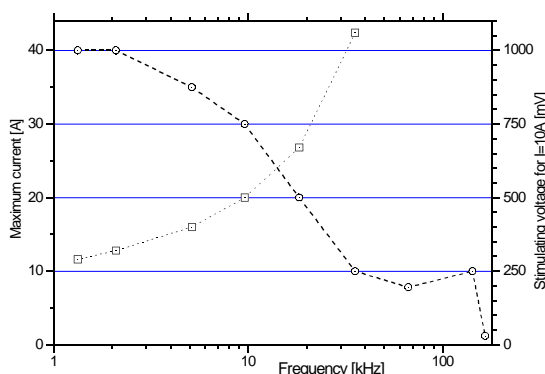


Figure 4-1 Maximum achievable current of the amplifier and needed voltage for 10 A system current.

reachable current in the loop. The dashed line with the circles in figure 4-1 shows the reached currents for the specific frequencies. In the field it turned out that at lower frequencies the capacitors were not the problem, but the amplifier went too hot when the transmitter was active for several minutes.

The second observed value was the voltage which was necessary to produce a current of 10 A in the loop. These voltages are plotted as a dotted line with open boxes in figure 4-1. For frequencies over 35 kHz no voltages are displayed as the maximum achievable currents lay below 10 Amperes. Note that the maximum voltage of the system signal generator is 980 mV.

As a result of these tests the maximum transmitter frequency for the field was set to 40 kHz to prevent the system from heat damages. Besides the temperature problem the current amplitudes are very small at higher frequencies anyway. For the two “high” frequencies 32 and 40 kHz a security routine was implied into the control program which switches the signal generator off after one minute transmitting time.

4.1.2 Calibration

The CSRMT control program is provided with the possibility to calibrate the system. During this calibration the effects of the sensors, preamplifier, cables and the receiver systems like A/D converter etc. are eliminated. As only ratios of certain field pairs like E_x / B_y or B_z / B_x are important to determine the impedance and tipper, only these ratios are calibrated.

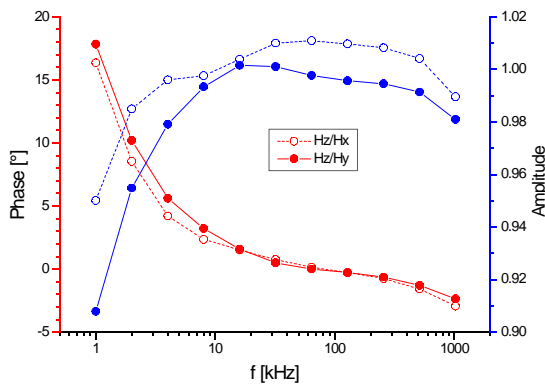
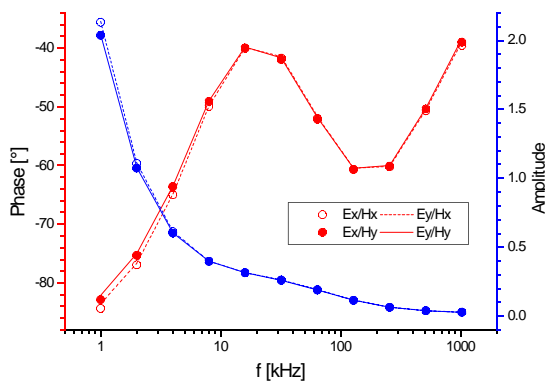


Figure 4-2 Calibration curves for $B_z / B_{x,y}$.

Figure 4-3 Calibration curves for $E_{x,y} / B_{x,y}$.



The technical layout is described in the following. The receiver coil triple is brought into a position where all magnetic dipoles are oriented downwards with the same inclination. Around the antennas a horizontal single loop is placed with the coil triple in the center. The coupling between the horizontal calibration coil and the single receiving loops is equal, which yields a ratio of $B_z / B_x = B_z / B_y = 1$. To measure the electric fields as well, a resistor is integrated in the calibration loop wire on which the voltage for the E field is picked up. The channels E_x and E_y are connected to the same resistor. This yields values of $E_{x,y} / B_{y,x}$ which are a function of the resistance and the mutual inductance of the calibration loop and the receiver coils. When a calibration measurement is conducted, the sixth channel of the receiver which supplies the calibration signal is connected to the calibration coil. It delivers sine signals with the desired calibration frequencies. During the calibration loop is transmitting the ratios of the single fields are acquired with the receiver. The results of a calibration

like this are shown in figure 4-2 and 4-3. The frequency dependency of the amplitude and phase is also influenced by the frequency depending characteristics of the gain of the preamplifiers and the sensitivity of the receiver loops. The properties of the A/D converters and of the cables running from the sensors to the receiver also influence the system. The datapoints for the single channel ratios are stored in a calibration file. When measurements are done in the field calibration values for the actual frequencies are calculated using a polynomial interpolation between the data points in the calibration file. A result of such a fitting can be seen in the following chapter.

4.1.3 Control program verification

As described before, the measurement control program was revised to involve the controlling of the transmitter as well. To test the function of this routine a CSRMT measurement was simulated in the laboratory. Therefore the calibration coil acted as the transmitter. This loop was connected directly to the signal generator of the transmitter system. The receiver sensors were placed in exact the same position

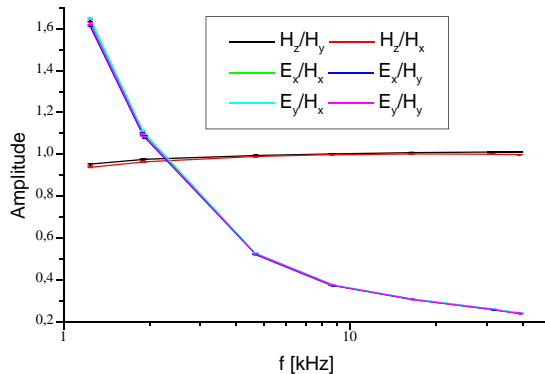
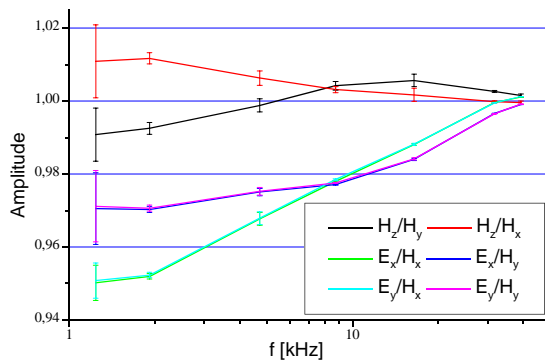


Figure 4-4 Uncorrected amplitudes of the field ratios acquired at a simulated CSRMT measurement using the calibration coil as transmitter.

Figure 4-5 Corrected (calibrated) amplitudes of the



field ratios acquired according to fig. 4-4 at the frequencies of the NS loop.

as during calibration. In this configuration it is possible to check the correct timing of frequency changes in the transmitter and receiver. Figure 4-4 and appendix IV÷1 show the results of such a measurement. The ratios of the fields behave, as expected, like during the calibration. Also the effects of the calibration were tested in this measuring layout. The results of a correction with the formerly acquired calibration data are shown in figure 4-5 for the frequencies of the NS loop. In figure 4-4 the frequencies for both polarizations are plotted. Due to the smaller data range in the calibrated plot, the resolution is high enough to show little offsets between the data points for the single frequencies. Because of this the plots for the different polarizations were separated. Graphs for the not shown polarization and the phases can be found in appendix IV÷1 to IV÷4. Furthermore figure 4-5 shows an increased measuring error for 1.24 kHz compared to the other frequencies. This dataset consists of only 4 stacks but the high error level is not removable with excessive stacking. The origin of this error could not be found definitely, but it seems to be due to the frequency is near the end of the bandwidth of the receiving system.

Besides this failure the calibrated values show a deviation less than 5 % which is satisfying. These test measurements deliver a system accuracy of 5 % for the amplitude and 1.5° for the phase.

4.2 Field

As the transmitter was a prototype and not ready for the field, a lot of time and energy had to be invested to achieve a field capable condition both in the laboratory and field. Unfortunately no sounding data could be acquired during the numerous transmitter tests before its conclusive breakdown.

4.2.1 Resonance curves

To find the exact resonance frequencies of the system the equipment was built up in the field and the current in the transmitter loops was measured for different stimulating frequencies. The system was controlled with the program introduced in chapter 3.1.2 on page 48. Figure 4-6 exemplarily shows one of the curves for a

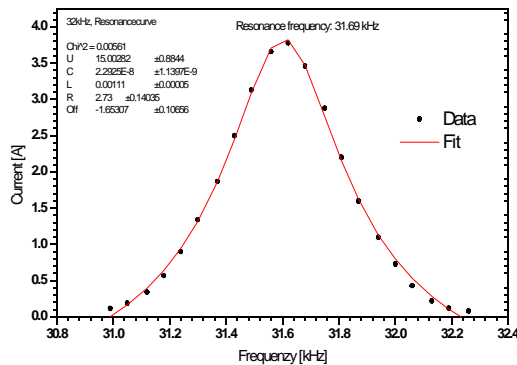


Figure 4-6 Current in the transmitter loop depending on the stimulating frequency with capacitors activated for 32 kHz.

desired frequency of 32 kHz. In appendix IV÷5 to IV÷7 plots for 1, 8 and 100 kHz are supplied. The measured data points were fitted with the equation for the current in a serial resonance circuit which is given by

$$I(\omega) = \frac{U}{\sqrt{R^2 + (\omega L - 1/\omega C)^2}} \quad (4-1)$$

As the data are shifted on the current axis an offset (Off) was implied into the fitting formula as additional parameter. The results of these fittings are plotted as red lines in the figures. The calculated values for U , R , L , C and the offset are printed to the upper left corner of the plots. The fitting reaches a good match to the data points and the standard deviation of the single parameters remains small. With these calculated values for the capacity and inductivity the resonance frequency can be calculated with the help of $\omega = \sqrt{1/LC}$. Even though these frequencies match quite well, the values for the resistance, voltage and inductivity vary. Especially regarding R and L no changes should take place. The reason is found in the way of acquiring the current data. They were measured with a current pliers connected to a "Voltcraft M-4660A" voltmeter. This meter shows a frequency response in the displayed voltages. The frequency response is shown in appendix IV÷8. To get this curve a sine with constant amplitude but varying frequency was fed into the voltmeter. The graph shows the voltage values which the meter displayed. This frequency response explains the slightly asymmetrical appearance of the resonance curves and therefore the different values for the resistance, voltage and inductivity.

Measurements of this kind were done for all desired frequencies with both transmitter loops. The acquired pairs of system capacity and corresponding resonance frequency are introduced to the measuring program as initial values.

4.2.2 Transmitter currents

To determine the maximum possible transmitter moment in the field, the currents in the transmitter loop were measured at the highest stimulating signal level of

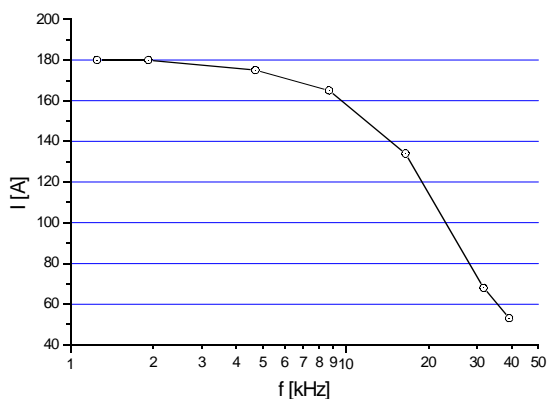


Figure 4-7 Current in transmitter loop at maximum stimulating voltage of 0.98 V for frequencies from 1 to 40 kHz.

980 mV. This test was done with both of the loops but only the data for one are plotted in figure 4-7 since there was no significant difference between the two curves. As in chapter 4.1.1 (page 56) already found out, the maximum achievable current decreases with increasing frequency. The current drops rapidly at frequencies above 20 kHz. It is also impossible to transmit for longer times than one minute at these high frequencies as the heating of the capacitors and the transmitter have to be taken into account. Thus the possibility to eliminate the low signals with higher stacking is not feasible.

4.2.3 Received signals

Due to the massive problems and breakdowns of the transmitter several field measurements were conducted, but no single “real” sounding dataset could be acquired. It turned out that one of the first measurements was supposed to be the one and only interpretable.

The aim of this field day was to verify the resolvability of the transmitted signals by the receiver at a small distance to the source. As this survey was not supposed to be processed furthermore, also the field layout was somehow spontaneous. The transmitter polarizations were roughly NNW and ENE and the receiver sensors were placed 200 m to the SSE. For sake of simplicity the transmitter polarizations will be called NS and EW in the following. It is therefore also assumed that the azimuth of the receiver is roughly 0°. The data are displayed in appendix IV÷9 and IV÷10. All of these graphs consist of four single measurements at different transmitter frequencies. The single plots display narrow frequency bandwidths. A combination of four graphs yields a spectrum containing the information of all four transmitted frequencies. The plots in appendix IV÷11 show the acquired data that contain just permanent transmitting VLF and radio frequencies. The transmitter of the system was turned off during these registrations. All graphs are scaled in bits since the absolute values of the single channels are not calibrated but just the ratios are, as it was explained in chapter 4.1.2. The displayed data represent FFT spectra of the unprocessed time series. They were acquired in the so called scan routine in which no down conversion takes place. Every time series consists of 65536 data points sampled with 2.5 MHz. Two characteristics can be observed in the data:

The signal to noise ratio at the investigated frequencies lies between 10 and 100 similar to the normally used VLF or radio signals. The spectra in the appendix show this quite well. To distinguish the transmitted “high frequencies” of 16.5 and 30.7 kHz from other permanent signals, the spectra of the “background” are provided. For instance the 30.7 kHz frequency fills a gap between the numerous other signals.

These results look fairly good, however the relative small distance between transmitter and receiver has to be taken into account. Tests with a distance of 400 m showed a dramatic decrease of the signal levels (approximately a tenth). Due to the constant troubles with the transmitter, this behavior could not be evaluated exactly but the theoretical decrease of the fields with $1/r^3$ implies such a rapid dying of.

The second feature worth mentioning is the relation between the fields at the different transmitter polarizations. The respective data is shown in figure 4-8 and appendix IV÷12 + IV÷13.

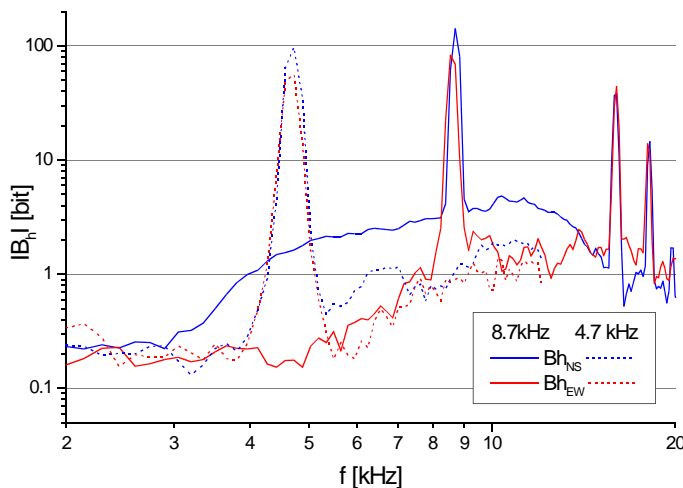


Figure 4-8 Spectra of B_h for active frequency 4.7 and 8.7 kHz in both polarizations. Acquired 200 m from the transmitter.

According to chapter 2.2.2 (page 29) the horizontal magnetic and electric field amplitudes in collinear are twice as high as in broadside mode. Observing the amplitudes of Bh_{NS} and Bh_{EW} at the transmitter frequencies 4.7 and 8.7 (8.6) kHz one can find the factor 2 in in the field data again. Concerning the measured electric fields this relation is not achieved. For the low frequency the collinear

and broadside fields are almost equal but for the 8.7 kHz signal Eh_{NS} overtops Eh_{EW} by a factor of roughly 1.5. The reason for this could be a current channeling due to a drain just next to the measuring site that runs parallel to the connection of transmitter and receiver. As reported in CSAMT literature (for example Zonge and Hughes, 1988), a conductor in such a position can influence the measurement massively. For the vertical magnetic field the collinear amplitudes are higher than in the broadside mode as well. Naturally the broadside fields won't be zero in the field although the modeling data predicts it. As described the position of the receiver is not exactly on the polarization axis of the transmitter. Also the restriction of a 1D earth is definitely not fulfilled.

Unfortunately due to the massive transmitter troubles mentioned before, no more presentable data could be acquired.

5 Interpretation concepts

5.1 Inversion of near field data

As the last chapters line out, the requirements to interpret CSRMT measurements with the standard MT plane wave solution are satisfied at quite far distances. Especially when a conductive overburden is concerned, the far field distance reaches values above 800 m. As the transmitter range limits the maximum separation between transmitter and receiver, measurements often will have to be done inside the near field or at least in the transition zone.

To interpret these “near field disturbed” data an inversion routine, taking the source field geometry into account is required. Routh and Oldenburg (1999) presented a technique for inverting CSAMT data to recover a 1D conductivity structure. Resting upon the formulation of the fields of a horizontal electric dipole (HED) as the solution of the forward problem they introduced a linearized inversion of the apparent resistivity derived from E_x and H_y of the HED over a layered earth. Unsworth et. al. (2000) introduced a 2.5D inversion for CSAMT data. An according inversion for the fields of the HMD would be a chance to achieve accurate results both in the near and far field region. An outstanding advantage would be the improved signal to noise level if the receiver could be placed near the transmitter and not several hundred meters away to stay in the far field. The following table illustrates the dependency of the specific field components over a 1D earth on ω, μ, σ and/or r :

	Near field	Far field
$E_h \sim$	$\omega \mu \frac{1}{r^2}$	$\sqrt{\omega \mu} \frac{1}{\sqrt{\sigma}} \frac{1}{r^3}$
$H_h \sim$	$\frac{1}{r^3}$	$\frac{1}{r^3}$
$H_z \sim$	$\omega \mu \sigma \frac{1}{r}$	$\frac{1}{\sqrt{\omega \mu \sigma}} \frac{1}{r^4}$

The transmitter moment m is not in the list, as it contributes to all fields directly linear. Note that the typically used ratio of orthogonal horizontal electric and magnetic field would deliver no information regarding the conductivity of the subsurface in the near field, where only H_z contains the resistivity information. For inversion a field ratio like H_z/E_h could be taken into account, as then the knowledge of the receiver moment would not be required. As long as field ratios are used, the absolute sensitivities of the receiver channels don't have to be calibrated. Besides note that the dependency of H_z/E_h on r is linear both in the near and far field. As the inversion algorithm should be able to handle near field and far field data as well this could be a major advantage.

How many receiver channels and transmitter polarizations would be needed is a subject for further investigations. The resistivity information could be extracted even from one (H_z, E_x, E_y) or two ($E_x/H_y, E_y/H_x, B_z/E_h$) acquired fields in the transition zone and far field. On the other hand using several channels could improve the results using a joint inversion. The ratios of the fields could provide

information about the dimensionality of the subsurface structure. Maybe only one transmitter polarization would be sufficient which would double the measurement speed.

It is a fact that the distance between receiver and transmitter has to be known for such an inversion. This could be the only disadvantage as it would have to be acquired in the field. Using a differential GPS to determine the position of the transmitter and the sounding points would solve this “problem” quite easily. Considering the accuracy of the measured distance, note the specific contribution of the deviation of r to the certain fields respectively field ratios.

5.2 Joint CSRMT and VLF profiling

Another interesting variation of interpretation is the combination of CSRMT and tensor VLF measurements. In this case tensor VLF stands for the passive registration of the magnetic transfer function T in the frequency range 10 kHz to 1 MHz.

Imagine a profile with several VLF sounding points. On every 5th or maybe 10th point a CSRMT sounding with frequencies down to 1 kHz is conducted. The use of the system transmitter is limited just for the CSRMT measurements. This field layout represents a profiling method which delivers a lot of data in a fast way. The building up of the E field sensors, which takes most of the time for one CSRMT sounding, can be done while the VLF soundings are acquired. The larger separation of the CSRMT measuring sites compared to the VLF sounding points is obvious as the lateral resolution at the lower frequencies recommends it.

For interpretation respectively inversion I want to refer to the tipper transformation, introduced by Becken (2000) as well as Gharibi and Pedersen (1999). They presented a way to transform VLF data into MT apparent resistivities. As one can find in these works, knowing one impedance value on the profile it is possible to calculate the resistivities on the remaining sounding points from the measured tipper. The conducted CSRMT measurements between the numerous VLF soundings can deliver this “start-” impedance on several points.

With this background it would be possible to realize a sort of joint inversion of the two data sets or to revise the tipper transform to an inversion with several boundary values. While the tipper measurements are done definitely in the far field, the CSRMT impedances might be derived as proposed in the last chapter.

6 Conclusion and Outlook

Conclusion

The aim of this work is to develop a controlled source radiomagnetotelluric (CSRMT) system. Both an instrument prototype had to be reworked and a set of model calculations had to be performed.

The controlling and processing software for the RMT receiver was adapted for CSRMT measurements. The revised control program was verified by measurements in the laboratory. A lot of time and energy was invested to rework the transmitter prototype to a field suitable instrument. Unfortunately it turned out that one of the main parts of the system, the amplifier, didn't meet the requirements for high currents and frequencies. Because of this, few presentable data could be acquired. However, some characteristics of the calculated fields could be observed in the field as well.

The decisive goal regarding the forward modelings was the detailed investigation of the far field distance (FFD). The FFD illustrates the distance between transmitter and receiver, where a specific condition is met. Mostly a certain deviation between HMD- and MT apparent resistivity is the restrictive condition. The MT apparent resistivity represents the plane wave MT resistivity of the layered model. In contrast to the MT-, the HMD apparent resistivity is determined from the spatial deformed field of the HMD on the surface of the specific layered halfspace.

Reflecting the results of the modelings, it is obvious that the far field conditions for CSRMT measurements are met at distances which can be out of the transmitter range, limited by the resolvability of the receiver. Especially in the presence of a conductive overburden, minimum separation between transmitter and receiver above 800 m is needed. Though the tensor CSRMT configuration decreases the far field distance compared to a scalar layout, this problem is not solved for impedance derived resistivity measurements, as the FFD can still force the receiver out of the transmitter range. In contrast to the impedance determination, near field effects are eliminated concerning tipper data by the two transmitter polarizations. Even "scalar tipper" measurements ($T_x = B_z / B_x$) could be conducted in the broadside mode as the vertical magnetic field equals zero there. A formula relating the skin depth and the CSRMT far field distance was developed.

To sum up, the results imply that the plane wave approximation is not adaptable for CSRMT in general. Sounding locations are either out of the transmitter range, or inside the near field respectively in the transition zone, especially in the presence of a conductive overburden. Hence the processing of CSRMT data must be done subject to the near field effects.

Outlook

One subject of future studies is the verification of the modeled spatial characteristics of the fields and transfer functions in the field. The estimation of the far field distance regarding a conductive overburden is an interesting topic in this context. The definition of the FFD in this work bases on the apparent resistivity of the layered subsurface, but how are frequency sounding data influenced by the near field?

A second interesting field of work is the evaluation of the different interpretation concepts. How can a near field / transition zone inversion be performed? Which field components and how many transmitter polarizations are decisive? Is it possible to skip the acquirement of E field data and the usage of the transmitter on specific sounding points, to combine CSRMT and tipper measurements in a joint inversion?

Acknowledgments

This work has been supervised by Prof. Hans Burkhard and I am very grateful for that. I enjoyed the atmosphere during discussions and his open minded attitude. During all the time I have been working on this topic Prof. Burkhard supported me in every possible way.

Mr. Radic drew my interest to the subject of electromagnetics during my employment as a student assistant to the mentioned scientific project. Especially regarding the numerous systematical troubles with the transmitter, Mr. Radic gave a helping hand.

Mr. Diefenbach-Moschick, the electrical engineer of the department, performed all the electrical improvements on the transmitter and inspired me with his electrical knowledge.

Mr. Schmarsow and Mr. Schenkluhn from the department's workshop helped concerning technical problems with the instrument and supplied the power generator as well as the battery charger for the transmitter.

Without a list of names I want to acknowledge all the members of the department for Applied Geophysics at the TU Berlin. There is such a friendly, warm and collegial atmosphere that it makes one feel good to work there. Special thanks to all the reviewers of my thesis!

My parents supported this work financially and hence enabled me to fully concentrate on my thesis. They also backed me up concerning the following point.

Besides all this, the most important "helpful background" who gave me the power to walk through all the dark clouds was the birth of my daughter Leola in October 2000. She motivates me every morning when I see her after she wakes up. Although this immense happening took place and changed my life completely, I found enough time to work on this thesis which would not have been possible without the backing up by my girl friend Antje. Thank You!

List of figures

Figure 2-1 Deviation of the Hankel transforms computed analytical and with a digital filter.	21
Figure 2-2 Position of the two simulated profiles.	24
Figure 2-3 Calculated amplitudes of the electric and magnetic fields caused by a HMD over a homogeneous halfspace. On the abscissa the skin depth p and the induction parameter $Ikrl$ are provided.	25
Figure 2-4 Amplitudes of B_x due to a HMD at (0,0) for x and y from 1 m to 1 km.	27
Figure 2-5 Amplitudes of B_y due to an HMD at (0,0) for x and y from 1 m to 1 km.	27
Figure 2-6 Amplitudes of B_z due to a HMD at (0,0) for x and y from 1 m to 1 km.	28
Figure 2-7 Amplitudes of B_h due to a HMD at (0,0) for x and y from 1 m to 1 km.	28
Figure 2-8 Dependency of the electric and magnetic fields on the frequency for different transmitter polarizations.	29
Figure 2-9 Dependency of the electric and magnetic fields on the halfspace resistivity for different transmitter polarizations	29
Figure 2-10 Ratio of the horizontal fields in collinear and broadside measurements	29
Figure 2-11 Phases of E_y due to a HMD at (0,0) for x and y from 1 m to 1 km.	30
Figure 2-12 Scalar resistivity calculated from B_x and E_y due to the HMD at (0,0) as in chapter 2.2.2.	31
Figure 2-13 Scalar resistivity calculated from B_y and E_x due to the HMD at (0,0) as in chapter 2.2.2.	31
Figure 2-14 Amplitude of the resistivity tensor element r_{xy} over a 100 Wm halfspace. Derived from the electromagnetic field of a HMD at (0,0) with two dipole polarizations.	32
Figure 2-15 Phases of the resistivity tensor elements calculated according to fig. 2-14.	32
Figure 2-16 Amplitude of the tipper element T_x over a homogeneous halfspace. Derived from the electromagnetic field of a HMD at (0,0) with two dipole polarizations. The yellow area marks values above 1 %.	33
Figure 2-17 Calculated resistivity tensor element r_{xy} at (500,10) for different halfspace resistivities as a function of frequency. Derived from the electromagnetic field of a HMD at (0,0) with two dipole polarizations.	35
Figure 2-18 Phases of r_{xy} in figure 2-17.	35

Figure 2-19 Amplitude of the resistivity tensor element r_{xy} over a 2 layer halfspace with conductive overburden and MT apparent resistivity of 100 Wm for 10 kHz. Derived from the electromagnetic field of a HMD at (0,0) with two dipole polarizations.	36
Figure 2-20 Phases of the resistivity tensor elements over a 2 layer structure with increasing resistivity. Derived according to fig. 2-19.	36
Figure 2-21 Amplitude of the resistivity tensor element r_{xy} over a 2 layer halfspace with resistive overburden and MT apparent resistivity of 100 Wm for 10 kHz. Derived from the electromagnetic field of a HMD at (0,0) with two dipole polarizations.	37
Figure 2-22 Phases of the resistivity tensor elements over a 2 layer structure with decreasing resistivity. Calculated as in fig. 2-21.	37
Figure 2-23 Amplitudes of r_{xy} along a profile in x- direction at $y = 5$ m for different $K = \log(r_1 / r_2)$ with $f = 10$ kHz. Derived from the electromagnetic field of a HMD at (0,0) with two dipole polarizations.	38
Figure 2-24 Phases of r_{xy} in figure 2-23.	38
Figure 2-25 Far field distances for 5 %, 10 %, 1° and 2° deviation depending on $K = \log(r_1 / r_2)$.	39
Figure 2-26 FFD and B_h for 1, 10 and 100 kHz depending on the halfspace resistivity (x10 as the thick; x1 as the thin line).	40
Figure 3-1 Picture of the RMT receiver with connected control laptop.	45
Figure 3-2 Picture of the magnetic sensors.	46
Figure 3-3 Picture of electric preamplifier.	46
Figure 3-4 Screenshot of the front panel of the RMT control program.	47
Figure 3-5 Screenshot of the CSRMT control program.	49
Figure 3-6 Sketch of the transmitter parts.	51
Figure 3-7 Built up transmitter loops in the field. The loop cables are highlighted by orange lines.	52
Figure 3-8 The start up configuration of the RMT source.	52
Figure 3-9 Distribution of the system current among the single capacitors of the transmitter for different frequencies.	53
Figure 3-10 The reworked transmitter system with radio modem.	54
Figure 4-1 Maximum achievable current of the amplifier and needed voltage for 10 A system current.	56
Figure 4-2 Calibration curves for $B_z / B_{x,y}$.	57
Figure 4-3 Calibration curves for $E_{x,y} / B_{x,y}$.	57
Figure 4-4 Uncorrected amplitudes of the field ratios acquired at a simulated CSRMT measurement using the calibration coil as transmitter.	58

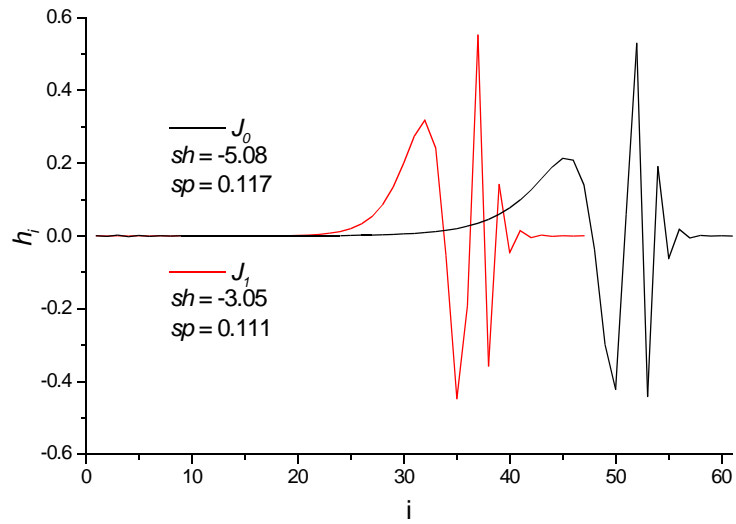
Figure 4-5 Corrected (calibrated) amplitudes of the field ratios acquired according to fig. 4-4 at the frequencies of the NS loop.	58
Figure 4-6 Current in the transmitter loop depending on the stimulating frequency with capacitors activated for 32 kHz.	59
Figure 4-7 Current in transmitter loop at maximum stimulating voltage of 0.98 V for frequencies from 1 to 40 kHz.	60
Figure 4-8 Spectra of Bh for active frequency 4.7 and 8.7 kHz in both polarizations. Acquired 200 m from the transmitter.	61

Appendix

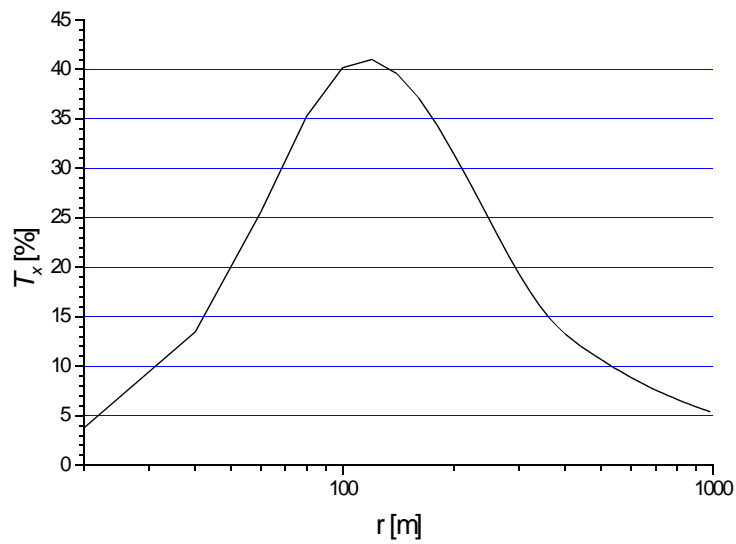
I Bibliography

- Becken, M., 2000, Interpretation of magnetic transfer functions from airborne tensor-VLF measurements: Diploma Thesis, Technical University Berlin, Germany.
- Dey, A. and Ward, S. H., 1970, Inductive sounding of a layered earth with a horizontal magnetic dipole: *Geophysics* **35**, 660-703.
- Gharibi, M. and Pedersen, B., 1999, Transformation of VLF data into apparent resistivities and phases: *Geophysics* **64**, 1393-1402.
- Guptasarma, D. and Singh, B., 1997, New digital linear filters for Hankel J_0 and J_1 transforms: *Geophysical Prospecting* **45**, 745-762.
- Pedersen, L., Dynesius, L., Bastani, M., Gharibi, M. and Matzander, U., 1999, EnviroMT. - A new radio/controlled source system: 61st Mtg. Eur. Assoc. Geosc. & Eng., Extended Abstracts, European Association Of Geoscientists & Engineers, **1**, Session:2-29.
- McNeill, J. D. and Labson, V. F., 1988, Geological mapping using VLF radio fields: *in* Nabighian, M. N., Ed., *Electromagnetic methods in applied geophysics* **2**: Soc. Expl. Geophys., 521-640.
- Radic, T. and Burkhardt, H., 2000, Klärung des methodischen Potentials einer vielkanaligen geophysikalischen RMS-Apparatur mit HTSL-SQUID: internal report, Technical University Berlin, Germany.
- Routh, P. S. and Oldenburg, D. W., 1999, Inversion of controlled source audio-frequency magnetotellurics data for a horizontally layered earth: *Geophysics* **64**, 1689-1697.
- Tezkan, B., Goldman, M., Greinwald, S., Hördt, A., Müller, I., Neubauer, F. M. and Zacher, G., 1996, A joint application of radiomagnetotellurics and transient electromagnetics to the investigation of a waste deposit in Cologne (Germany), *Journal of Applied Geophysics*, **34**, 199-212.
- Turberg, P., Müller, I. and Flury, F., 1994, Hydrogeological investigations of poroes environments by radio magnetotelluric-resistivity (RMT 12-240 kHz), *Journal of Applied Geophysics*, **31**, 133-143.
- Unsworth, M. J., Lu, X. And Watts, M. D., 2000, CSAMT exploration at Sellafeld: Characterization of a potential radioactive waste disposal site: *Geophysics*, **65**, 1070-1079.
- Ward, S. H. and Hohmann, G. W., 1988, Electromagnetic theory for geophysical applications: *in* Nabighian, M. N., Ed., *Electromagnetic methods in applied geophysics* **1**: Soc. Expl. Geophys., 131-311.
- Weidelt, P., Einführung in die elektromagnetische Tiefenforschung: lecture script, unpublished, Technical University Braunschweig, Germany.
- Zonge, K. L. and Hughes, L. J., 1988, Controlled source audio-frequency magnetotellurics: *in* Nabighian, M. N., Ed., *Electromagnetic methods in applied geophysics* **2**: Soc. Expl. Geophys., 713-810.

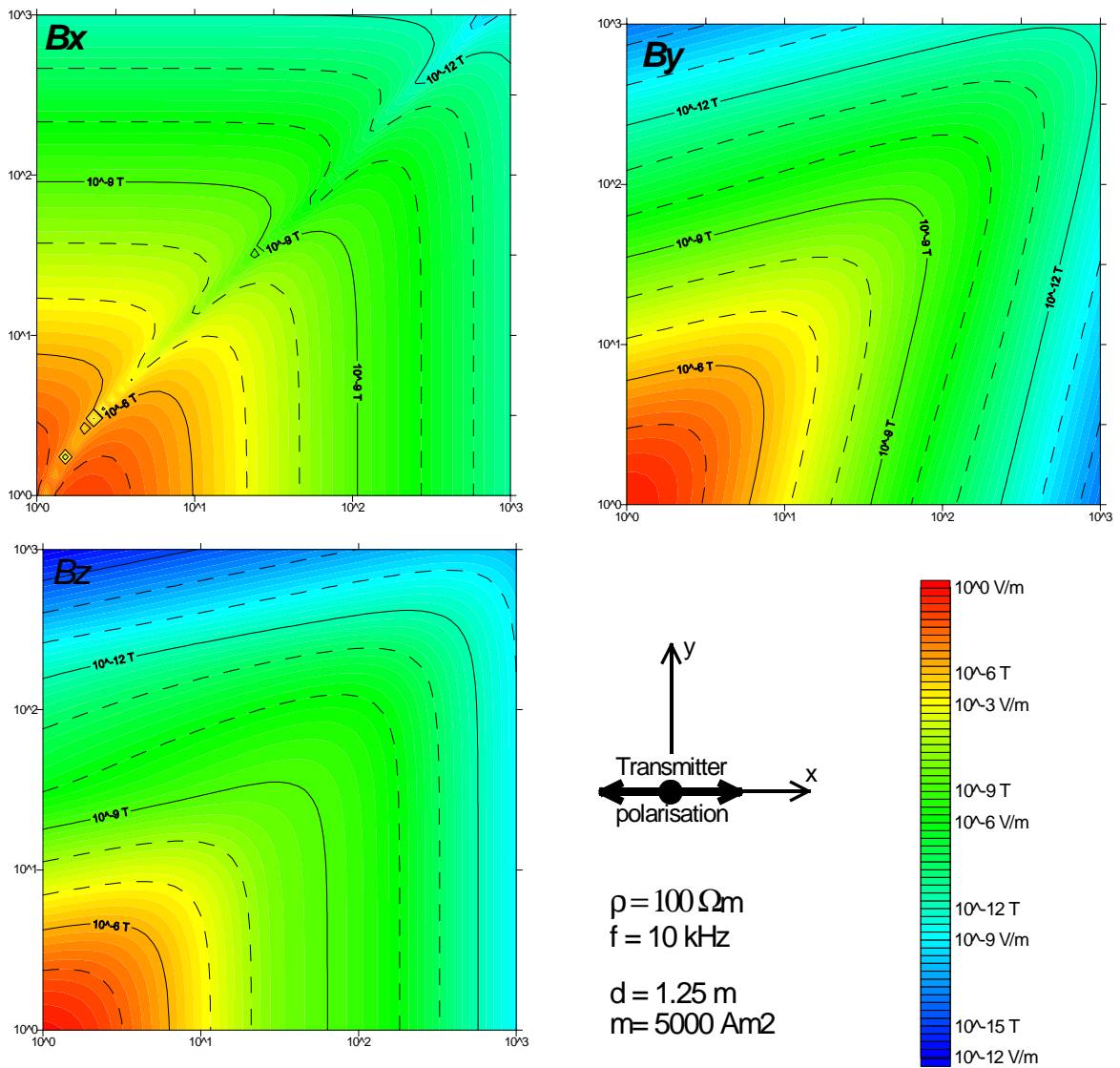
II Modeling



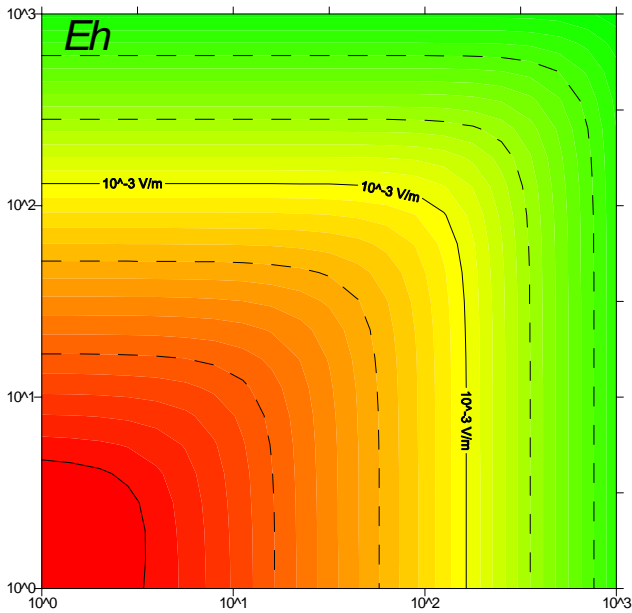
Appendix II÷1 Curves of both filter functions for J_0 and J_1 with values for sh and sp



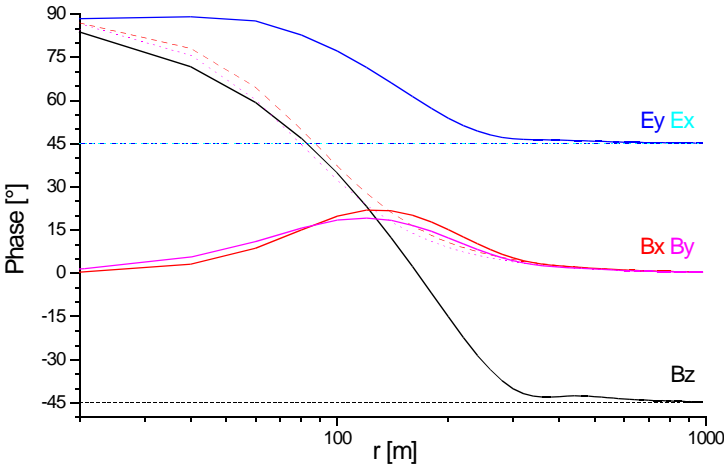
Appendix II÷2 Calculated "scalar tipper element" T_x^s out of the data of figure 2-3.



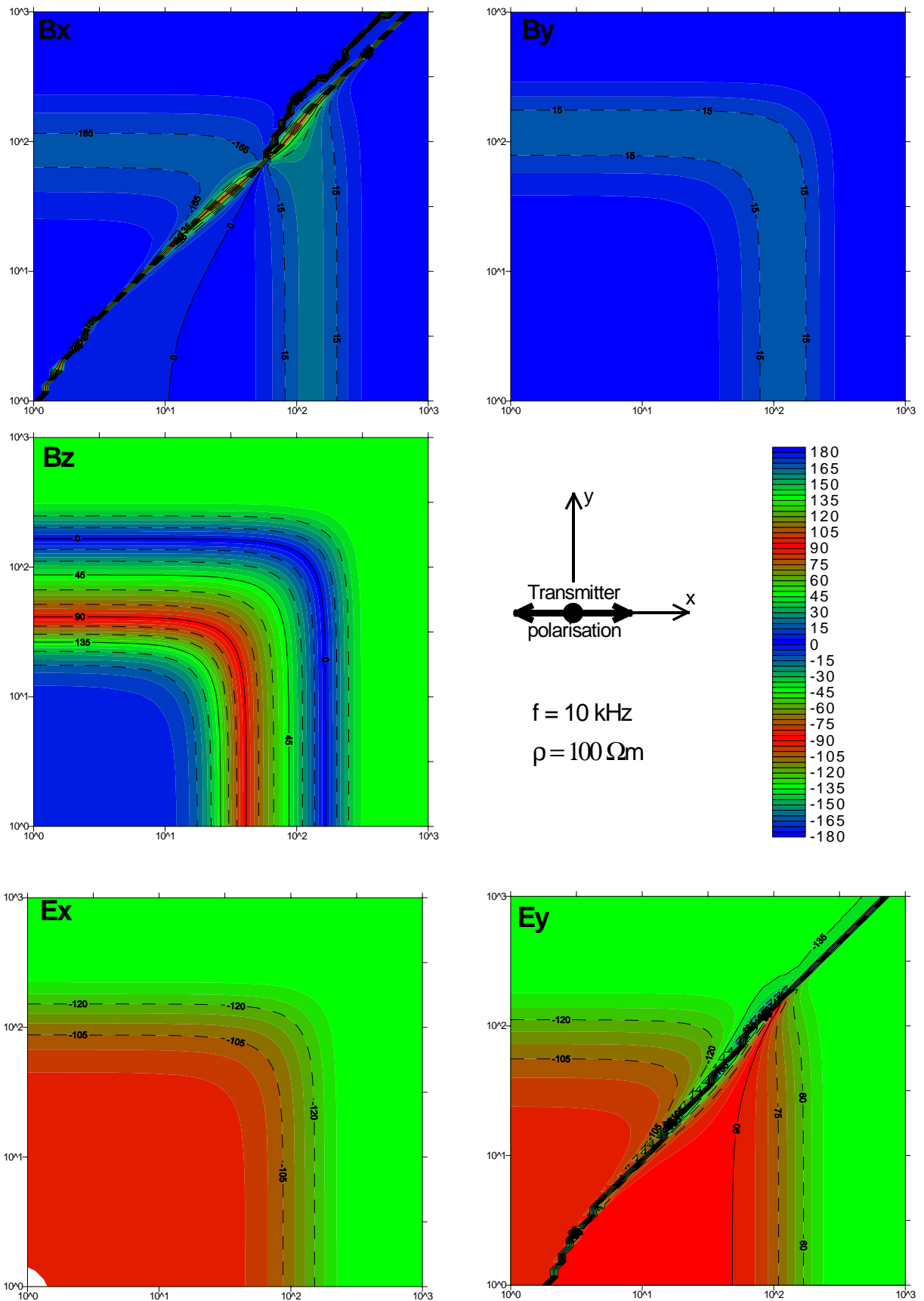
Appendix II-3 Absolute values of the fields over a 100 Ωm halfspace from 1 m to 1 km distance to the source.



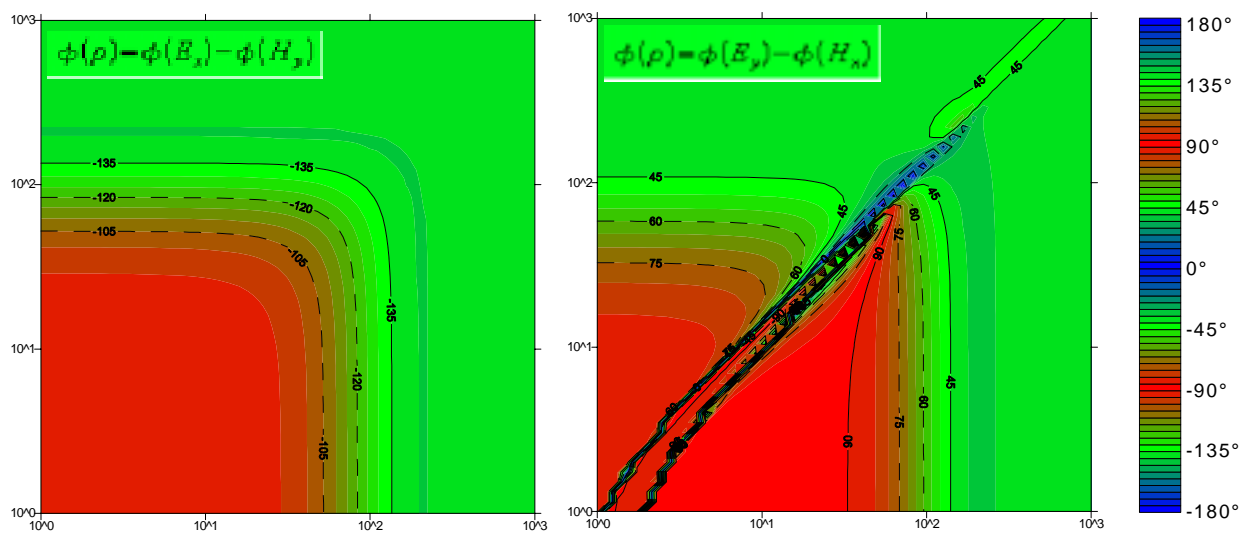
Appendix II÷4 Absolute values of the horizontal electric field over a 100 Ω m halfspace from 1 m to 1 km distance to the source. (Legend like in II÷3)



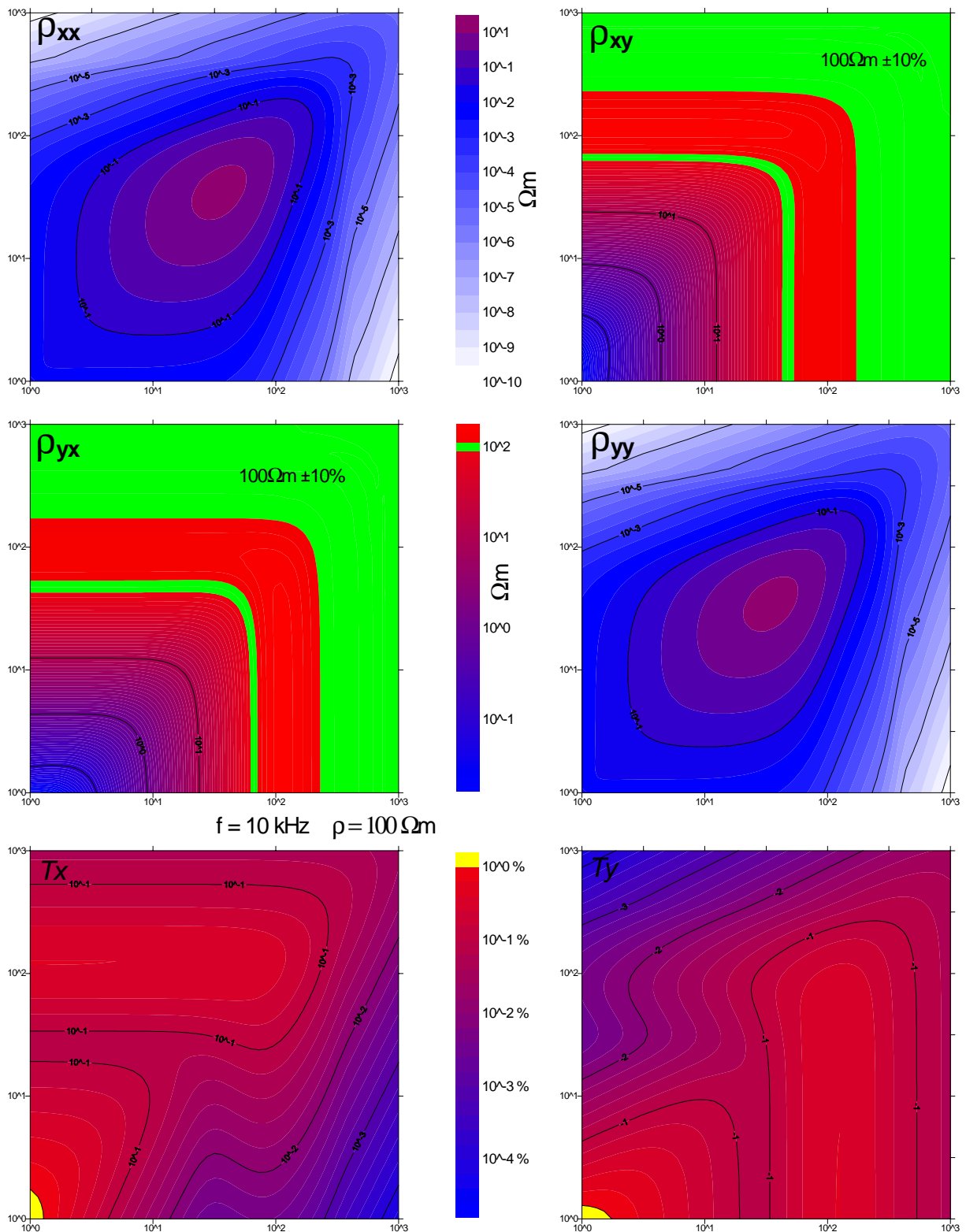
Appendix II÷5 Simulated phases of the fields caused by a HMD over a homogeneous halfspace.



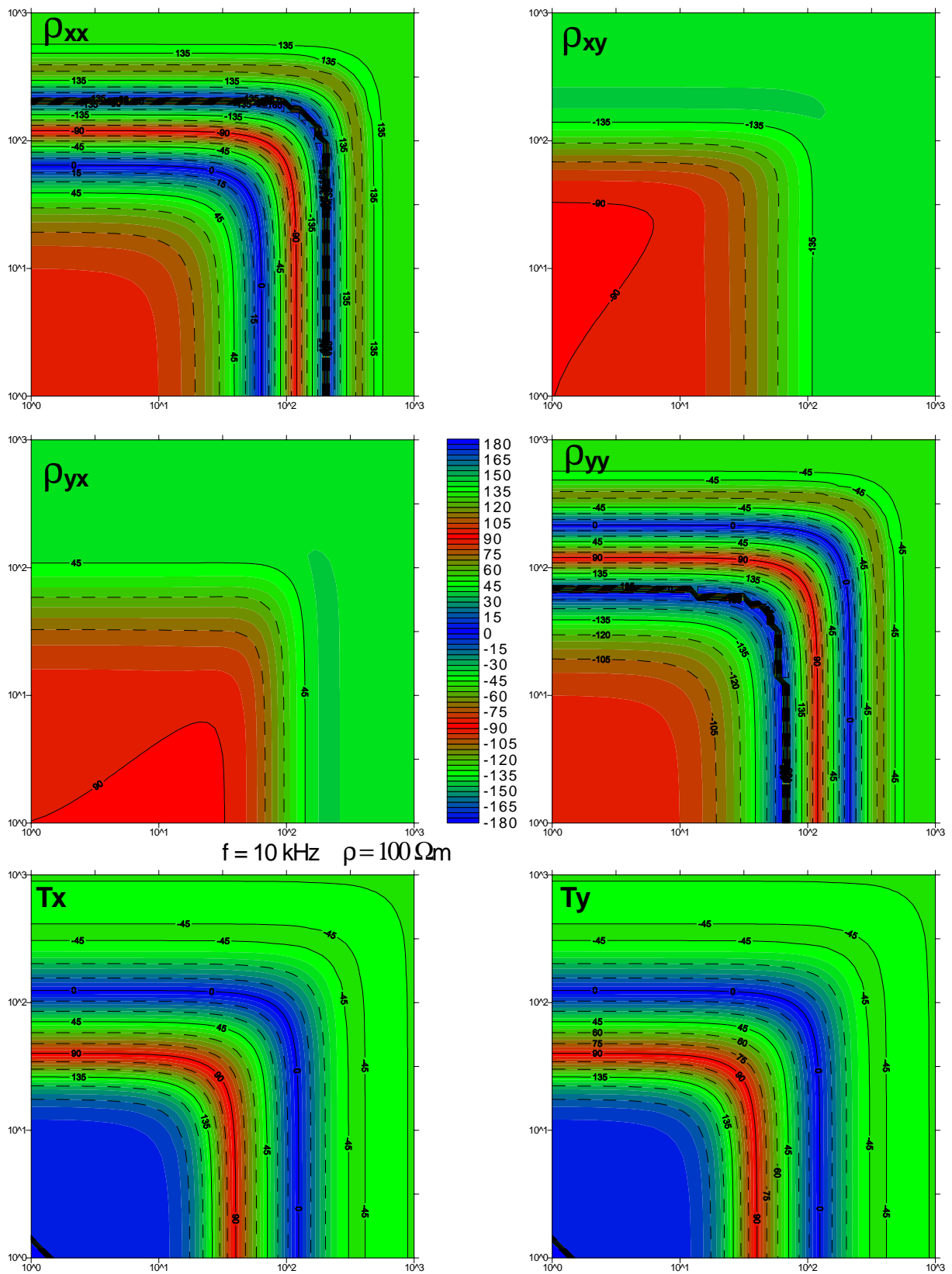
Appendix II-6 Phases of the fields over a $100 \Omega\text{m}$ halfspace from 1 m to 1 km distance to the source.



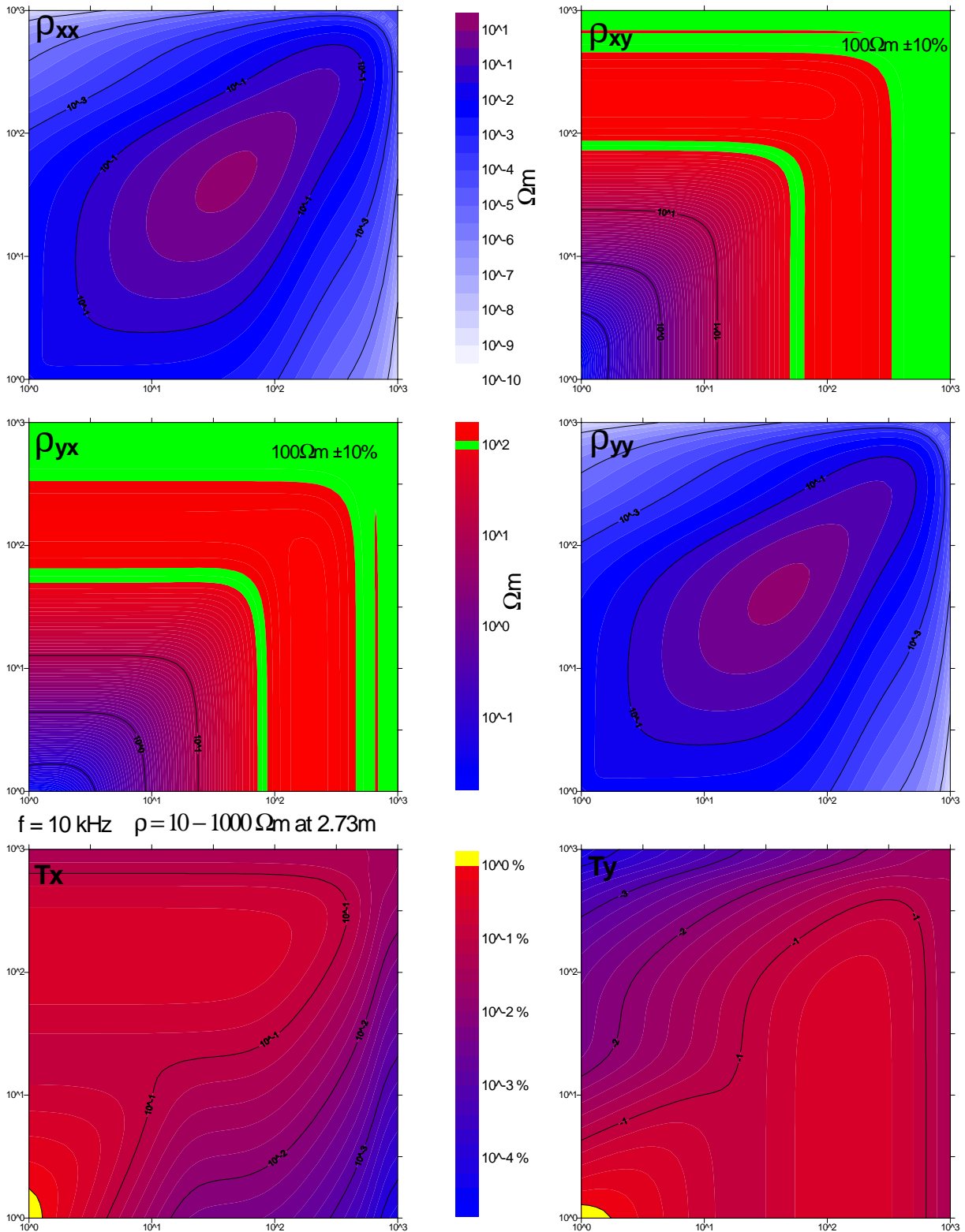
Appendix II÷7 Phases of the scalar resistivities over a homogeneous halfspace.



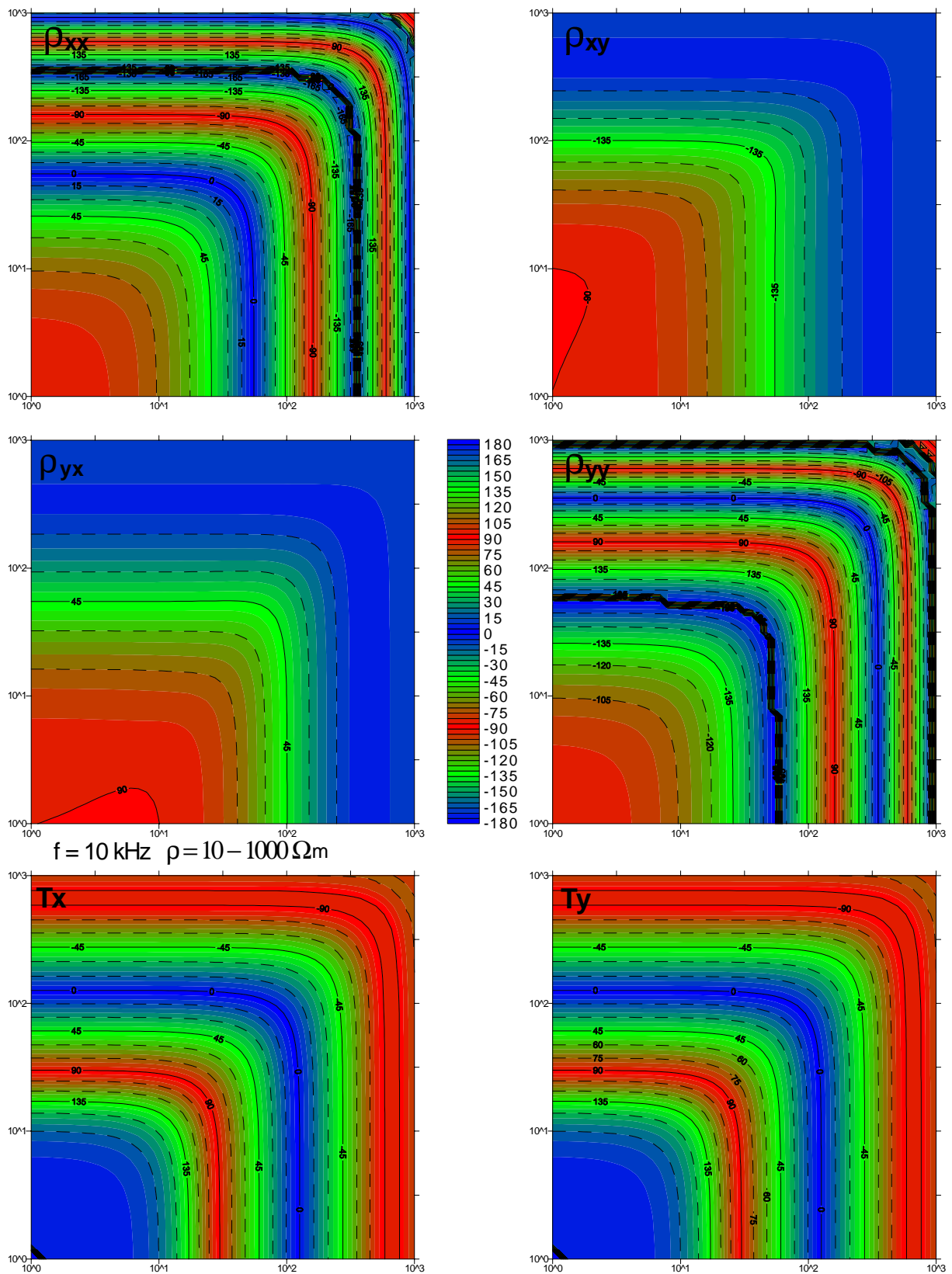
Appendix II-8 Absolute values of the resistivity tensor and tipper vector values over a 100 Ωm halfspace from 1 m to 1 km distance to the source.



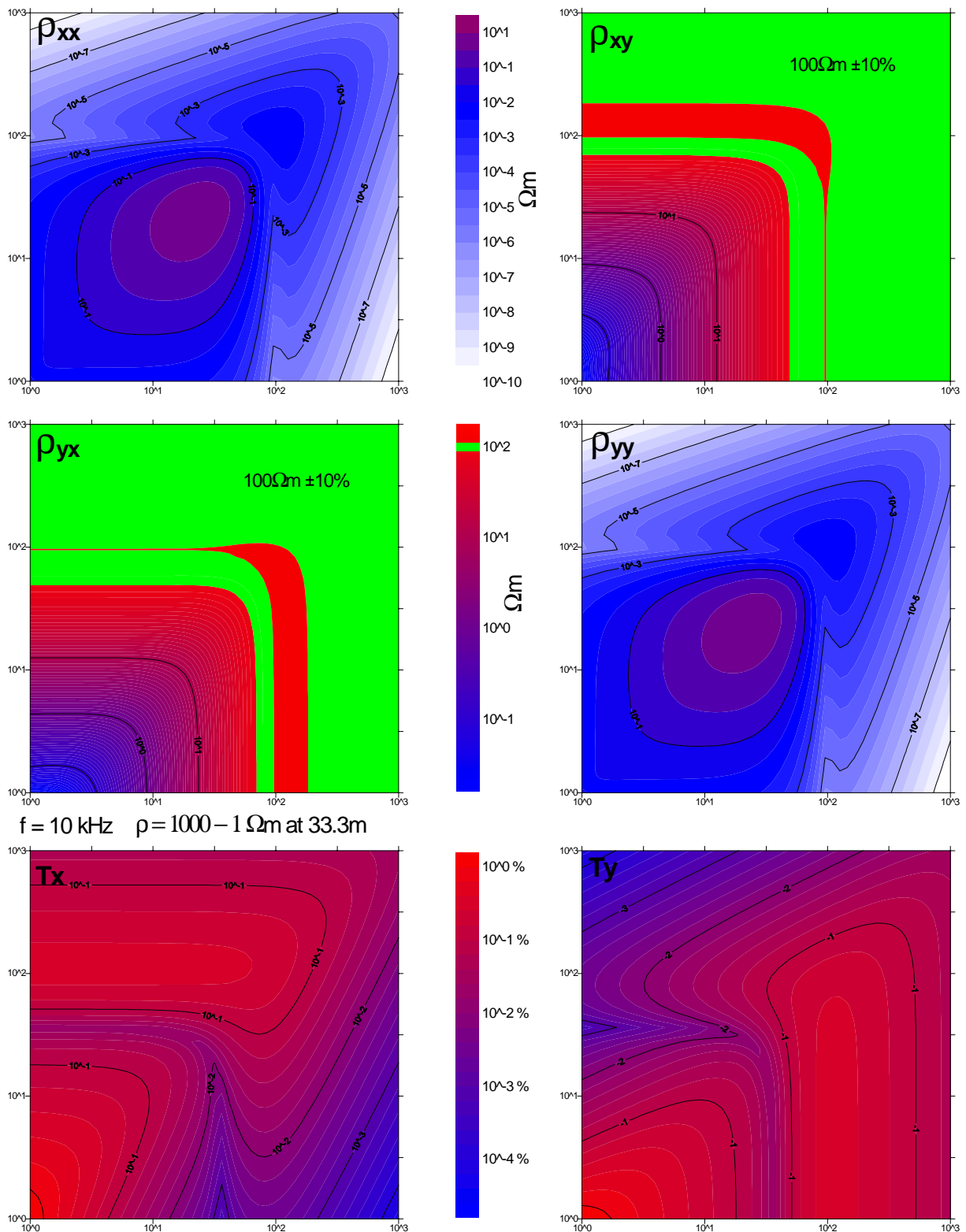
Appendix II-9 Phases of the resistivity tensor and tipper elements over a homogeneous halfspace from 1 m to 1 km distance to the source..



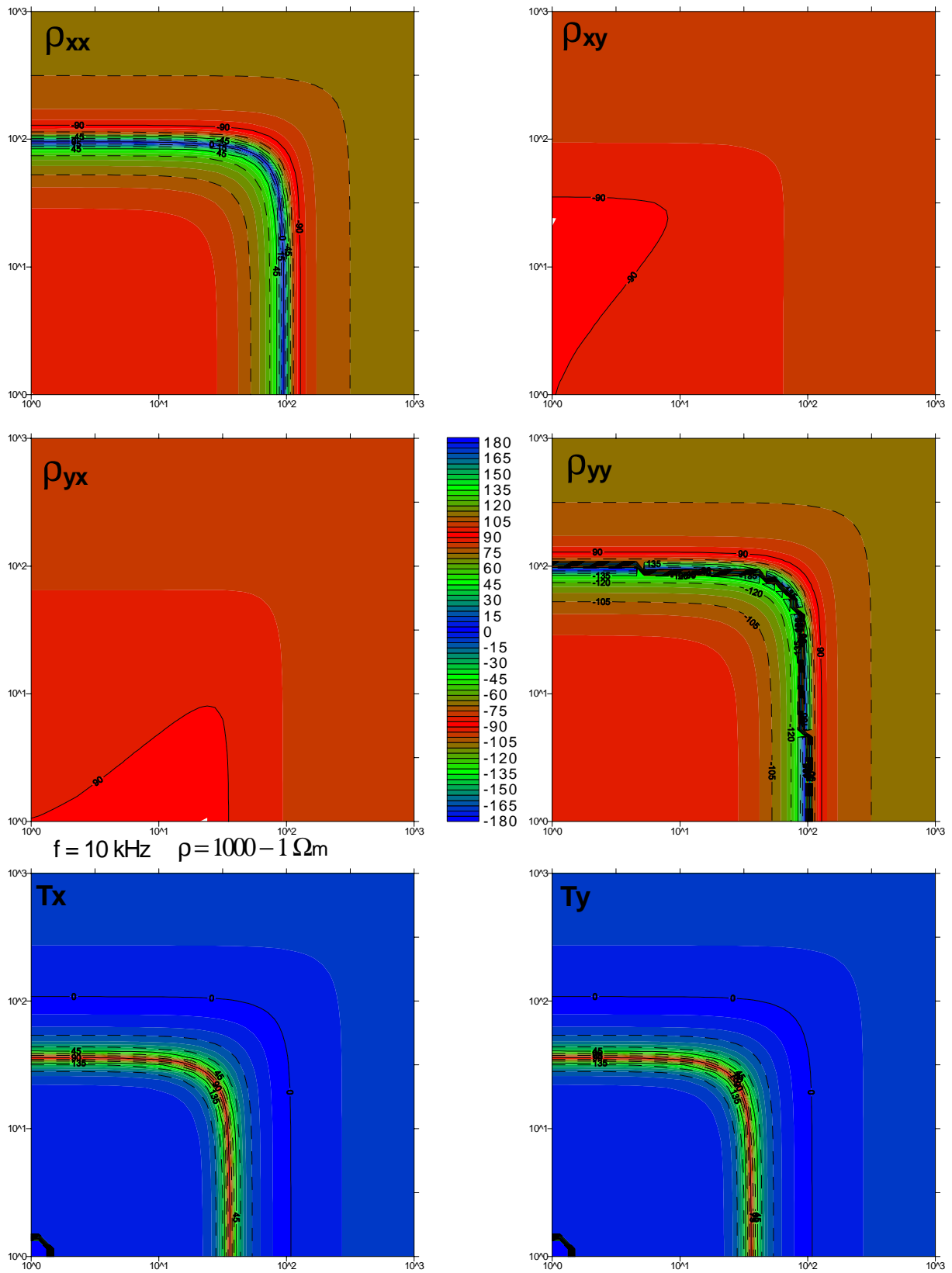
Appendix II-10 Absolute values of the resistivity tensor and tipper vector values over a 2 layered halfspace with conductive overburden.



Appendix II-11 Phases of the resistivity tensor and tipper vector values over a 2 layered halfspace with conductive overburden.



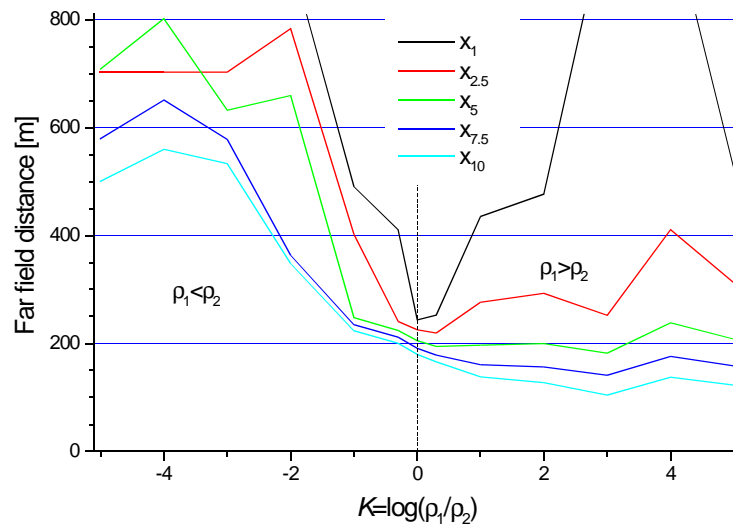
Appendix II-12 Absolute values of the resistivity tensor and tipper vector values over a 2 layered halfspace with resistive overburden.



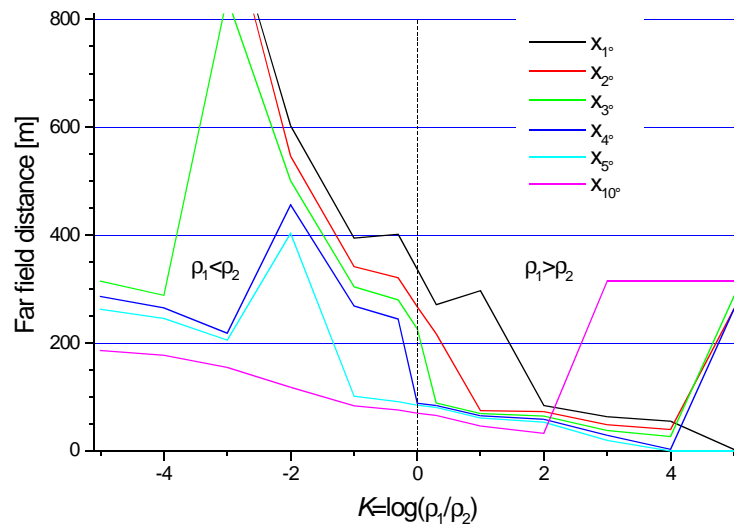
Appendix II-13 Phases of the resistivity tensor and tipper vector values over a 2 layered halfspace with resistive overburden.

ρ_1 [Ωm]	ρ_2 [Ωm]	t [m]	K	Φ [$^\circ$]
1.0E+04	1.0E-01	34,800	5	89
1.0E+04	1.0E+00	33,000	4	86
1.0E+03	1.0E+00	33,180	3	84
1.0E+03	1.0E+01	27,260	2	75
2.0E+02	2.0E+01	27,000	1	65
1.5E+02	7.5E+01	13,300	0.3	50
1.0E+02	1.0E+02		0	45
7.5E+01	1.5E+02	14,040	-0.3	39
2.0E+01	2.0E+02	2,934	-1	31
1.0E+01	1.0E+03	2,154	-2	14
1.0E+01	1.0E+04	3,318	-3	6
1.0E+01	1.0E+05	3,486	-4	3
1.0E+01	1.0E+06	3,538	-5	2

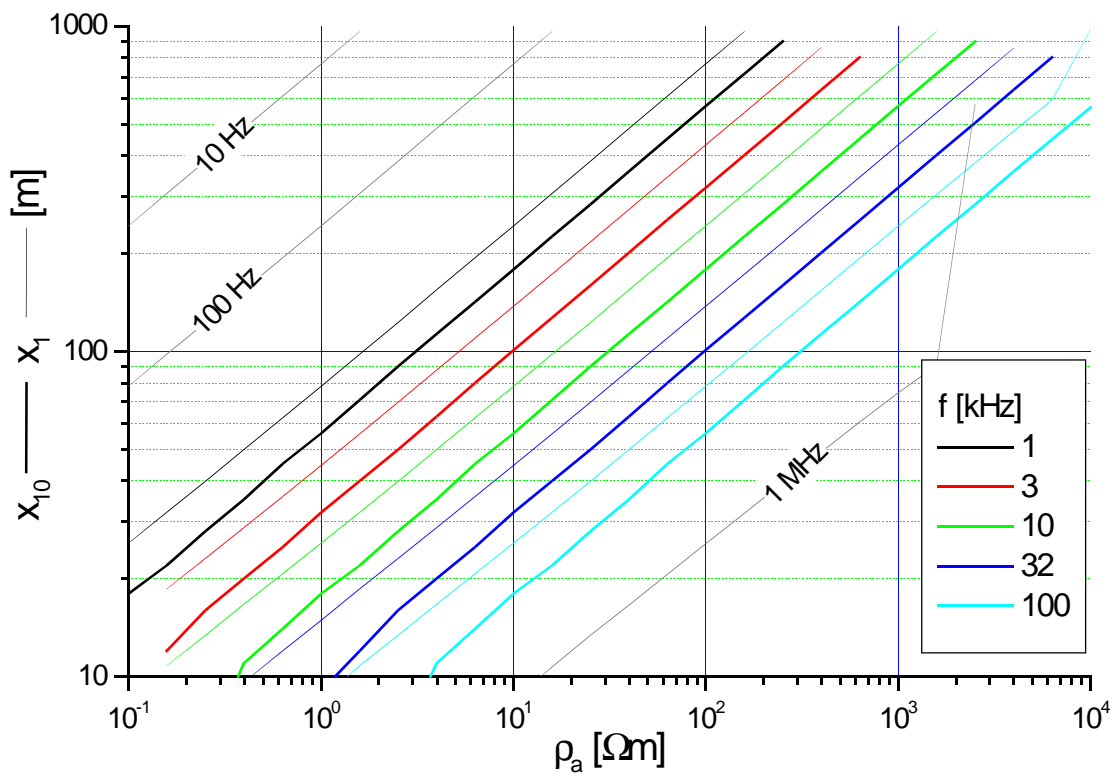
Appendix II-14 Table of the used resistivities and depths for the simulations regarding the resistivity contrast. Phases Φ are given for 10 kHz.



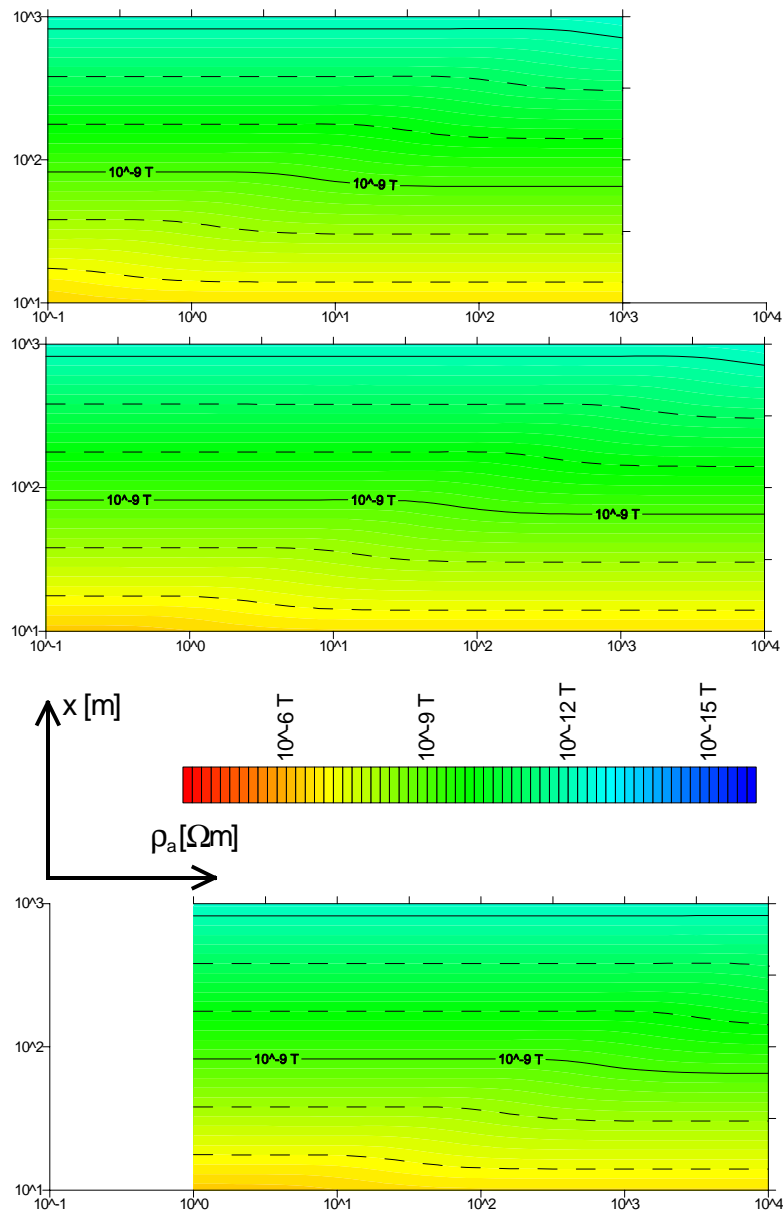
Appendix II-15 FFD for 1 to 10 % deviation.



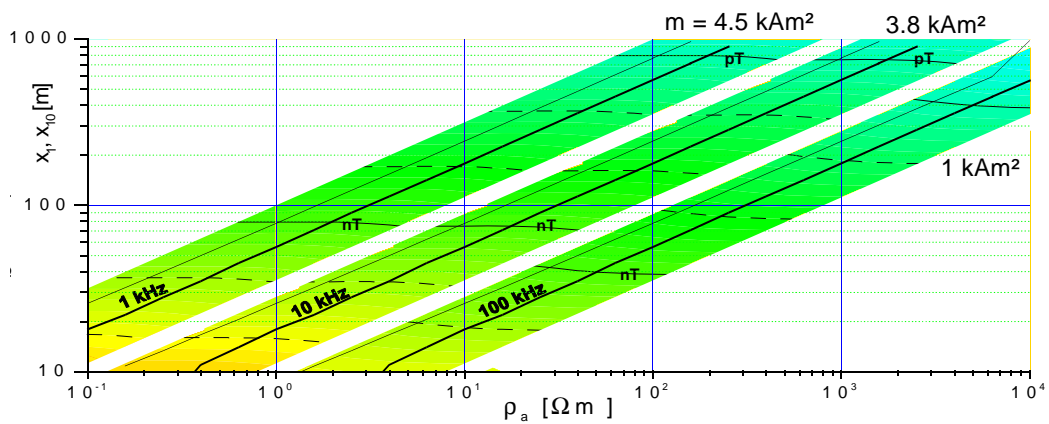
Appendix II÷16 FFD for 1° to 10° deviation.



Appendix II÷17 FFD x_{10} (thick lines) and x_1 (thin lines) for $f = 10$ Hz to 1 MHz.



Appendix II÷18 Bh for 1, 10 and 100 kHz depending of resistivity and distance in x- direction.



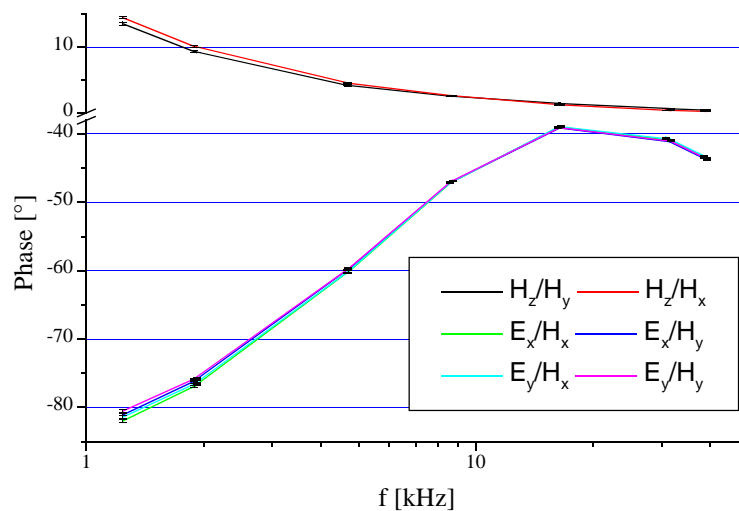
Appendix II÷19 FFD (x_1 thick line) and Bh for 1, 10 and 100 kHz with different m .

III Instrument

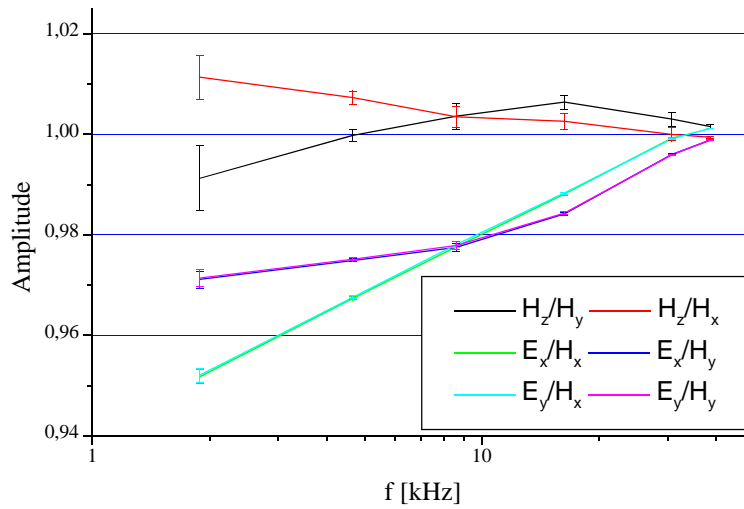
#	Capacity [μF]	f [kHz]							
		1	2	4	8	16	32	64	128
1	1.00E+01	53.26							
2	4.70E+00	25.03	64.32						
3	2.20E+00	11.72	30.11						
4	1.00E+00	5.33		54.63					
5	4.70E-01	2.5		25.68					
6	2.20E-01	1.17	3.01	12.02	54				
7	1.00E-01	0.53	1.37	5.46	24.55	87.97			
8	4.70E-02	0.25	0.64		11.54				
9	2.20E-02	0.12	0.3	1.2	5.4		78.1		
10	1.00E-02	0.05	0.14	0.55	2.45	8.8			
11	4.70E-03	0.03	0.06	0.26	1.15		16.68	68.12	
12	2.20E-03	0.01	0.03	0.12	0.54	1.94		31.88	
13	1.00E-03	0.01	0.01	0.05	0.25	0.88	3.55		68.03
14	4.70E-04	0	0.01	0.03	0.12	0.41	1.67		31.97

Appendix III÷1 List of the implemented capacitors and the relative current in % for the specific frequencies.

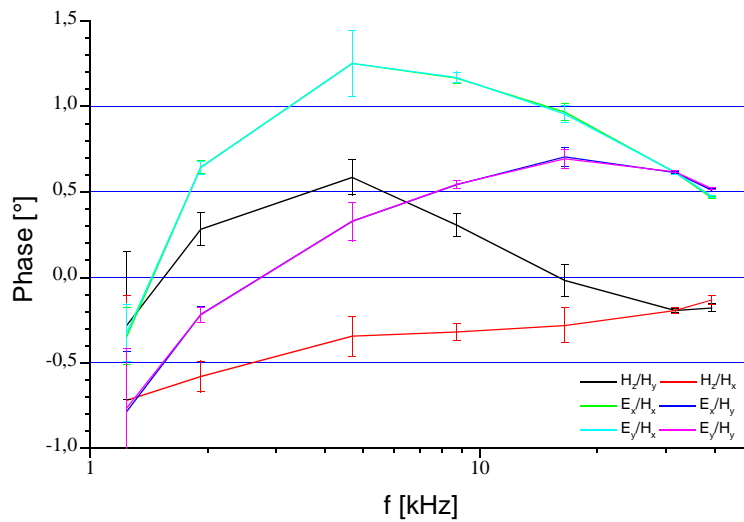
IV Measurements



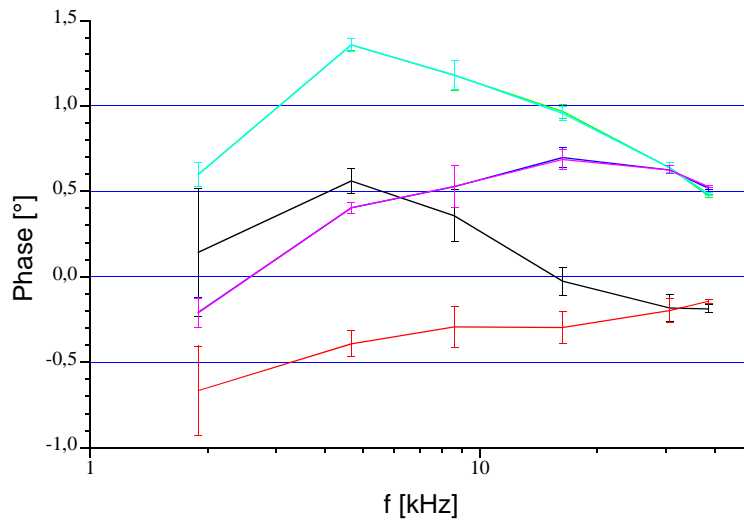
Appendix IV÷1 Uncorrected phases of the ratio of the fields acquired at a simulated CSRMT measurement.



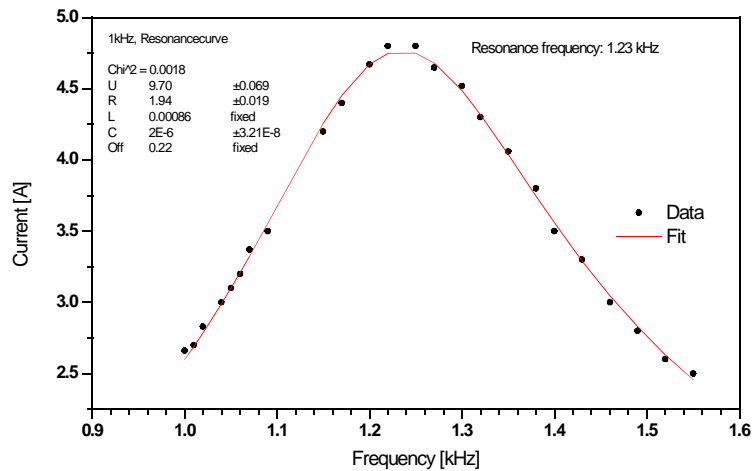
Appendix IV÷2 Corrected (calibrated) amplitudes of the ratio of the fields acquired at a simulated CSRMT measurement at the frequencies of the WE loop.



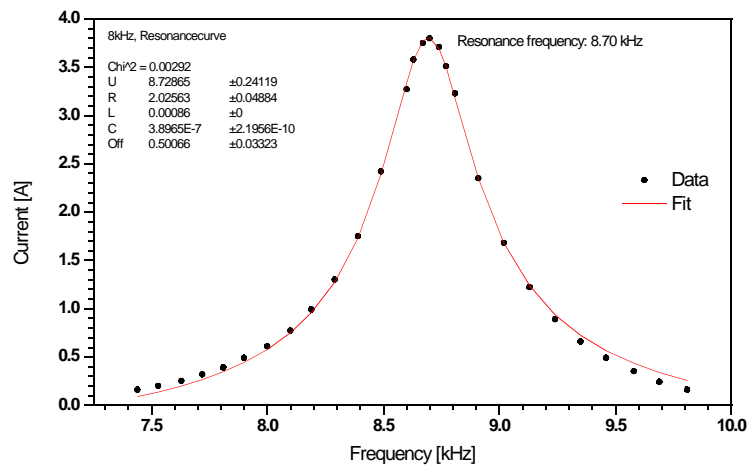
Appendix IV÷3 Corrected (calibrated) phases of the ratio of the fields acquired at a simulated CSRMT measurement at the frequencies of the NS loop.



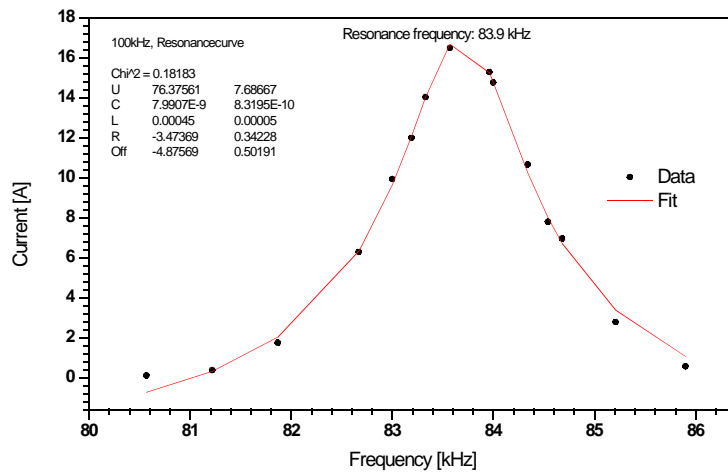
Appendix IV÷4 Corrected (calibrated) phases of the ratio of the fields acquired at a simulated CSRMT measurement at the frequencies of the WE loop.



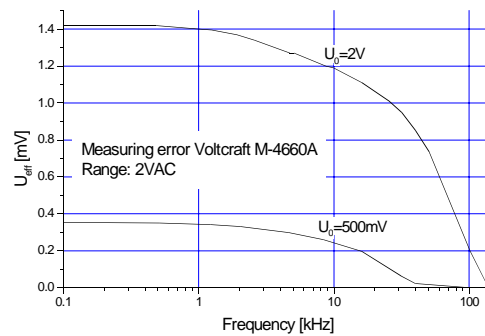
Appendix IV÷5 Current in the transmitter loop depending on the stimulating frequency with capacitors activated for 1 kHz.



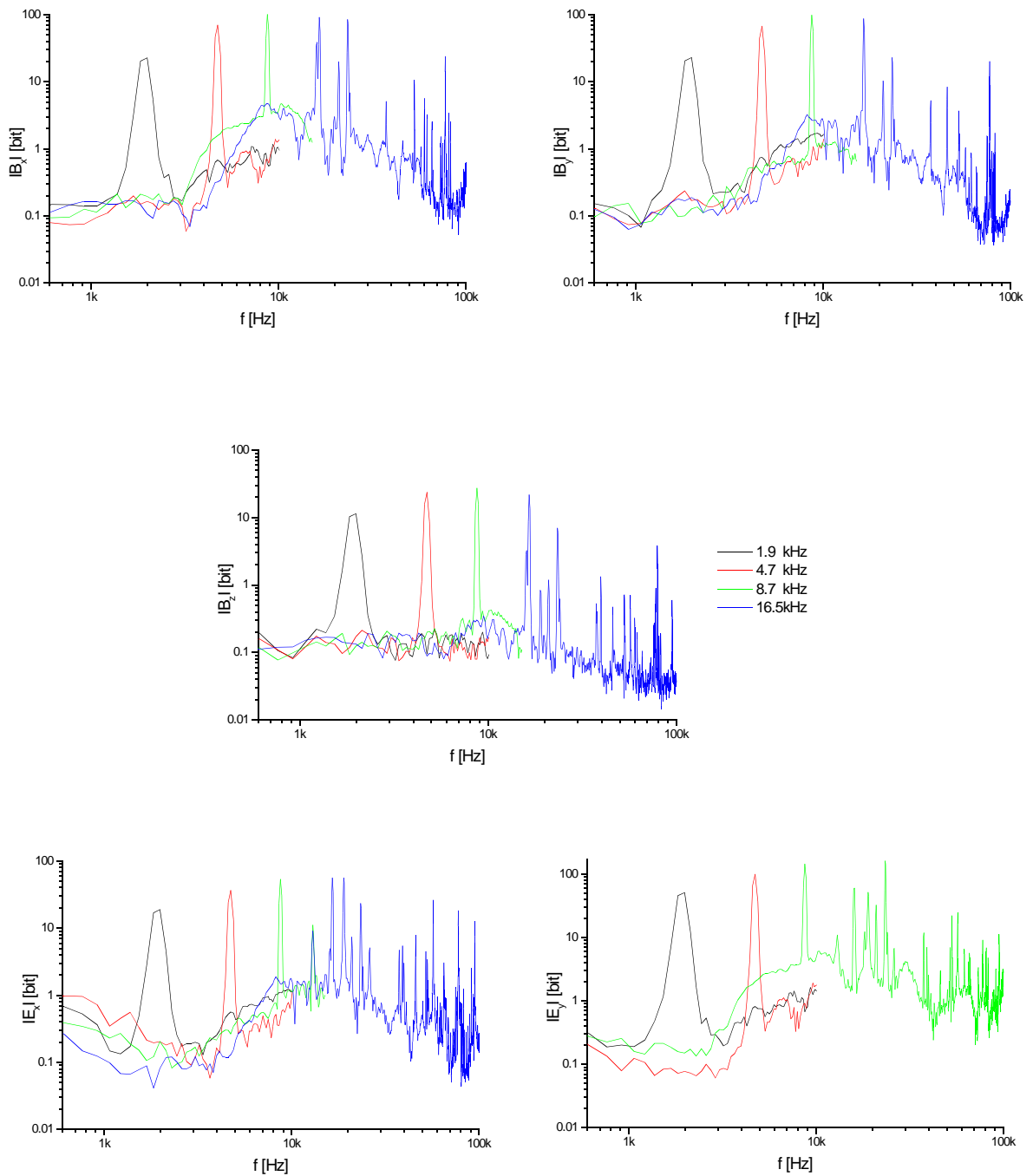
Appendix IV÷6 Current in the transmitter loop depending on the stimulating frequency with capacitors activated for 8 kHz.



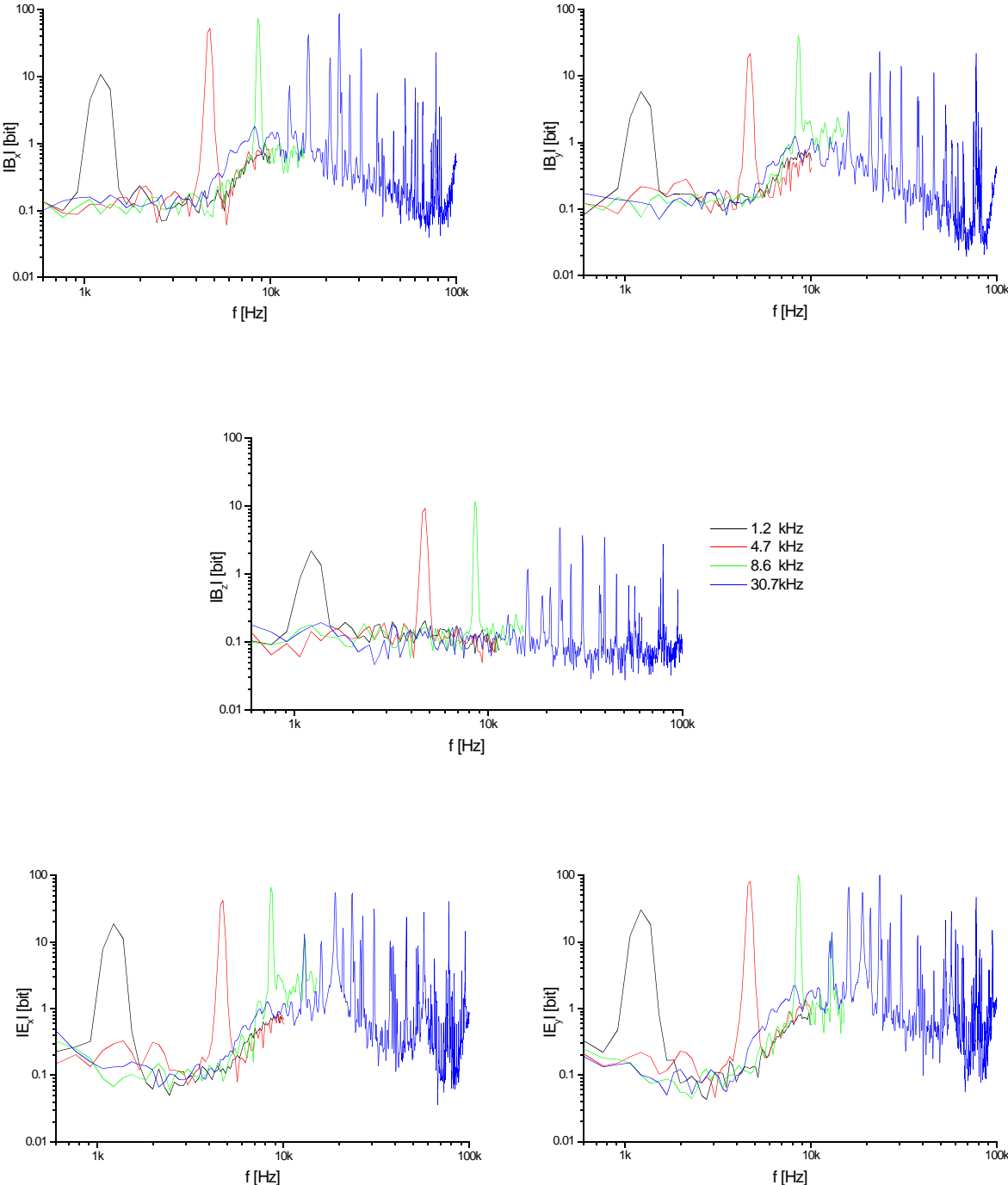
Appendix IV÷7 Current in the transmitter loop depending on the stimulating frequency with capacitors activated for 100 kHz.



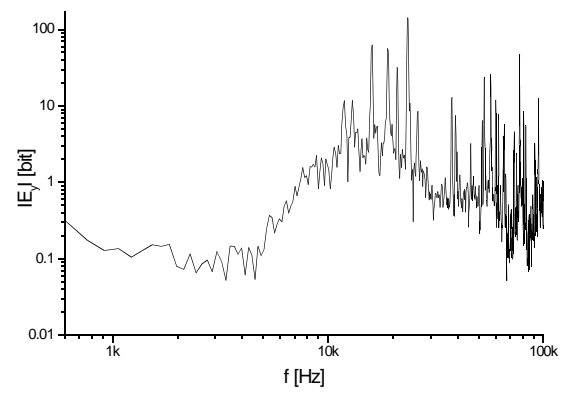
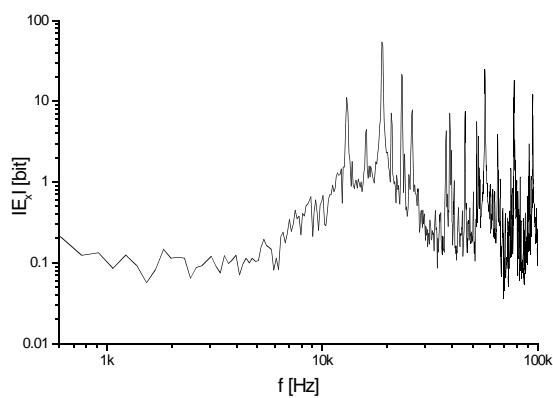
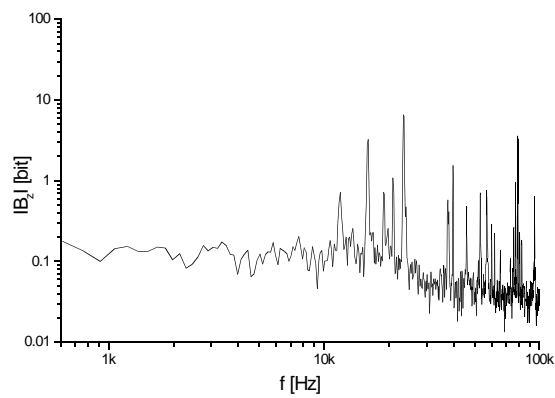
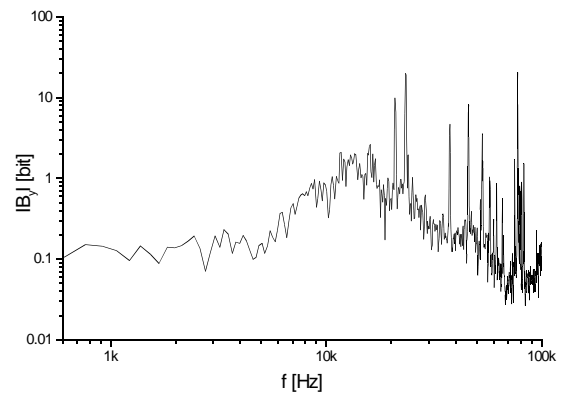
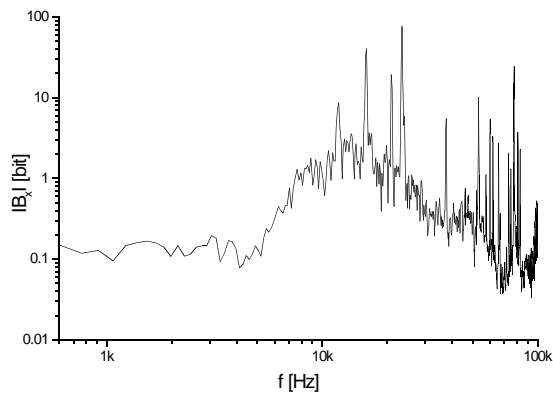
Appendix IV÷8 Frequency response of the used voltmeter.



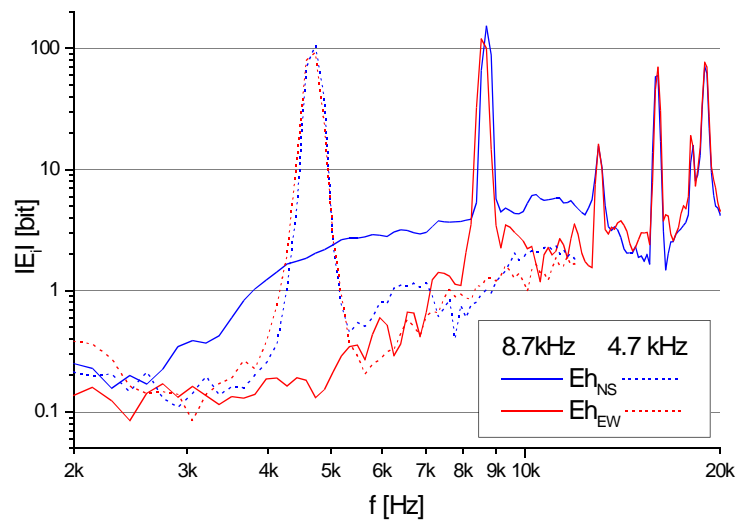
Appendix IV-9 Spectra of the five measured fields while the NS loop was transmitting at four frequencies.



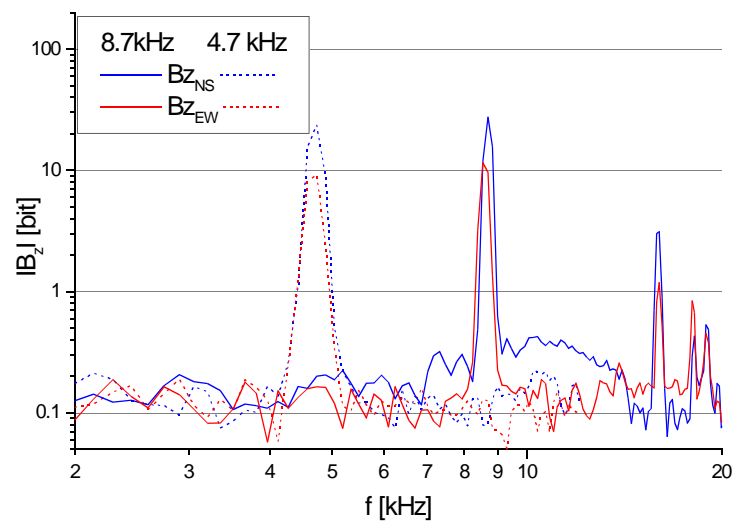
Appendix IV÷10 Spectra of the five measured fields while the WE loop was transmitting at four frequencies.



Appendix IV÷11 Spectra of the fields without active transmitter.



Appendix IV÷12 Spectra of E_h for active frequency 4.7 and 8.7 kHz in both polarizations.



Appendix IV÷13 Spectra of B_z for active frequency 4.7 and 8.7 kHz in both polarizations.

Zusammenfassung (german summary)

Das Ziel dieser Arbeit war die Entwicklung eines "controlled source magnetotelluric" (CSRMT) Systems. Ein Prototyp des Gerätes mußte überarbeitet und Modellrechnungen mußten durchgeführt werden. In Bezug auf die Vorwärtsmodellierungen war das ausschlaggebende Ziel die detaillierte Untersuchung der Fernfeldentfernung (FFD). Die FFD repräsentiert die Entfernung zwischen Sender und Empfänger, bei der eine besondere Voraussetzung erfüllt ist. Die einschränkende Bedingung ist meistens die Abweichung zwischen dem berechneten und dem wahren scheinbaren Widerstand.

Wenn man die Ergebnisse der zahlreichen durchgeführten Simulationen betrachtet, ist es offensichtlich, daß die Fernfeldbedingungen für CSRMT-Messungen bei Entfernungen erreicht werden, die außerhalb der Senderreichweite liegen können. Insbesondere wenn leitfähige Deckschichten berücksichtigt werden, treten Entfernungen zwischen Sender und Empfänger von mindestens 800 Meter auf. Obwohl im Vergleich zu der skalaren, die tensorielle CSRMT-Anordnung die Fernfeldentfernung verringert, ist dieses Problem für Widerstandsmessungen mithilfe der Impedanz nicht gelöst. Im Kontrast zu den Impedanzbestimmungen sind die Nahfeldeffekte Tipperdaten betreffend eliminiert. In der "broadside mode" könnten sogar "skalare Tipper"-Messungen ($T_x = B_z / B_x$) durchgeführt werden, da das vom Sender hervorgerufene vertikale Magnetfeld dort Null ist. Eine handliche Faustformel, die die FFD auf die Skintiefe bezieht wurde entwickelt.

Zusammenfassend laufen die Ergebnisse darauf hinaus, daß die Ebene-Welle-Näherung für CSRMT im allgemeinen nicht gültig ist. Meßpunkte sind entweder außerhalb der Senderreichweite oder innerhalb des Nahfeldes beziehungsweise in der Übergangzone, insbesondere wenn leitfähige Deckschichten auftreten. Daher muß die Verarbeitung von CSRMT-Daten unter Berücksichtigung der Nahfeldeffekte stattfinden.

Einige Änderungen wurden an der Kontroll- und Verarbeitungssoftware für den RMT-Empfänger durchgeführt, um ihn für die CSRMT-Messungen anzupassen. Die Funktion des überarbeiteten Kontrollprogramms wurde durch Labormessungen sichergestellt.

Viel Zeit und Energie wurde investiert, um den Sender-Prototypen geländetauglich zu machen. Leider stellte sich heraus, daß eines der wichtigsten Teile des Systems, nämlich der Verstärker, die Voraussetzungen für diese hohen Ströme und Frequenzen nicht erfüllte.

Deswegen konnten nur wenig präsentierbare Daten aufgezeichnet werden. Trotzdem konnten einige Charakteristika der berechneten Felder auch im Gelände beobachtet werden.

Hiermit versichere ich, die vorliegende Arbeit selbständig und ohne unerlaubte fremde Hilfe sowie nur mit den angegebenen Hilfsmitteln angefertigt zu haben.

Berlin, den 12/01/01 _____